学位論文

Study of muons from ultra-high energy cosmic ray air showers measured with the Telescope Array experiment

(テレスコープアレイ実験による極高エネルギー宇宙線空気シャワー中のミューオンの研究)

平成28年12月博士（理学）申請

東京大学大学院理学系研究科
物理学専攻
武石　隆治

Abstract

The origin of Ultra High Energy Cosmic Ray (UHECR) is a long-standing mystery. The aim of the Telescope Array (TA) experiment is to reveal the mystery by observing the spectrum, the anisotropy and the mass composition of UHECRs with the surface detector (SD) and the fluorescence detector (FD). UHECRs are observed by the signal of air shower particles, and information of primary cosmic rays is estimated from the air shower Monte Carlo (MC) simulation. UHECR air showers are not fully understood, and the observation results of the mass composition have the dependence of hadronic models used in the air shower MC. In addition, the Pierre Auger Observatory measured the number of muons from UHECR air showers with the water Cherenkov type surface detectors sensitive to muons, and reported that the average ratio of the observed number of muons to the MC prediction value is $1.841 \pm 0.029(\text{stat.}) \pm 0.324(\text{syst.})$ using QGSJET II-03 hadronic interaction model for proton. The Auger group claimed the excess of muons in the data.

The number of muons from the UHECRs on the ground depends on the composition of primary cosmic rays. Its MC prediction also depends on hadronic interaction models since it is related to the shower propagation at the early stage. One may test the hadronic interaction models by comparing the measured number of muons with the MC prediction. The TA experiment uses the SD made of plastic scintillator. It is sensitive to the electromagnetic component that is the major part of secondary cosmic rays from UHECR air showers. An analysis approach to increasing muon purity is necessary to calculate the number of muons in the TA SD data.

We selected the air shower events and the SDs used in the analysis by the zenith angle of the event θ, the azimuth angle ϕ of the SD relative to the shower axis and the distance R from the shower axis to the SD to search for muon-enriched condition. Then the signal size, which is the energy deposit of air shower signals in the SD, is compared between the observed air shower event data and the MC on that condition. We used the lateral distribution of the signal size for the comparison to study the air shower structure. The typical ratios of the signal size of the data to that of the MC with QGSJET II-03 model observed on the condition of muon purity 60 - 70% were $1.72 \pm 0.10(\text{stat.}) \pm 0.40(\text{syst.})$ at 1910 m $< R <$ 2160 m and $3.14 \pm 0.36(\text{stat.}) \pm 0.72(\text{syst.})$ at 2760 m $< R <$ 3120m. The average signal size is found to decrease slower in the data than in the MC when R is larger, namely larger discrepancy at larger R. The similar properties existed in different hadronic models (QGSJET II-04, Epos 1.99 and Sibyll 2.1). The signal size of the MC for iron was closer to that of the data than the MC for proton, but the data is larger than the MC for iron with the significance greater than 1σ in $R > 3000$ m. The feature obtained in this work that the signal size of the data is larger than that of the MC was qualitatively consistent with the muon excess detected in researches of Pierre Auger Observatory. In addition to the Auger analysis, where the R dependence of muons was not studied, we confirmed the lateral distribution of the MC does not reproduce the data on the analysis condition ($30^\circ < \theta < 45^\circ, 150^\circ < |\phi| < 180^\circ$,2000 m

$< R <$ 4000 m) with the significance of 1.6 - 2.7σ.

Contents

1 Introduction

1.1 Ultra-high energy cosmic ray

The cosmic ray history began in 1912 when Hess measured the ionization rate of the atmosphere about kilometers above the sea level by balloon flight [1]. He found the average ionization increased with increasing altitude. This was a clear evidence that the source of the ionizing radiation must be located above the Earth's atmosphere. Later study revealed the radiation source is particles from outside of the Earth, which was named "cosmic ray".

Figure 1.1 provides the energy spectrum of observed cosmic rays from various experiments [2]. The range of the energy is from 10^8 eV to 10^{20} eV and the spectrum can be described by power-law distributions.

In the energy range 10^8 eV - 10^{10} eV, the flux is decreased from power-law distribution. This is due to the cosmic rays from sources inside the Galaxy is diffused by the solar magnetic field. On this energy range, the fluxes of particles varies depending on solar activity. At less than 10^8 eV, there are low energy cosmic rays derived from the Sun, such as the Solar Wind or the Solar Flare.

On high energy side of the spectrum, the energy spectra of the cosmic ray can be described by

$$N(E)dE = KE^{-x}dE \tag{1.1}$$

with $x \approx 2.7$. This relation is applicable with energies in the range 10^9 eV - 10^{14} eV. There is a steepening of the spectrum in 10^{15} eV - 10^{16} eV, which is called "knee". Since particles can be accelerated up to this energy range by diffusive shock acceleration in the magnetic field in supernova remnants (see appendix I), this break is thought to be due to decrease of the flux on acceleration limitation energy. The spectrum index x is 3.1 in the energy range between 10^{14} eV and $10^{18.5}$ eV. There is the spectrum flattens at about $10^{18.5}$ eV, referred to as the "ankle". At this energy range, the cosmic ray arrival rate is 1 particle km^{-2} year^{-1}.

The cosmic ray spectrum is observed by various detectors and observation methods. At the energies below about 10^{15} eV, cosmic ray particles are directly measured by balloon experiments and satellites. The energy spectra of different cosmic ray species below 10^{15} eV are shown in Figure 1.2 [3]. At this energy range, proton component is dominant. In the energy range above 10^{15} eV, where the arrival rate is less than 1 particle m^{-2} year^{-1}, the energy spectra are obtained from cosmic ray air showers by detectors on the ground. At higher energies, the composition is identified by the measurement of the

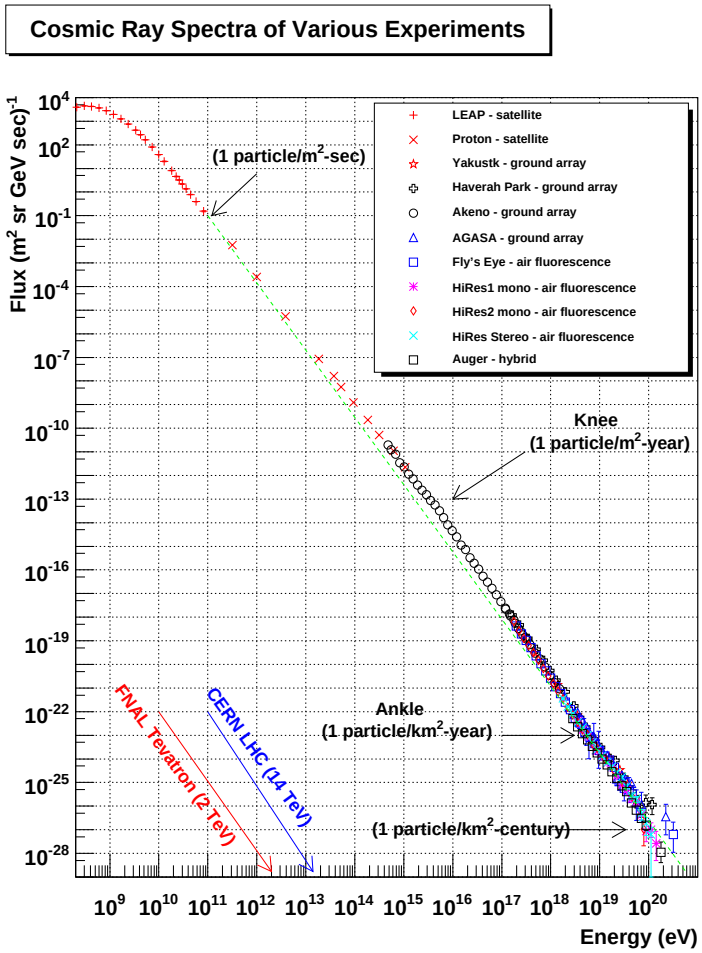

Figure 1.1: The energy spectrum of observed cosmic rays from various experiments [2].

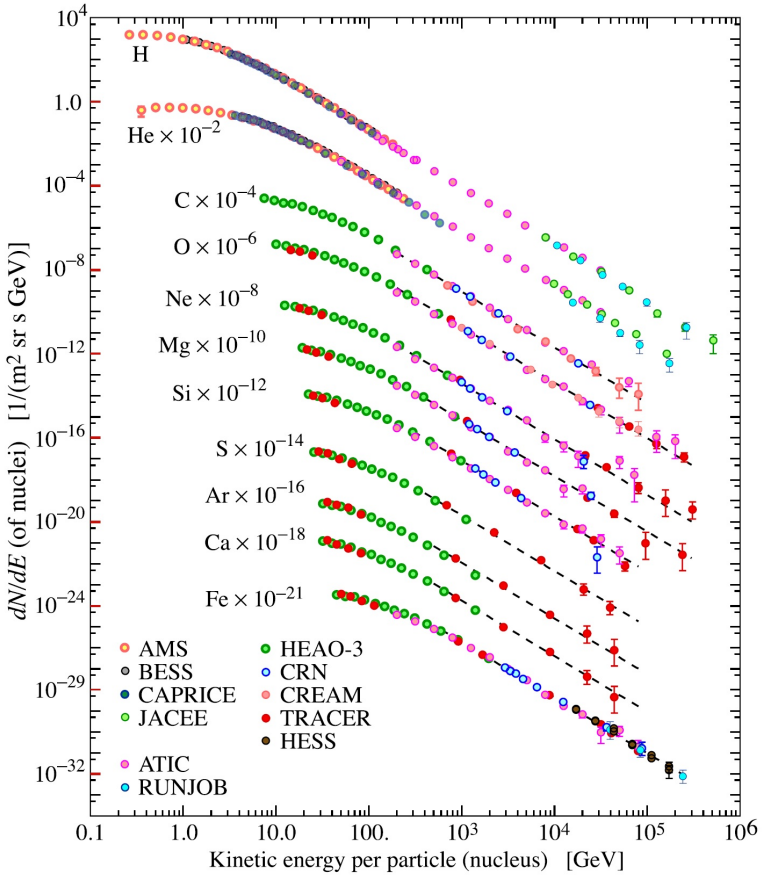

Figure 1.2: The energy spectra of various cosmic ray species [3]. The horizontal axis represents the primary cosmic ray kinetic energy per nucleus. The vertical axis represents fluxes of nuclei of the primary cosmic rays

depth of air-shower maximum as described later sections.

Cosmic rays with energies above about 10^{18} eV are called Ultra-High Energy Cosmic Ray (UHECR). In the 1930s, P. Auger *et al.* observed coincidences of cosmic ray events between particle detectors separated by up to 300 m on the ground [4]. They inferred that the coincidences were caused by nucleonic cascades of cosmic rays at the top of the atmosphere. The showers were the secondary particles of primary cosmic rays, and named "extensive air-showers (EAS)". After that, a number of particle detector arrays were constructed to detect the most energetic cosmic rays.

The larger the energy of the primary particle, the further the EAS penetrates through the atmosphere. Hence the larger detector array can observe the larger energy cosmic rays. The Akeno Giant Air Shower Array (AGASA) in Japan had 111 scintillator detectors and 27 muon detectors regularly spaced over an area roughly 14×8 km^2 [5]. The maximum energy of detected cosmic rays were $\sim 10^{20}$ eV on the experiment.

Charged particles excite nitrogen molecules in the atmosphere and make isotropic

emission of fluorescent radiation. The intensity of fluorescent radiation is proportional to the flux of charged particles. Thus by measuring the flux of fluorescent radiation, the development of the shower through the atmosphere can be determined. Pioneering experiment using this technique was Fly's Eye. The experiment reported the event of the energy 3×10^{20} eV [6] at the maximum. The technique was also used in the High Resolution Fly's Eye (HiRes) air-fluorescence experiment, in which air-fluorescence telescopes were located separated by several kilometers so that the shower geometry of the energy above 10^{19} eV was determined with better accuracy than monocular telescope [7, 8, 9].

Large statistics of cosmic rays are obtained by the surface detector, while precise measurement of the cosmic ray energy is achieved by the fluorescence telescope. The combined technique using the surface detector and the fluorescence telescope is called hybrid observation. In the method coincident measurements of both detectors are performed and the observed cosmic ray energy is cross-checked to make large cosmic ray statistics in high accuracy. The Telescope Array experiment (TA) located in Utah, USA uses this technique and observing UHECRs since 2008. The Pierre Auger Observatory (Auger) in Western Argentina also uses the same technique and taking data from 2004. Currently, these two experiments are taking data to observe UHECRs.

The origin of the UHECR is unrevealed. The observation of the spectrum and anisotropy of the arrival direction are necessary to expect the astrophysical sources of the UHECR. Since cosmic rays are deflected in the galactic and extragalactic magnetic field, the observation of the mass composition is also needed. Those parameters of the UHECR are reconstructed from the signals of the surface detectors and fluorescence telescopes using the Monte-Carlo (MC) simulation of air showers. However, the UHECR air showers are not fully understood, so the observation results of the mass composition have hadronic model dependence used in the air shower MC. One experimental procedure to improve the models is to observe muons in air showers. In the following sections, current understanding of the air showers and previous study of muons in air showers are described.

1.2 Cosmic ray acceleration and source

1.2.1 The acceleration of high energy particles

The existence of cosmic rays indicates that the process of the acceleration of high energy particles and non-thermal radiation occur at astrophysical sources. The energy spectrum form is $dN(E) \propto E^{-x}dE$, where the exponent x typically lies in the range 2 - 3. The Fermi mechanism was first proposed in 1949 as an acceleration mean of high energy particles. This theory naturally explains that the cosmic ray energy spectrum forms a power-law. For more details, see Appendix I.

1.2.2 Cosmic ray source

The cosmic rays with energies up to $E \sim 10^{18}$ eV, supernova remnants in our Galaxy are possible sources. In this energy range, cosmic ray source cannot be identified by direct detection. It is because cosmic rays are deflected by the galactic magnetic field during propagation to the Earth. The sources are estimated by indirect measurements using secondary neutral particles, such as gamma rays generated at the sources by the cosmic ray interaction [13].

On UHECR, Hillas diagram provides the hints for the cosmic ray sources [14]. The maximum cosmic ray energy accelerated in a magnetic field of flux density B and scale L can be calculated by the shock acceleration theory (*cf.* Appendix I);

$$E_{\max} = zeBUL \tag{1.2}$$

where z is particle charge, e is the elementary charge and U is the speed of the shock. If the particle has the energy $E \sim 10^{20}$ eV, this equation becomes

$$\frac{3 \times 10^{11}}{z\beta} = \left(\frac{B}{\mathrm{T}}\right)\left(\frac{L}{\mathrm{m}}\right) \tag{1.3}$$

where $\beta = U/c$. This relation is drawn in figure 1.3 with astrophysical objects of UHECR source candidates. If the plot of the source lies above the blue (red) line in the figure, protons (iron nuclei) can be accelerated up to $E \sim 10^{20}$ eV. Active galactic nuclei (AGNs) [16] and gamma-ray bursts (GRBs) [17] are the possible source candidates of extragalactic UHECR.

There are remarkable features on UHECR spectrum, which is related to the source candidates. In 1966, Greisen [18], Zatsepin and Kuzmin [19] predicted a suppression in the cosmic ray flux at around 5×10^{19} eV due to the interaction of protons with the cosmic microwave background (CMB), which is called the GZK cutoff. The UHE proton has such large Lorentz factor that CMB photon, which is 2.4×10^{-4} eV blackbody radiation, has very high energies in the proton rest frame. This provides photo-pion production, including the reactions of

$$p + \gamma_{\mathrm{CMB}} \to N + \pi \tag{1.4}$$

The threshold energy of the reaction is around 5×10^{19} eV and so the flux is degraded above the energy. The fractional loss of the energy of a cosmic ray proton in one collision is estimated to be $\sim 1/10$. If the highest energy cosmic ray is a proton, it cannot be originated further than around 50 Mpc, hence the source locates within around 50 Mpc from the Earth.

Also the electron-positron photo-pair production process occurs by the interaction of cosmic ray proton and CMB photon. Although the reaction removes only 10^{-3} of the energy of protons, this process is important at the 10^{18} eV - 10^{19} eV, which makes a distortion on the spectrum which is called “dip” structure.

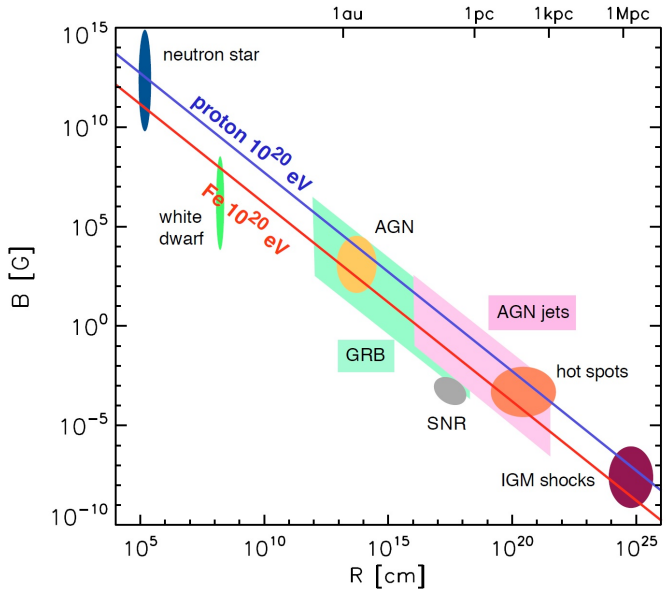

Figure 1.3: Updated Hillas diagram [15]. The vertical and horizontal axes mean a magnetic field of flux density, B, and a scale, R (denoted as L in the text), respectively. Above the blue (red) line in the figure, protons (iron nuclei) can be accelerated up to $E \sim 10^{20}$ eV. The candidate sources are shown with the uncertainties in their parameters.

If the UHECR is a heavy element, there is a cut-off at energies around 5×10^{19} eV because of photonuclear interactions. But the dip structure is not made by the cosmic ray reaction.

Cosmic rays are deflected by the galactic and extragalactic magnetic fields during the propagation from the source to the Earth. The deflection angle is inversely proportional to the cosmic ray energy [20]. At the energies $E > 10^{19}$ eV, the deflection angle is expected to be small enough to appear a sizeable anisotropy [21]. Therefore the UHECR source can be estimated by the measurement of the CR arrival direction.

1.3 Extensive air showers

1.3.1 Cosmic rays in the atmosphere

When cosmic rays enter in the atmosphere, many of the high energy particles cause spallation reactions with atmospheric particles.

$$p + N \to p' + N' + k\pi^+ + k\pi^- + r\pi^0 \tag{1.5}$$

where N is a target atmospheric nucleus, k and r are multiplicity of π particles. The π particles decay during the propagation in the atmosphere.

$$\pi^+ \to \mu^+ + \nu_\mu \tag{1.6}$$

$$\pi^- \to \mu^- + \overline{\nu_\mu} \tag{1.7}$$
$$\pi^0 \to 2\gamma \tag{1.8}$$

The similar reactions also caused by $K^\pm$ instead of $\pi^\pm$, which is generated from primary cosmic ray reactions. Muons from pion (kaon) partially decay and make the following secondary particles.

$$\mu^+ \to e^+ + \nu_e + \overline{\nu_\mu} \tag{1.9}$$
$$\mu^- \to e^- + \overline{\nu_e} + \nu_\mu \tag{1.10}$$

Then the electron and positron cause pair annihilation reaction and generate photons.

$$e^+ + e^- \to \gamma + \gamma \tag{1.11}$$

The photons also cause pair production reaction.

$$\gamma \to e^+ + e^- \tag{1.12}$$

After these cascade reactions, air shower secondary particles reach the ground. They consist of muon, electromagnetic (EM) components (electron, positron and photon), hadronic components such as proton.

Muons are the most numerous charged particles at sea level in the energy range $E > 1$ GeV. Most muons are produced in the height typically 15 km in the atmosphere and lose about 2 GeV by ionization loss before reaching the ground [3]. This type of muons is called atmospheric muons. Their energy and angular distribution reflect a convolution of the production spectrum, energy loss in the atmosphere and decay in 10 GeV - 100 GeV energy range. The mean energy of the muons at the ground is $\sim$ 4 GeV and the angular distribution is proportional to $\cos(2\theta)$ [3]. Figure 1.4 shows the spectrum of atmospheric muons at sea level.

The EM component is generated originally from the decay of mesons as described in (1.6) - (1.10). The ratio of the number of muons to that of EM components depends on the energy threshold and the observation altitude, because the EM components are more reduced than the muons as the atmospheric depth increases.

1.3.2 Extensive air showers

An extensive air shower (EAS) is a cascade of particles caused by a single cosmic ray with energy high enough so that many secondary particles are detectable at the ground. Figure 1.5 is the schematic view of an extensive air shower. The primary cosmic ray makes hadronic interaction in the atmosphere, generating π and K mesons. Then the air shower is generated by the cascade reactions described in the previous section, which consists of hadronic and EM showers. Figure 1.6 shows air shower particle description from MC simulation. The cosmic ray reacts at about 20 km in height and the shower

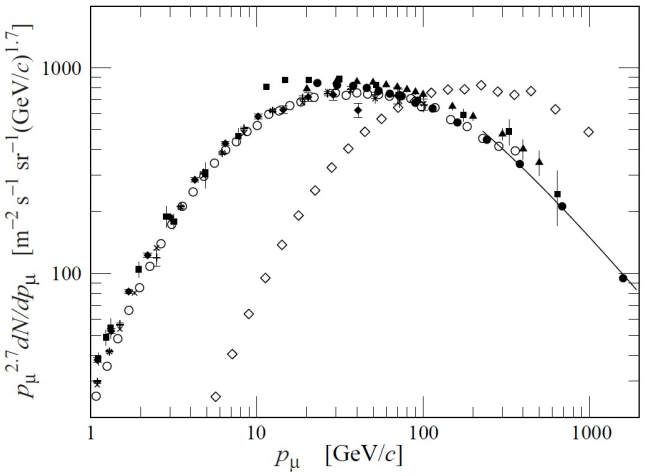

Figure 1.4: The spectra of atmospheric muons at sea level [3]. The diamond represents $\theta = 75°$, while others represent $\theta = 0°$ in various experiments. The line is drawn using an approximate extrapolation formula.

particles extends several kilometers on the ground. Almost particles generated by air showers are EM components ($e^{\pm}$ and γ). The air shower particles at larger distances from the core on the ground are originated from the particles generated at the earlier stage of the showers.

The evolution of the EM shower is as follows. π^0 generated by the cosmic ray interaction decays into two photons as equation (1.8). The photons and $e^{\pm}$ are generated by pair annihilation and production, as equations (1.11) and (1.12). Also $e^{\pm}$ are generated by $\pi^{\pm}$ decay, and photons are generated by bremsstrahlung of $e^{\pm}$. These EM cascade reactions occur repeatedly and a number of particles increase during the propagation in the atmosphere, losing the energy of each particle. After particle energy reaches the critical energy, ionization process dominates over pair production and bremsstrahlung, hence the number of particles turns to decrease. The number of particles becomes maximum at the stage, which is called the air shower maximum. The particles which survive after the propagation in the atmosphere reach the ground.

Most EM particles reaching the ground derives from π^0 decay and most muons are from $\pi^{\pm}$ or K decay. Part of the EM particles on the ground are produced by muons through decay or radiative processes [87]. Also, part of muons on the ground are made by photoproduction reactions [87].

The air shower EM components reach the ground after multiple scatterings and interactions. The air shower muons are less scattered in the atmosphere, hence the muons on the ground have the information about the early stage of the shower propagation. The critical energy of electrons is about 81 MeV [3] and the energy deposit of the minimum ionization particle is 2 MeV/(g/cm^2), hence the radiation length of the electrons is typically 40 g/cm^2. The decrease of air shower muons is mainly caused by muon decay. The

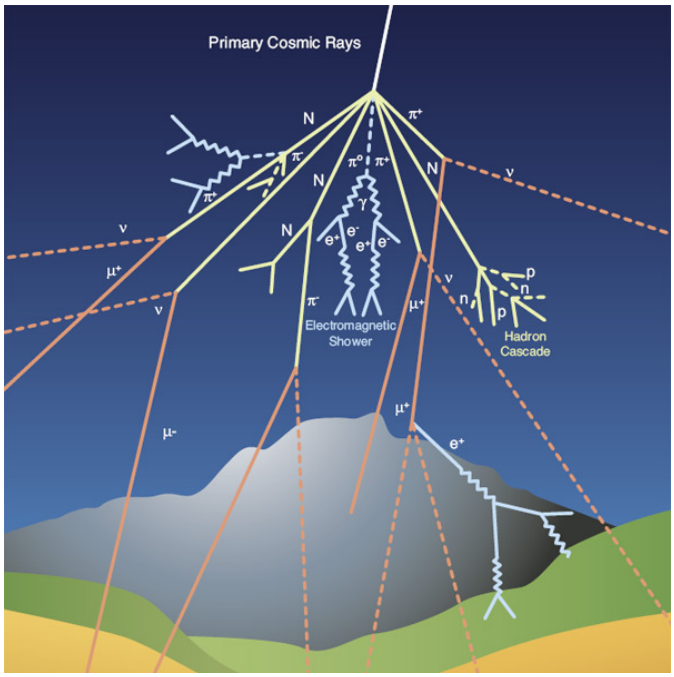

Figure 1.5: The schematic view of an extensive air shower [22].

length which muon passes until decaying is described by $\Gamma c\tau$, where Γ is the Lorents factor and τ is the mean lifetime of a muon in the rest frame, which is 2.2×10^{-6} s. The decay length is about 3 km for 1 GeV muons, while 30 km for 10 GeV muons.

1.3.3 Lateral distribution

Air shower particles from the UHECR extend over a large area (larger about 1 km in the distance from the shower axis) on the ground, due to multiple Coulomb scattering and the transverse momenta of the particle production. The lateral distribution of pure EM cascade particles is expressed by the NKG function.

$$\rho(R) = C \frac{N_{\mathrm{e}}}{{R_{\mathrm{M}}}^2} \left(\frac{R}{R_{\mathrm{M}}} \right)^{s-2} \left(1 + \frac{R}{R_{\mathrm{M}}} \right)^{s-4.5} \tag{1.13}$$

where ρ is the particle density and R is the distance from shower axis. N_{e} is the shower size, which is the total number of EM particles. R_{M} is the Moliére unit, which is the average lateral distribution of electrons with critical energy passing through one radiation length of the matter. $R_{\mathrm{M}} \approx 78$m at sea level [3] and increases as the air density decreases at the higher altitude. The parameter s is the age parameter, which increases as the shower progresses and becomes $s = 1$ at the shower maximum [23]. If s becomes larger, the lateral distribution becomes broader.

The lateral distribution of EM particles from hadronic cascade reactions is described

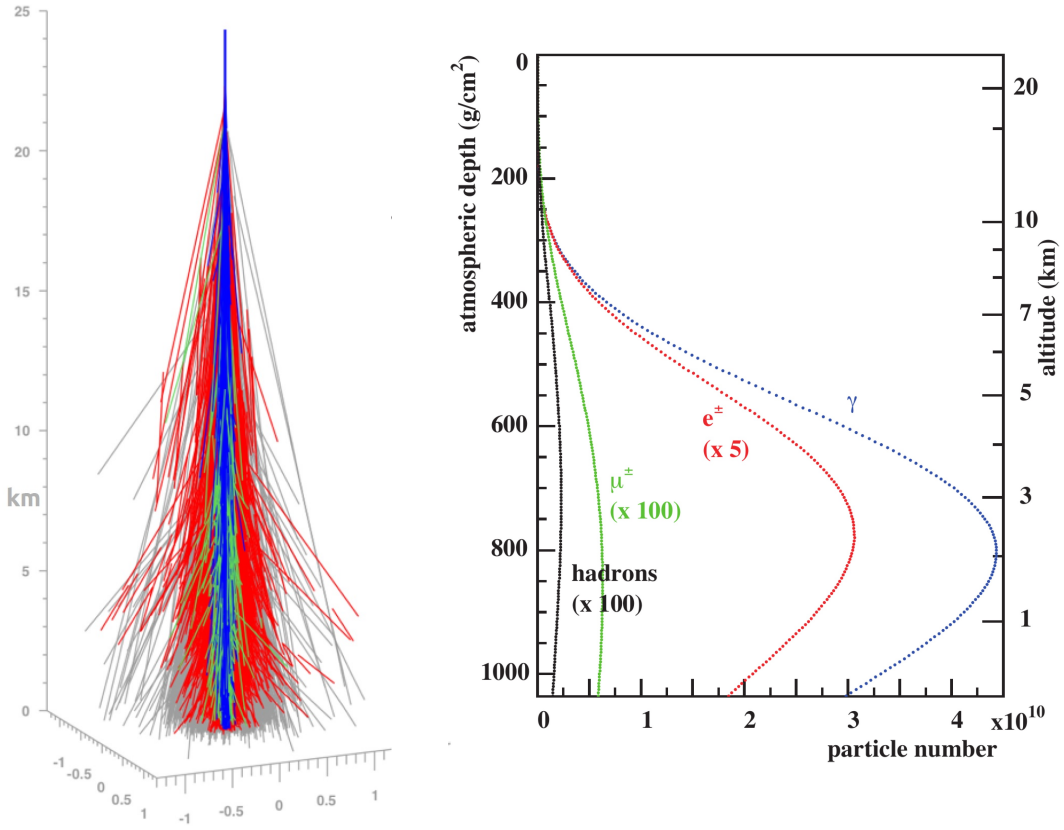

Figure 1.6: The description of air shower particles from MC simulation [47]. (left) The air shower propagation in each particle. The blue, red and green shows gamma, $e^{\pm}$ and muons, respectively. The longitudinal axis represents the altitude and the two horizontal axes mean the lateral distances from the injection track. (right) The evolution of the number of particles. The horizontal axis represents the number of particles and the longitudinal axis means the altitude and corresponding atmospheric depth. At the depth of the Telescope Array experiment (about 870 g/cm^2), the EM components are dominated.

by Linsley [24];

$$\rho_{\rm e}(R) = N_{\rm e}C_{\rm e}\left(\frac{R}{R_{\rm M}}\right)^{-\alpha}\left(1+\frac{R}{R_{\rm M}}\right)^{-(\eta-\alpha)} \tag{1.14}$$

where $C_{\rm e}$ is a normalization factor. α and η are characteristic of the structure of the function, determined by the observed lateral distribution. For example, $R_{\rm M} = 91.6$ m and α is estimated as 1.2 for AGASA experiment [25]. Also an additional term was introduced in the function and described the lateral distribution for AGASA experiment [26];

$$\rho(R) = C\left(\frac{R}{R_{\rm M}}\right)^{-1.2}\left(1+\frac{R}{R_{\rm M}}\right)^{-(\eta-1.2)}\left(1+\left(\frac{R}{1000}\right)^{2}\right)^{-\delta} \tag{1.15}$$

$$\eta = (3.97\pm0.13) - (1.79\pm0.62)(\sec\theta - 1) \tag{1.16}$$

where $C = N_{\rm e}C_{\rm e}$.

The lateral distribution of muons from UHECR air showers are introduced in Appendix Ⅱ.

1.3.4 Longitudinal development

The number of charged particles N at the given atmospheric depth X is expressed by Gaisser-Hillas (G-H) function [27],

$$N(X) = N_{\rm max}\left(\frac{X-X_0}{X_{\rm max}-X_0}\right)^{\frac{X_{\rm max}-X_0}{\lambda}}\exp\left(\frac{X_{\rm max}-X}{\lambda}\right) \tag{1.17}$$

where X_0 is the atmospheric depth at the first interaction, $X_{\rm max}$ is the depth at which the air shower becomes maximum, $N_{\rm max}$ is the number of particles at $X_{\rm max}$ and λ is a scale parameter with the value of $\simeq 70$ g/cm^2.

1.3.5 Observation of extensive air showers

There are two common types of air shower detectors. One is the surface detector (SD) array on the ground to study the lateral distribution of the air showers. The air shower energy and arrival directions are reconstructed with the SD array. The other is the fluorescence detector (FD) that studies fluorescence and partially Cherenkov light emission. This technique is used only in the night without the Moon, hence the duty cycle becomes $\simeq 10\%$. But the energy of the air shower particles is detected calorimetrically, hence the hadronic model dependence of energy estimation using MC is less in the FD than in the SD. The FD also studies air shower maximum, which indicates cosmic ray composition. Figure 1.7 is the schematic view of the observation with each detector.

Observation methods described above utilize the atmosphere as a calorimeter which includes target, absorber and luminous layer. Such a methodology is used for UHECR since the atmospheric layer of the Earth has roughly 1000 g/cm^2 thickness.

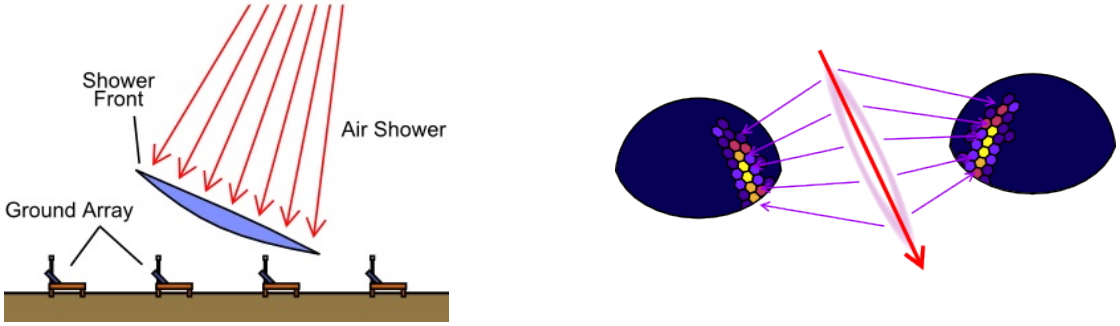

Figure 1.7: The schematic views of air shower observation [28]. (left) The observation using the SD array. (right) The observation using the FD.

1.4 Previous results

To understand the origin of UHECR, experiments have measured the spectrum, the composition and the arrival direction of cosmic rays. In this section we will follow the existing results and indications.

We will also introduce studies of muons in UHECR air showers. The interaction process of EAS is not fully understood, which provides the uncertainty for measurements of UHECR. It is significant to study muons in EASs to test hadronic models used in the MC calculation.

1.4.1 Spectrum

Figure 1.8 shows the spectra of cosmic rays from various EAS measurements. Figure 1.9 is the expanded view of the highest energy portion of the cosmic ray spectra measured by the TA and the Auger. The systematical flux discrepancy between the TA and the Auger in $E < 10^{19.5}$ eV is expected to be due to the systematic uncertainty in the measurements of energy with the FDs. There is the dip structure for both spectra at around $10^{18.7}$ eV where the spectrum index changes from -3.3 to -2.7. Both spectra also have cutoff above around $10^{19.7}$ eV for TA [12] and $10^{19.6}$ eV for Auger [29].

The existence of the dip and cutoff structure is common between these experiments, but the interpretation of the origin of the features is different. This is because the interpretation of the composition estimated from $X_{\rm max}$ measurement is different, although the TA and Auger composition working group reported that the data on $< X_{\rm max} >$ of the two experiments are in good agreement within systematic uncertainties if accounting for the different detector effects and analysis strategies of the two experiments [30]. The TA result indicates that light composition is favored in $10^{18.2}$ eV - $10^{19.8}$ eV, but in the Auger result a change in the composition is indicated, where the composition is lightest at $\sim 10^{18.3}$ eV and heavier above $\sim 10^{18.3}$ eV, as described in the next section. If the composition is proton, the dip structure is made by the electron-positron pair produc-

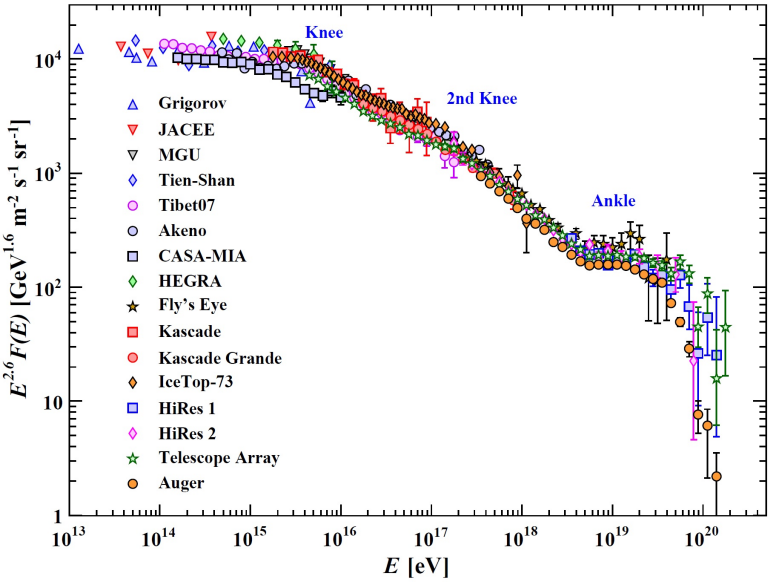

Figure 1.8: The spectra of cosmic rays from various EAS measurements [3].

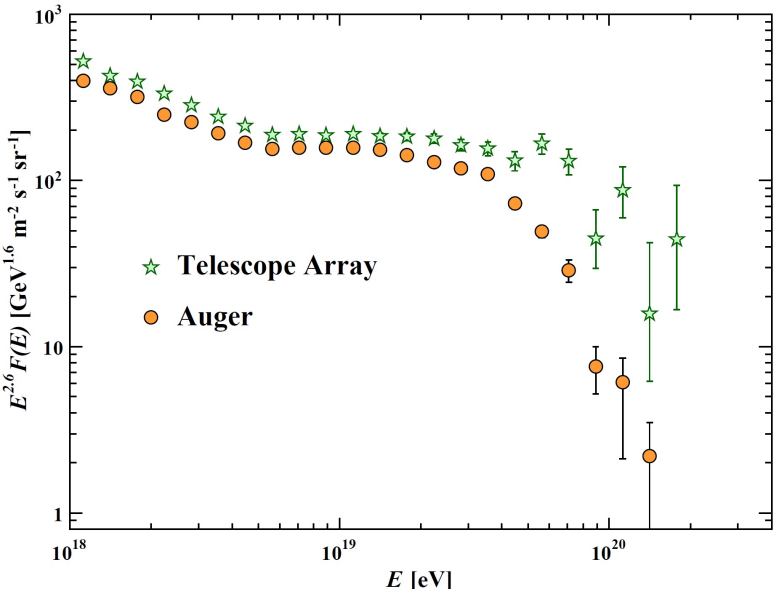

Figure 1.9: The cosmic ray spectra measured by the TA and the Auger [3].

tion reaction between proton and CMB photons, and the GZK cutoff is made by the photopion production reaction. If the composition is heavier nuclei, the cutoff is made by the photodisintegration reaction between nuclei and CMB photons. But the origin of the dip structure for heavy cosmic rays requires another interpretation, for example, an extragalactic flux beginning to dominate over the galactic flux [29]. In $E > 10^{19.5}$ eV, the difference of the flux between the TA and the Auger is broader. The difference can be interpreted as the difference of the cutoff energy, but the cause of the difference is unrevealed.

1.4.2 Composition

The mass composition of the UHECR is estimated by the measurement of the depth of the air shower maximum ($X_{\rm max}$). $X_{\rm max}$ is a quantity that correlates strongly with the interaction cross section of the primary particle. If heavy nuclei have the same energy as a proton, the energy per nucleon in the nuclei is smaller than the proton energy. Then the heavy nuclei develop faster and produce smaller $X_{\rm max}$ than proton. Figure 1.10 is $X_{\rm max}$ distribution by the TA experiment in the energy range $10^{18.4}$ eV - $10^{21.0}$ eV. The data points are closer to the MC prediction of proton than that of iron. There are three FDs (named BR, LR and MD) in the TA site, and several methods are used for the $X_{\rm max}$ study to understand systematic uncertainty. Figure 1.11 - 1.13 are the elongation rate of $X_{\rm max}$ from the TA experiment. Figure 1.14 shows the elongation rate of $X_{\rm max}$ from the Auger Observatory. The TA result indicates that light composition is dominant from $10^{18.2}$ eV to $10^{19.8}$ eV. But in the Auger result the composition is lightest at $\sim 10^{18.3}$ eV, becoming heavier above the energy, and intermediate between proton and iron at $\sim 10^{19.5}$ eV. The Auger collaboration suggests that the extragalactic cosmic rays have a mixed composition [35].

1.4.3 Arrival direction

Using the data at energies above 10^{19} eV, there is no apparent deviation from isotropy in the TA data [21]. On the other hand, TA reported a cluster of events, which is called the hotspot, in the northern hemisphere at energies above 5.7×10^{19} eV of radius $\sim 20^{\circ}$ with 5 year data set [36]. The statistical significance of such a hotspot appearing by chance in an isotropic cosmic-ray sky is 3.4 σ. The hotspot also appears with the 7 years' TA data set [37]. Figure 1.15 shows the map of the observed UHECR arrival directions. The source astrophysical objects of the hotspot are studied by applying single source hypothesis to the MC simulation [38]. It found out the best-fit source coordinates and magnetic field parameters, but the source is not apparent.

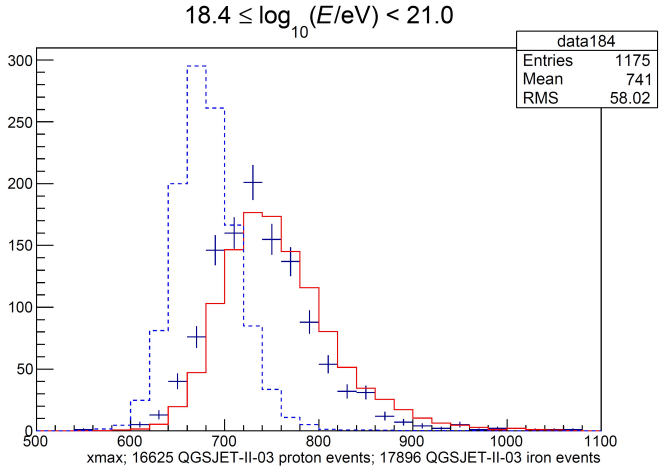

Figure 1.10: The reconstructed $X_{\max}$ distribution in the energy range $10^{18.4}$ eV - $10^{21.0}$ eV from TA FD stereo analysis [31]. The blue points, red solid line and blue dashed line represent 7 years' data, the MC prediction using QGSJETII-03 model for proton and that for iron, respectively.

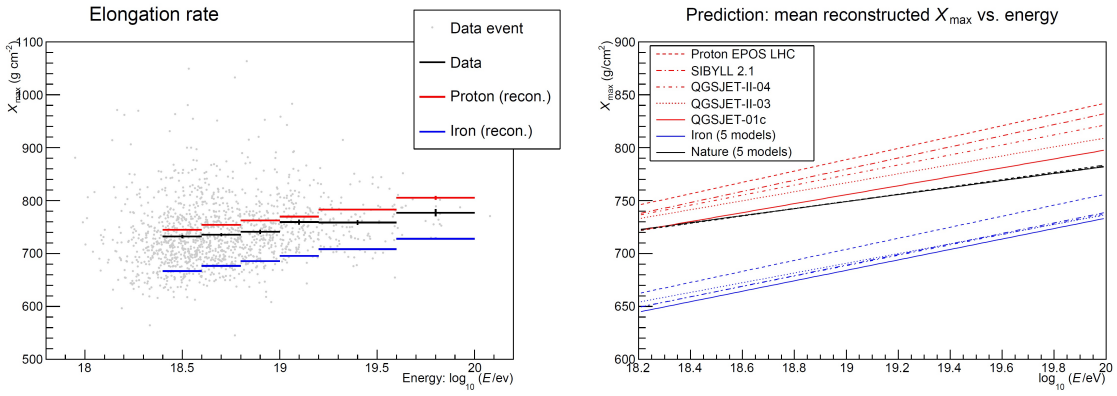

Figure 1.11: (left) The evolution of the mean reconstructed $X_{\max}$ with the reconstructed primary energy from TA FD stereo analysis [31]. The black represents the 7 years' data. The red and blue represent the MC predictions using QGSJETII-03 model for proton and that for iron, respectively. (right) Linear fits to the MC predictions for proton and iron using various hadronic models.

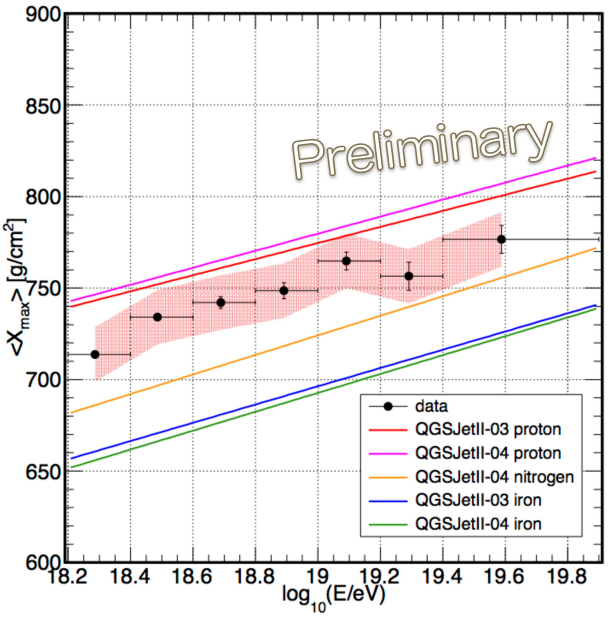

Figure 1.12: The evolution of the mean reconstructed $X_{\max}$ with the reconstructed primary energy from TA BR FD and LR FD hybrid analysis [32].

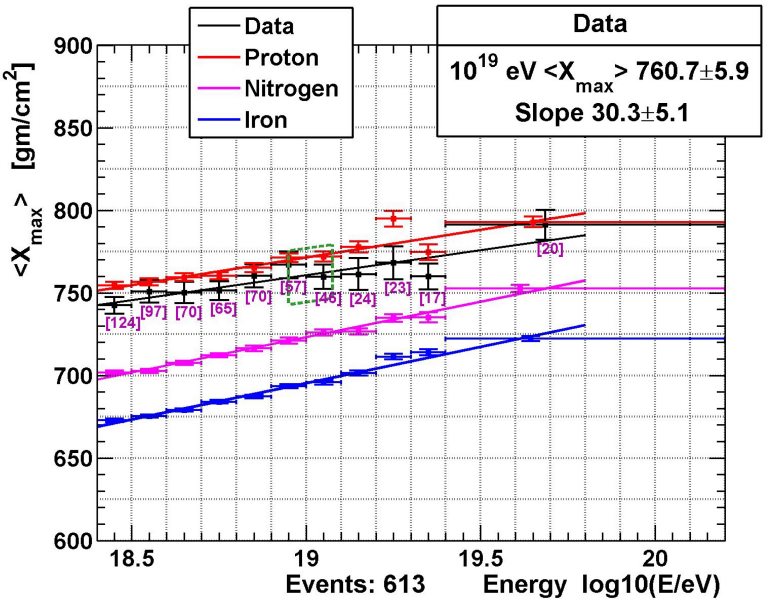

Figure 1.13: The evolution of the mean reconstructed $X_{\max}$ with the reconstructed primary energy from TA MD FD hybrid analysis [33].

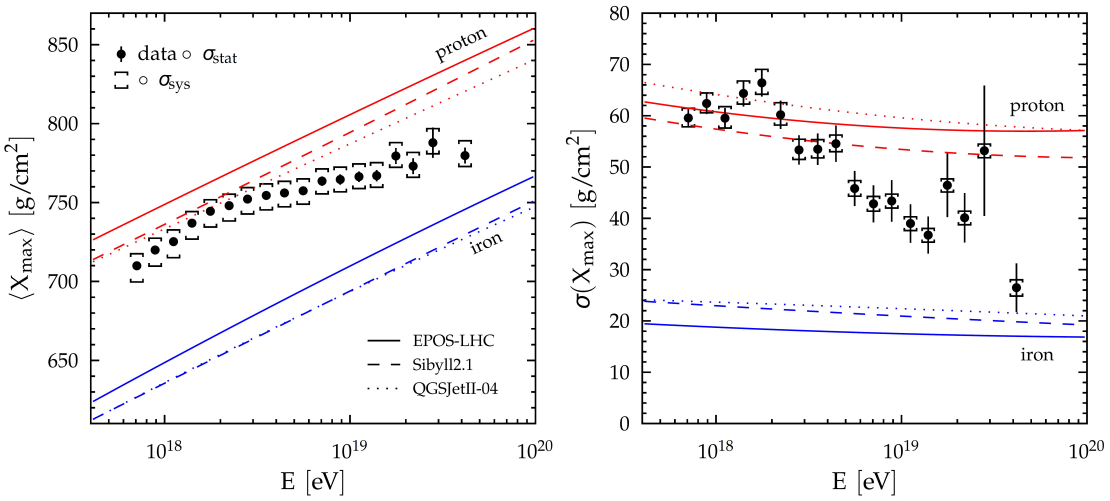

Figure 1.14: (left) The evolution of the mean reconstructed $X_{\max}$ with the reconstructed primary energy from the Auger analysis [34]. The black represents data. The red and blue represent the MC predictions for proton and that for iron, respectively using the hadronic models indicated in the figure. (right) The evolution of $\sigma(X_{\max})$ with the reconstructed primary energy from the Auger analysis.

1.4.4 Muon studies

The number of muons from air showers attenuates slower than that of electrons in the atmosphere. The disadvantage to use it as an energy estimator is that the expected number of muons by simulations depends on hadronic interaction models and the composition of primary cosmic rays. However it means that by comparing the measured number of muons with the simulation prediction, hadronic models can be tested.

The Pierre Auger Observatory reported several studies of muons from UHECR air showers. The Auger experiment does hybrid observation with the water cherenkov SD array and fluorescence detectors. Low energy EM components from air showers are absorbed in the water of the SD, and many of the signals consist of muons. The threshold energy of the Auger SD is about 0.3 GeV [11]. Here we will refer three studies of muons by the Auger experiment.

In the first study, the number of muons from air showers in the energy range $4 \times 10^{18}\text{eV} < E < 5 \times 10^{19}\text{eV}$ with zenith angles between 62° and 80° were measured with the SD [11, 48]. In the zenith angle above 62°, secondary particles from air showers are dominated by muons, since the EM components are largely absorbed in the large atmospheric depth crossed by the showers. Figure 1.16 shows the ratio of the EM to muonic contributions to the SD signal at the different zenith angles. Typically about 80% of the signal comes from the muons. When the showers reach the ground, signal patterns in the SD array with a narrow time period are obtained. The arrival direction

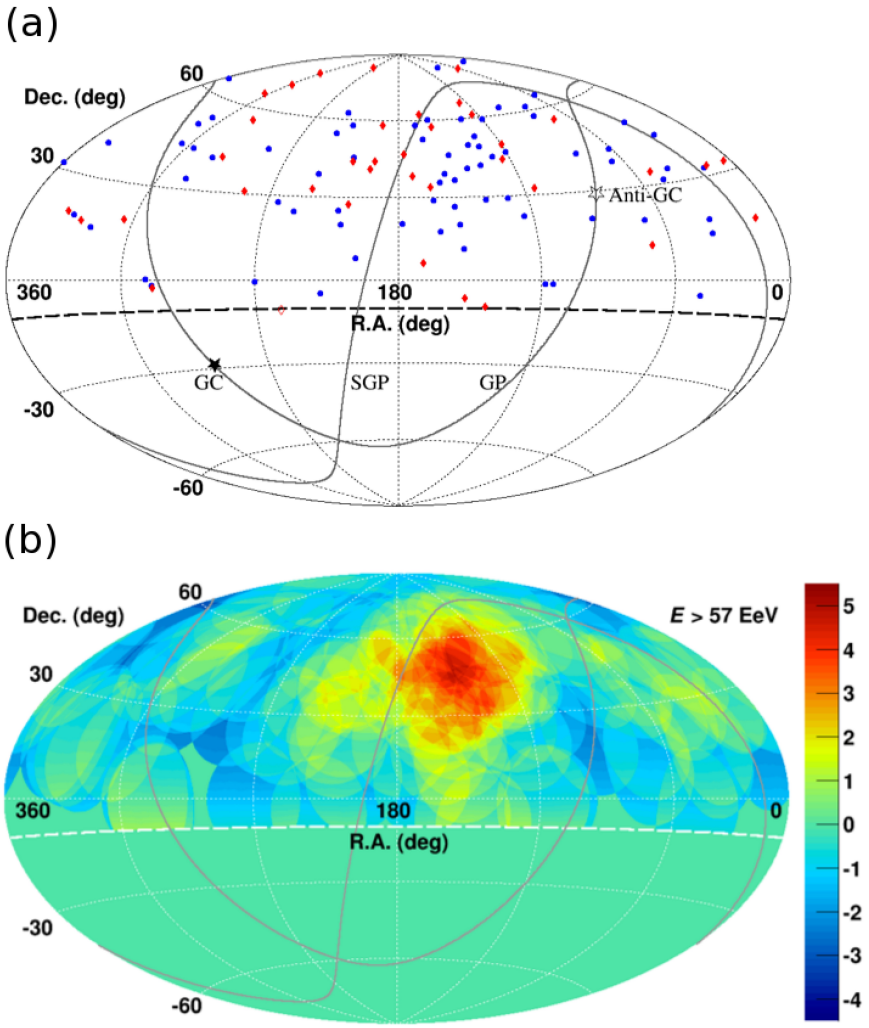

Figure 1.15: The hotspot of arrival directions of the UHECR with $E > 57$ EeV found by TA 7 years' observation [37]. (a) Aitoff projection of the UHECR maps in equatorial coordinates. The blue and red show the directions of the UHECR in the first 5 years' dataset and that in the later 2 years' dataset, respectively. (b) Significance map by oversampling using 20°-radius circles.

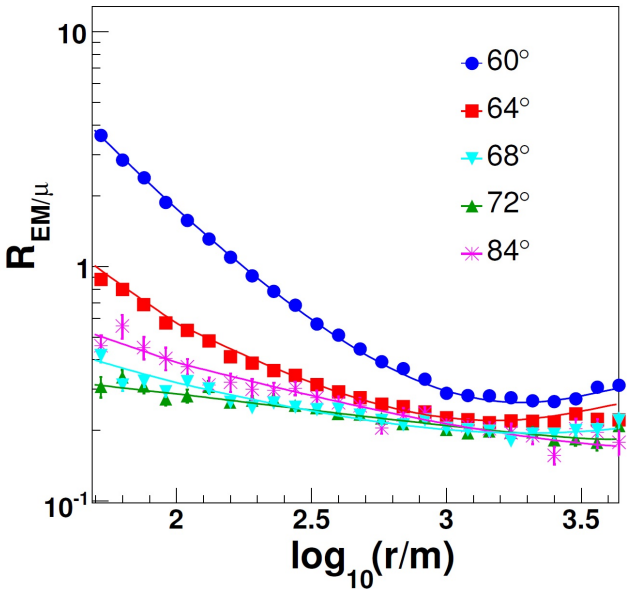

Figure 1.16: The ratio of the EM to muonic contributions to the Auger SD signal as a function of the distance from shower axis r, at different air shower zenith angle conditions indicated in the figure [48].

parameters (zenith angle θ and azimuth angle ϕ) of the cosmic ray is determined from the arrival time of the SD signal by fitting a model of the shower front propagation. Then from the measured SD signals, the muon signal is calculated using the ratio of the EM to muonic contribution to the signals expected from the MC using QGSJET01 model [49], which is described in figure 1.16. Next, the signal is fitted with the model of muon density ρ_μ at the ground point $\vec{r}$;

$$\rho_\mu(\vec{r}) = N_{19}\rho_{\mu,19}(\vec{r};\theta,\phi) \tag{1.18}$$

Here $\rho_{\mu,19}$ is the simulated muon density at $E = 10^{19}$ eV with QGSJET Ⅱ-03 model for proton. N_{19} is the scale factor, which corresponds to the ratio of the number of muons on the ground at the analyzed energy to that of the MC at $E = 10^{19}$ eV. The value N_{19} obtained by the MC has a bias by about 3% relative to the true value, which is the simulated ratio of the total number of muons to the integrated value of $\rho_{\mu,19}$ on the ground. Hence the N_{19} value is corrected for the averaged bias and the corrected estimator is called R_μ. The R_μ value was compared with the energy measured by the FD using hybrid events. Figure 1.17 shows the correlation between R_μ and the FD energy. The plots are fitted by

$$< R_\mu >= a(E/10^{19}\mathrm{eV})^b \tag{1.19}$$

where a and b are the fitting parameters. The parameter a expresses the average muon content $< R_\mu >$ at 10^{19} eV and the fitting result shows $a = 1.841 \pm 0.029(\mathrm{stat.}) \pm$

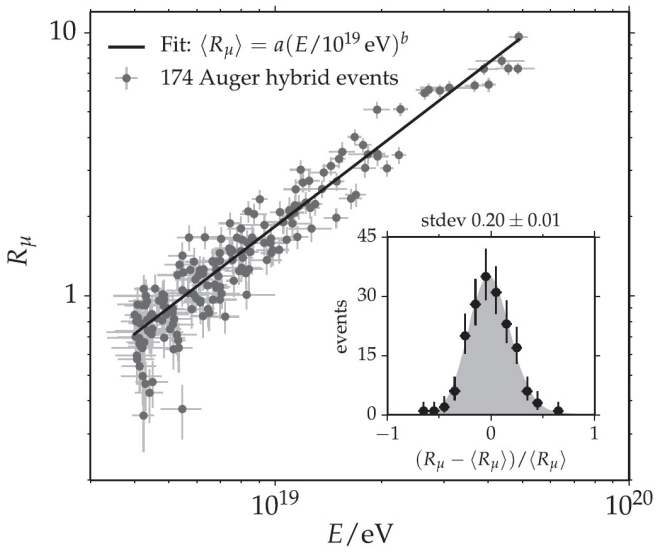

Figure 1.17: The scatter plot of the ratio of the number of muons of the data in each primary cosmic ray energy to that of the MC at $E = 10^{19}$ eV for proton using QGSJET II-03 [11]. The fit line is from the equation (1.19). The inset shows a histogram of the residuals around the fitted curve.

0.324(syst.). This means the measured number of muons is about 1.8 times larger than the MC prediction value. The systematic uncertainty of $< R_\mu >$ is 18%, which consists of R_μ-measurement (11%) from the hadronic model uncertainty of the bias of N_{19} [11] and the uncertainty of the simulated muon response of the detectors [50], and the uncertainty of the Auger FD energy measurement (14%) [51]. Figure 1.18 is the energy dependence of the R_μ value divided by $(E/10^{19}$ eV). The data is larger than the MC with QGSJET II-03 model by about 1.8 times in the energy range $4 \times 10^{18}\mathrm{eV} < E < 5 \times 10^{19}\mathrm{eV}$. Using the hadronic interaction models QGSJET II-04 [40] and EPOS-LHC [41], which are created referring to the results of the LHC experiment (*cf.* section 1.5), the number of muons of the MC becomes larger but still inconsistent with the observed value. From the results, the Auger group concluded that there is a muon deficit in the MC.

In the second study, the muon and EM contributions of the Auger SD signal is calculated by the MC, and compared with the Auger SD data to test the hadronic models [87]. The energy range is $10^{18.8}\mathrm{eV} < E < 10^{19.2}\mathrm{eV}$, where the mass composition changes rather little [34, 53] and zenith angles within 0° - 60°. In the analysis, the observed SD signal at the distance 1000 m from shower axis, S(1000), is compared with that of the MC *event by event*, using hybrid events. Simulated events which match the observed longitudinal profile of each event are selected for comparison to reduce shower-to-shower fluctuations. In the zenith angle $\theta < 60°$, the signal consists of both EM and muon components, as shown in the figure 1.19 [87]. The air shower component description in

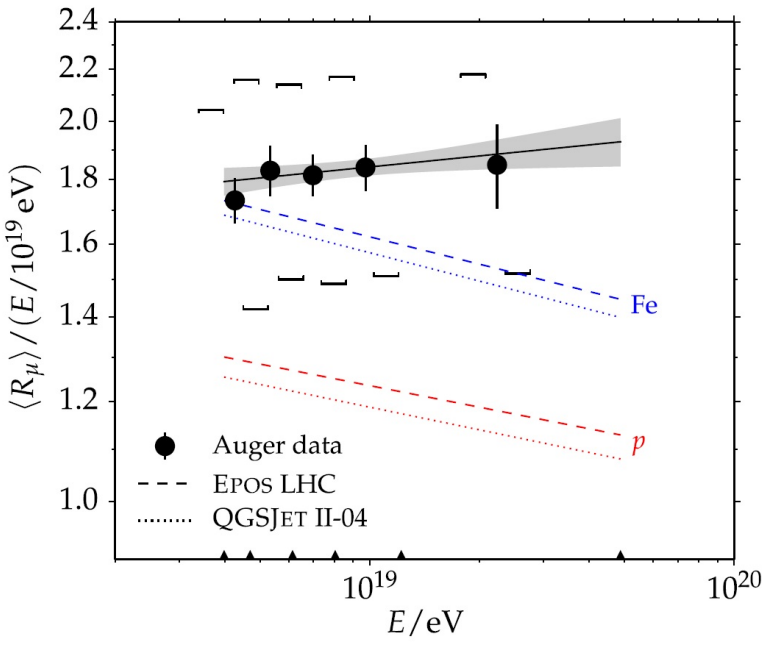

Figure 1.18: Energy dependence of the average ratio of the number of muons from air showers of the Auger SD data to that of the MC [11]. Here R_μ in the figure represents the ratio of the number of muons of the data to that of the MC at $E = 10^{19}$ eV using QGSJET II-03 for proton. Square brackets indicate the systematic uncertainty. The grey band indicates the statistical uncertainty of the fitted line of data plots. The red and blue represent the MC prediction values for proton and iron, respectively. The dashed and dotted lines represent the MC prediction values using EPOS-LHC and QGSJET II-04 models, respectively.

the figure follows the simulation study [52], which includes the muon component from $\pi^{\pm}$ or K decay, the EM component from π^0 decay, the EM component from muon interactions and muon decay, the EM component from low-energy hadrons (jet component) and muons that are produced through the photoproduction reaction. The muon signal is roughly independent of the zenith angle, while the EM signal falls with $\sec\theta$. In order to characterize the possible discrepancy between the data and the MC, the MC signal is separated into two components; the EM shower component and the hadronic shower component. Most of the ground EM (muon) signal derives from the former (latter) component.

In each hybrid event, the observed S(1000) is compared with the following function.

$$S_{\rm resc}(R_E, R_{\rm had})_{i,j} \equiv R_E S_{{\rm EM},i,j} + R_{\rm had} R_E^{\alpha} S_{{\rm had},i,j} \tag{1.20}$$

Here R_E and $R_{\rm had}$ are the scaling factor for EM and hadron shower components, $S_{\rm EM}$ and $S_{\rm had}$ are the signals of EM and hadron shower components calculated by the MC and R_E^{α} is the correction factor which reflects the difference of the energy dependence between EM and hadron components. i and j represent air shower ID and assumed primary mass, respectively. The R_E and $R_{\rm had}$ are determined so that $S_{\rm resc}$ maximizes the likelihood of the observed S(1000). The best fit values of R_E and $R_{\rm had}$ are shown in figure 1.20. Using the mixed composition determined from the Auger FD $X_{\rm max}$ observation, R_E results are 1.00 ± 0.10 for EPOS-LHC model and 1.00 ± 0.14 for QGSJET Ⅱ-04 model. This means the EM component does not need rescaling. But the $R_{\rm had}$ results are 1.33 ± 0.16 for EPOS-LHC model and 1.61 ± 0.21 for QGSJET Ⅱ-04 model. The Auger group reported that this result corresponds to an excess of muons in the data.

In the third study of the Auger group it is claimed that the arrival times of the muons on the ground provides information about the longitudinal development of the muon component of air showers [42, 43]. Using the particle arrival time in the Auger SD for showers with zenith angles around 60°, a distribution of muon production depth (MPD) and the muonic shower maximum $X^{\mu}_{\rm max}$ are reconstructed. The $X^{\mu}_{\rm max}$ depends on the primary cosmic ray mass composition so it can be an observable to infer the composition from the SD array. Figure 1.21 shows the evolution of the measured $X^{\mu}_{\rm max}$ with energy. The $X_{\rm max}$ and $X^{\mu}_{\rm max}$ values are correlated to the primary cosmic ray mass number A [54, 55]. Both parameters can be converted to $< \ln A >$ using the same hadronic models [42, 43]. Figure 1.22 shows $< \ln A >$ in each energy converted from $X_{\rm max}$ and $X^{\mu}_{\rm max}$. QGSJETⅡ-04 iron is within error bar of the Auger data above $\sim 3 \times 10^{19}$ eV, but it is not consistent with $X_{\rm max}$ results. The Auger group suggests that none of the models provides a consistent description of both the EM and muon components for the Auger data.

At the lower energy, there are researches on air shower developments with the accelerator. The accelerator experiment is related to air shower muon studies because almost muons on the ground from air showers derive from π or K particles generated at the

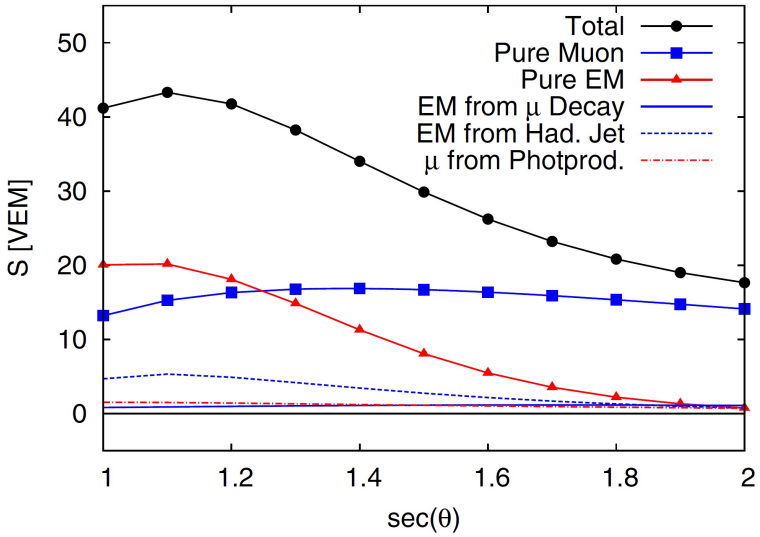

Figure 1.19: The contributions of different components of air showers to the average signal as a function of zenith angle [87]. The simulated 10^{19} eV proton showers with QGSJET II-04 model is used. The longitudinal axis represents the signal size at 1000 m from the shower axis, S(1000). The differences of markers and lines indicate the difference of the air shower components.

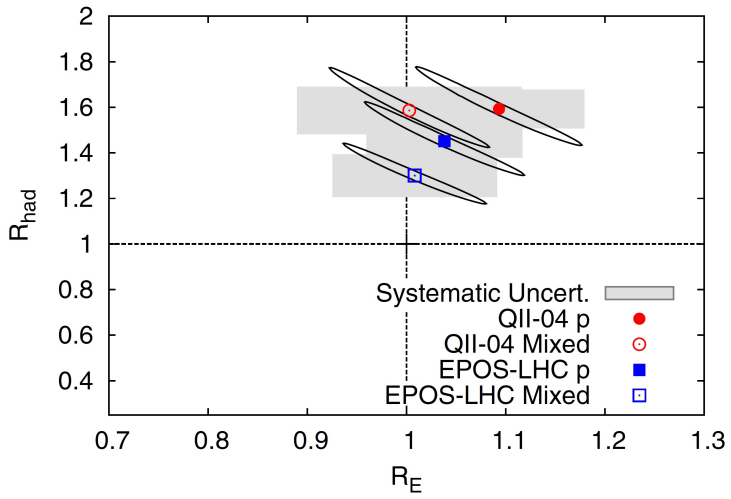

Figure 1.20: The best-fit values of the ratio of the data to the MC in the EM (R_E) and the hadronic shower component ($R_{\rm had}$), using QGSJET II-04 and EPOS-LHC models for the mixed composition estimated by the Auger FD measurement [87]. The ellipses and gray boxes show the statistical and systematic uncertainties, respectively.

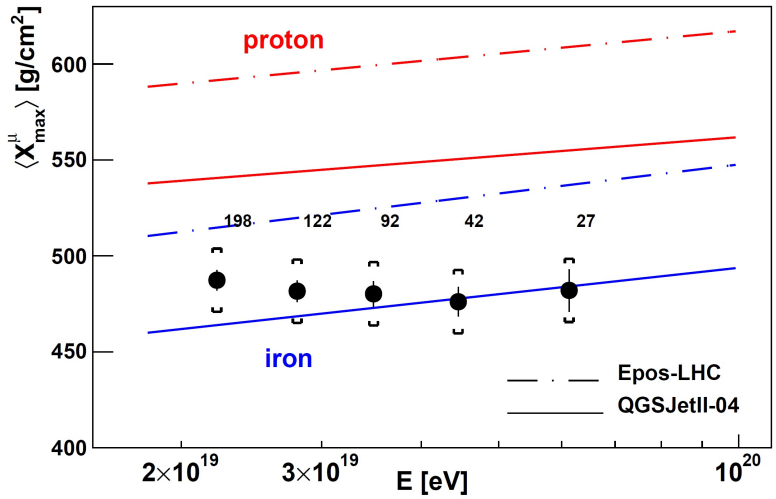

Figure 1.21: Evolution of the measured $X^{\mu}_{\rm max}$ with energy observed with the Auger SD [43]. The number of events is indicated in each energy bin.

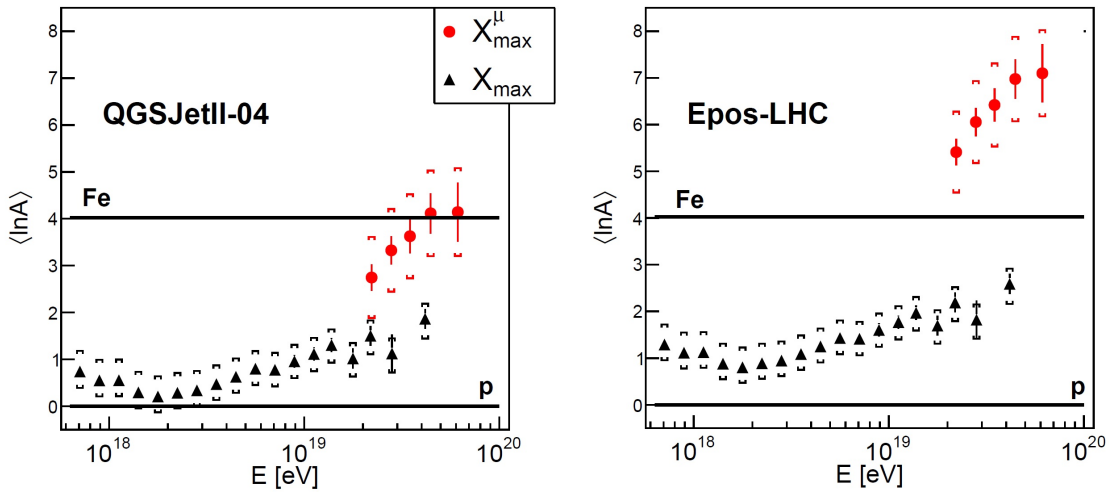

Figure 1.22: Energy dependence of $< \ln A >$ value calculated by $X_{\rm max}$ and $X^{\mu}_{\rm max}$ observed by the Auger experiment [43]. Here A represents the cosmic ray mass number.

early stage of the shower development. The LHC forward detector (LHCf) experiment [45] is designed to measure the hadronic production cross sections of neutral particles (such as π^0 [45] or neutron [46]) at very forward angles in proton-proton ($p+p$) and proton-lead ($p+\mathrm{Pb}$) collisions. The experiment showed the π^0 production cross sections as a function of transverse momentum (p_T) and longitudinal one (p_z) [45], and tested hadronic models in $p+p$ collisions at 2.76 and 7 TeV center-of-mass energy $\sqrt{s}$. Here $\sqrt{s} = 7$ TeV corresponds to the cosmic ray energy 2.6×10^{16} eV in the target rest frame. The experiment also tested hadronic models in $p+\mathrm{Pb}$ collisions at $\sqrt{s_\mathrm{NN}} = 5.02$ TeV. The results show that existing hadronic models do not produce full agreement with the data, though some of the models agrees well in a certain condition (for example, QGSJET Ⅱ-04 shows an overall agreement with the data in $p+p$ collisions, but not in $p+\mathrm{Pb}$ collisions) [45].

The KASCADE-Grande observatory pointed out a possible discrepancy between the measured and the predicted values of the attenuation length of EAS in the energy range $10^{16.3}$ eV - $10^{17.3}$ eV [44]. The attenuation length was obtained by measuring zenith angle dependence of the number of muons from air showers and is compared with the MC prediction value. The results showed that the measured value deviates from the predictions of the various hadronic models, ranging from +1.93 σ to +2.63 σ . Figure 1.23 is the lateral distributions of muon density in each energy and zenith angle condition. In the figures the MC predictions for a light (H + He) and a heavy (Si + Fe) composition are drawn. The predicted density changes faster than the measured value as the zenith angle increases. In addition, the measured density indicates heavier composition as the energy increases, being located at the upper limit of the MC predictions in the zenith angle $35.1^\circ \leq \theta \leq 40^\circ$. The KASCADE group indicates that this effect may be connected with the muon excess measured at the Pierre Auger Observatory at higher energies.

1.5 Purpose of study of muons from air showers

To understand the origin of UHECR, the observation of cosmic ray mass composition is important because cosmic rays are deflected in the galactic and extragalactic magnetic fields. But UHECR air showers are not fully understood. The present maximum energy of hadron interactions artificially made by an accelerator is around 10^{17} eV in the target frame performed by the LHC experiment. The MC for cosmic rays in the energy above 10^{18} eV uses the extrapolated values for the parameters of hadron interactions, such as cross section, multiplicity and rapidity. The values of these parameters are different among hadronic interaction models, due to the uncertainty of modeling pion or kaon generation at the early age of the air shower development. That causes the model uncertainty of the results of UHECR composition observation. In addition to that, the Pierre Auger Observatory reported that the number of muons measured with water Cherenkov detectors is larger than the MC prediction, as described in section 1.4.4. The Auger group claimed the excess of muons in the data [87].

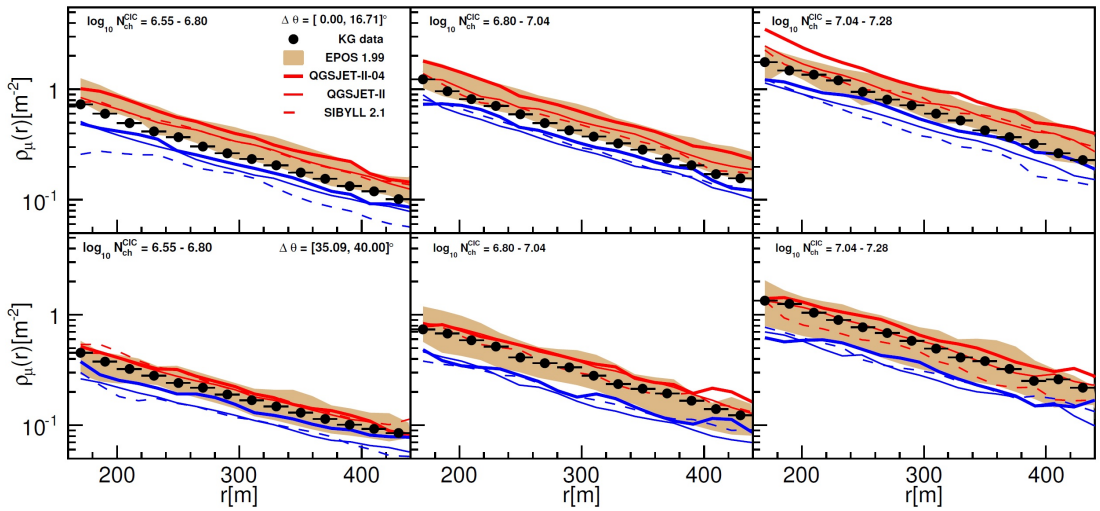

Figure 1.23: The lateral distribution of muons from air showers in the energy range $10^{16.3}$ eV - $10^{17.3}$ eV obtained by the KASCADE-Grande observatory [44]. The red lines are the MC predictions for a heavy composition (Si + Fe), while the blue lines are for a light composition (H + He). The upper panels show zenith angle condition within $[0°, 16.7°]$ and lower panels show $[35.1°, 40°]$. Three columns are divided by $\log_{10} N_{\rm ch}^{\rm CIC}$ conditions, where $N_{\rm ch}^{\rm CIC}$ is the number of charged particles that a shower could have at $\theta = 22°$. The difference of $N_{\rm ch}^{\rm CIC}$ corresponds to the difference of the primary energy.

The analysis of air shower components provides the information to obtain a realistic air shower model. The number of muons from UHECR air showers on the ground depends on the composition of primary cosmic rays. Its MC prediction also depends on hadronic interaction models since it has an information about the shower propagation at the early stage. One may test the hadronic interaction models by comparing the measured number of muons with the MC prediction. In the previous studies by the Pierre Auger Observatory, the total number of muons at the SDs [11] and the number of muons at 1000 m distance from the shower axis [87] were analyzed. However, to study the shower structure, it is necessary to analyze the lateral distribution of the number of muons. This work aims to separate the air shower EM and muon components in the TA SD signal, and study the lateral distribution of the number of muons on the ground. The TA experiment uses the SD made of plastic scintillator. It is sensitive to the EM component that is the major part of secondary cosmic rays from UHECR air showers, including electrons converted from gamma rays in the scintillator. A new analysis approach to increasing muon purity is necessary to calculate the number of muons in the TA SD data. The analysis strategy is as follows:

1. Assume the cosmic ray mass composition is proton.

2. Search for the analysis condition where the muon purity in the SD signal becomes high using the MC.

3. Compare the observed signal size from air shower particles with the MC prediction value on the muon-enriched condition.

The thesis is organized as follows. In chapter 2, the Telescope Array detectors are described and the condition for taking data is summarized. In chapter 3, the MC simulation methodology and its reliability is explained. In chapter 4, the analysis framework of muon analysis and the factors that contribute to the systematic uncertainty of the results are explained, and the analysis results are presented. In chapter 5, the requirement to the hadronic models from the results and the comparison of this work with the Auger results are described. Finally, concluding remarks which we found in chapter 6,

2 Telescope Array experiment

2.1 TA detectors

2.1.1 Overview

The Telescope Array (TA) experiment is designed for measuring EAS induced by the UHECR arriving in the Earth [56]. The TA site is located in Millard County, Utah, USA, and 1370 m above the sea level, 876 g/cm^2 vertical mass from the top of the atmosphere to the center of the site. The TA consists of 507 plastic scintillator surface detectors (SDs) and three fluorescence detectors (FDs). The SDs are placed on a square grid with 1.2 km spacing, covering about 700 km^2 area on the ground. The FD stations are located around the SD array, looking towards the sky above the SD array. Three FD sites are called Black Rock Mesa (BR), Long Ridge (LR) and Middle Drum (MD). Figure 2.1 shows a layout of the TA site. The triangles in the figure represent the communication towers; Smelter Knolls (SK), BR and LR which control SD array trigger of air showers and collect SD data in each sub-array. At the center of the site, a central laser facility (CLF) is installed for the calibration of the FD [57]. There is a control center for construction and operation of TA detectors in Delta city located to the east of the TA site.

The TA experiment aims at revealing the origin of the UHECR by observing the cosmic ray energy spectrum, arrival direction and mass composition. The measurement of UHECR with the SD is performed in the energy range $E > 10^{18.2}$ eV [12], while the FD monocular analysis covers $E > 10^{17.2}$ eV [62]. The TA detectors are continuously taking data since 2008. Figure 2.2 represents the exposure of the SD array and the FD monocular analysis of the BR and LR detectors. The TA SD array has nearly 100% duty cycle, and its exposure of the 7 year observation reaches 6300 km^2 sr year for $E > 10^{19}$ eV. While the TA FD has an advantage in terms of the detection area and solid angle coverage, the duty cycle is limited by daylight and weather conditions, making 10% duty cycle. Hence the exposure of the FD is smaller than that of the SD.

The TA SD has an advantage in the number of events in the spectrum and arrival direction measurements. The TA FD detects the full longitudinal profiles of air shower propagation in the atmosphere, hence the measurement determines the energy more accurately than the SD. Air shower events seen in coincidence between the TA FD and the TA SD are used for establishing the energy scale of the TA SD [12]. Also simultaneous FD and SD events measure the event geometry accurately and are used for determining the mass composition [33, 65, 66]. Such events are called hybrid events.

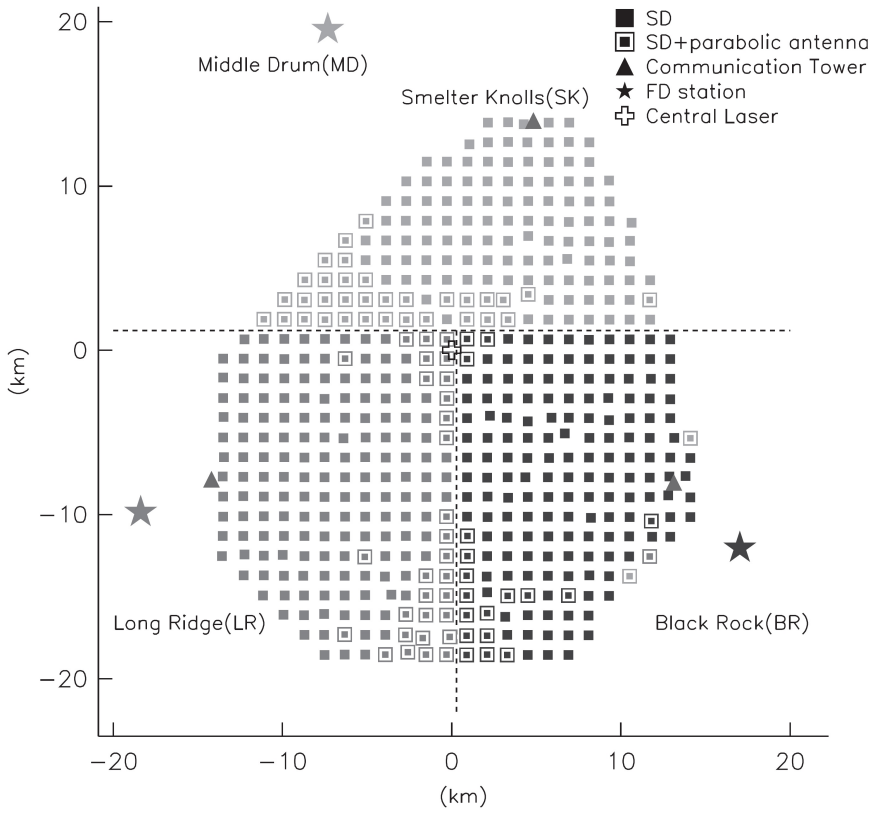

Figure 2.1: A layout of the TA site [58]. The dashed lines represent the boundary of three sub-arrays.

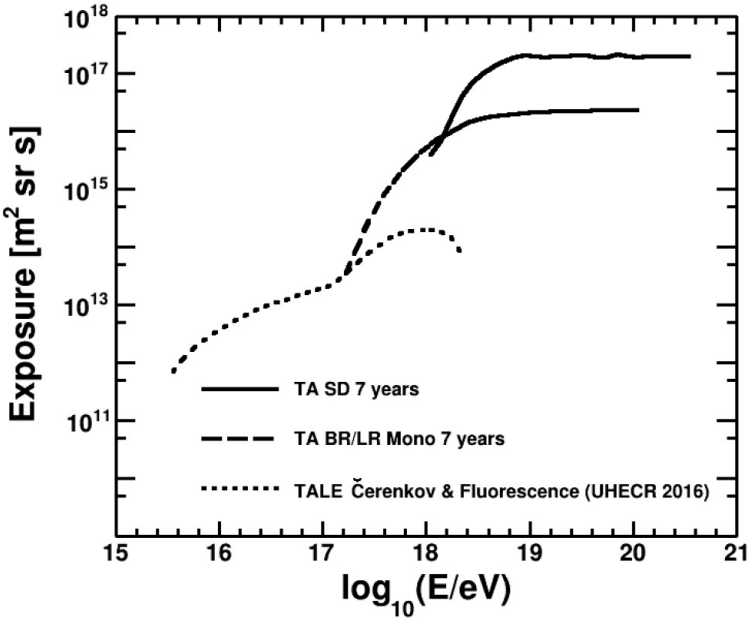

Figure 2.2: The exposure of the TA SD array and that of the TA FD using BR and LR for 7 year data [59]. Area × solid angle × efficiency × observation time for each detector is drawn.

2.1.2 Surface detector

Figure 2.3 shows an exterior view of the TA SD in the site. The TA SD is a plastic scintillation counter. The scintillator units which have area of 3 m^2 and photomultiplier tubes (PMTs) are enclosed in a box. The box consists of 1.2 mm thick stainless steel box with a 1.5 mm thick stainless cover. Figure 2.4 shows the inside schematics of a scintillator box. The scintillator unit consists of two layers of 2 m × 1.5 m × 1.2 mm scintillators. A stainless steal plate is placed between the layers, which has 1 mm thickness. When air shower particles arrive at the scintillators, photons generated in the scintillators are collected through wave length shifting fibers. Those photons are read out by PMT (Electron-tubes 9124SA) equipped at each layer.

The scintillator box is housed under an iron roof which have 1.2 mm of thickness. The roof protects the scintillators from large temperature variations due to direct sun light. The temperature range of inside scintillator is roughly from -20 °C to +50 °C [58].

A solar panel is mounted on the platform as shown in figure 2.3. Battery (DCH-100HIT) enclosed in electronics box is charged by the solar panel during the daylight. The power system ensures 100% data collection duty cycle. Data acuisition (DAQ) electronics is powered by the battery.

A GPS antenna is mounted on the roof. The time stamps of signals at all detectors are synchronized using commercial GPS module (Motorola M12+). With the GPS module, recorded pulse timing has accuracy of 10 ns [60].

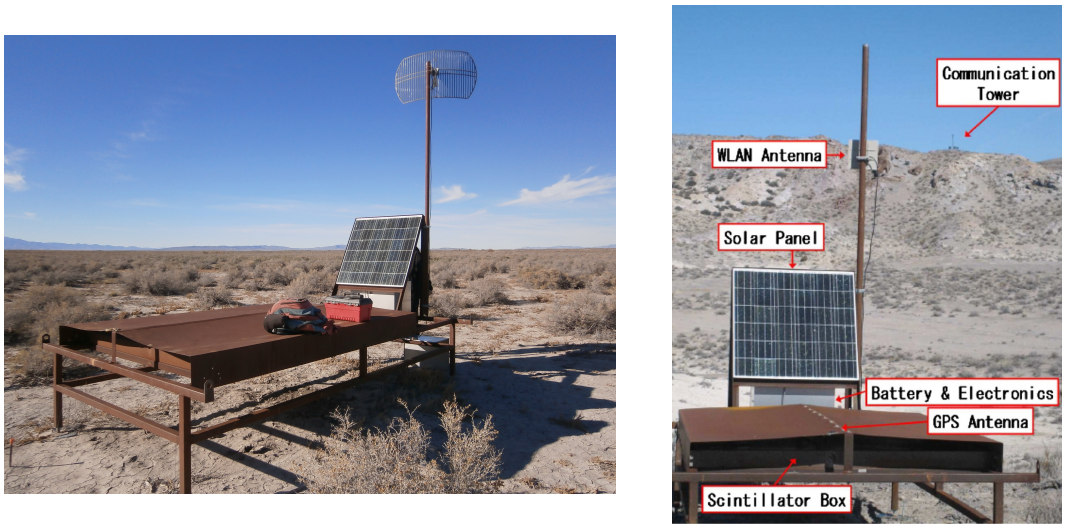

Figure 2.3: The TA SD deployed in the TA site. (left) The overview of the detector. (right) The explanation of each part [58]. The SK communication tower is seen behind on the hill.

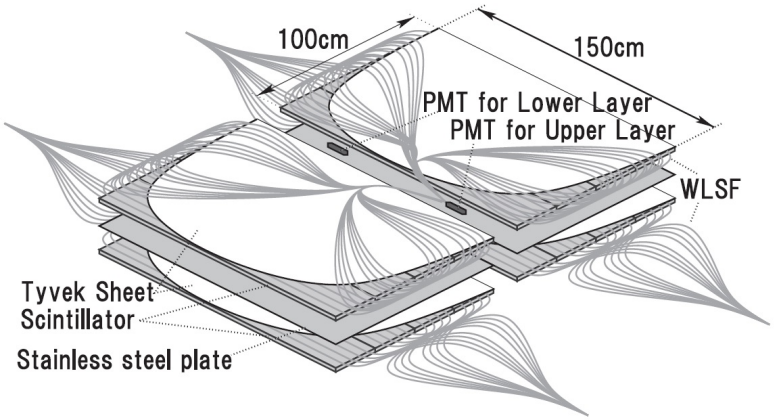

Figure 2.4: Inside of a scintillator box [58]. The wave length shifting fibers laid on the scintillators guide the photons generated by air shower particles. The fibers are bundled and attached to the PMTs at the edge.

Figure 2.5: The BR communication tower.

The signals from PMTs are digitized by a commercial 12-bit Flash Analog-Digital Converter (FADC) and stored in a memory. The sampling rate is 50 MHz. The digitized PMT signal is called the waveform. The waveform is recorded with 2.56 μs of flame length (128 time bin).

An energy deposition of a vertical muon at minimum ionizing energy (injection energy 300 MeV) is approximately 2 MeV. The value is dened as 1 MIP, which corresponds to about 50 counts in the unit of integrated FADC values. Signals which have the integrated FADC values larger than 15 counts ($\sim$ 0.3 MIP) are stored in a memory buffer on CPU board. The trigger condition is called the Level-0 trigger, which has the rate of $\sim$ 750 Hz. The waveforms are sent to the communication towers when requested. Signals greater than 150 counts ($\sim$ 3 MIP) is stored as the Level-1 trigger. The Level-1 trigger rate is $\sim$ 30 Hz. The list of the time stamp is sent to the trigger decision electronics equipped in a communication tower.

Figure 2.5 shows one of the communication towers. The communication and data transfer between a SD and a communication tower is done through a directional antenna equipped on 2.4 GHz wireless LAN modem (ADLINK540F). For the communication, a custom-made DAQ process is used [61]. The tower-to-tower communication is performed in 5.7 GHz band to avoid interference in the tower-to-SD communication.

2.1.3 Fluorescence detector

The SD array is overlooked by 38 FDs at three locations. The BR and LR stations each consists of 12 FDs and the Field Of View (FOV) of each FD is approximately 18° in azimuth and 15.5° in elevation [62]. The FOV of each station is determined from a combined coverage of the 12 FDs, which is $3° - 33°$ in elevation and 108° in azimuth. The

Figure 2.6: An exterior of the TA FD. (left) The overview of BR FD station. The shutters are set in three directions, which cover the FOV of four FDs each. The shutters protect the segment mirrors from sunlight, rain and dusts of the outside of the station when the observation is not performed. (right) The BR FD spherical mirror composed of 18 segment mirrors. In the figure the center position is covered for the maintenance.

FD has a spherical mirror with a diameter of 3.3 m, which is composed of 18 hexagonal segments. The mirror area of each FD is 6.8 m^2. The curvature radius of each segment mirror is 6067 mm. There is no mirror at the central position of the segments and xenon flash lamp for the PMT calibration is installed there.

Figure 2.6 shows the exterior of the BR FD station and the segment mirrors inside it. The mirror surface is coated with 200nm aluminum produced by the vacuum deposition and 10.5 mm glass covers the backside. The reflectivity of the mirrors is larger than 90% for photons with 300 nm - 400 nm wavelength. Since the mirrors are exposed in the outside air during the observation, dusts on the mirror increase gradually and make the reflectivity lower by about 10% at maximum in a year. To recover the reflectivity, the mirror surface is washed by pure water once in a year.

Each camera consists of 256 hexagonal PMTs arranged in a 16×16 honeycomb array, installed at the focal plane of the spherical mirror. The camera surface is protected by the acrylic filter which has UV transparency. Each PMT is applied different voltage to provide uniform gain. The signals from each PMT are digitized by a 12-bit FADC with a 40 MHz sampling rate. The trigger electronics selects a track pattern of triggered PMTs in real time and recognizes air shower tracks on the camera or rejects accidental noise caused by night sky background, artificial light and so on [63].

The MD FD consists of 14 FDs and the FOV of the station is $3^\circ - 31^\circ$ in elevation and 112° in azimuth [64]. Each FD has 5.1 m^2 spherical mirror composed of four glass mirror segments each arranged in a cloverleaf shape. The camera is comprised of a cluster of 256 hexagonal PMTs. Each PMT is optimized to collect UV light and is provided with its own high voltage setting to provide uniform gain.

2.2 Data taking condition

The TA SD data consists of the air shower event data and monitoring data with the GPS time information. To achieve timely storage and retrieval of the data, and to optimize the required storage space, the TA detectors implement an elaborate scheme of selecting and recording useful event and calibration information. In this section the data taking and recording processes are described.

2.2.1 Event data acquisition

Since most of the detectors are positioned nearly on the 1200 m square grid, X and Y numbering are used for the logical identification of each detector. Here X increases from west to east and Y increases from south to north. In the coordinate system, the CLF is located in 14.69 km east and 19.73 km north. Each detector position are measured in the unit of 1200 m grid. Then this scheme provides a labeling for every counter by one integer number (ID $= X \times 100 + Y$). This labeling scheme is used for data acquisition and also at the first stage of event reconstruction.

The data acquisition of air shower events is triggered by the module at the communication towers. Each tower uses the same electronics as the ones equipped in the surface detectors. But the firmware running in the electronics is different. The data communication between towers and SDs is done by 2.4 GHz wireless LAN using a custom-made communication protocol [61].

At each sub array, the trigger decision electronics at the tower requests a list of the Level-1 trigger ($\sim$ 3 MIP) event recorded at SDs at each second. When three adjacent SDs in the list are coincident within ± 8 μs, the tower electronics generates the Level-2 trigger. Possible pattern of position recognized as adjacent is shown in Figure 2.7.

When the Level-2 trigger is generated, the tower electronics send a command to SDs in the sub array to request the Level-0 trigger ($\sim$ 0.3 MIP) data within ± 32 μs from the event trigger time. Here the event trigger time is assigned as the time stamp of the Level-1 trigger detectors which first satisfy the condition of the Level-2 trigger. If SDs in sub array have the Level-0 signal within the requested time region, they send back detector position ID, waveforms and waveform time stamps with 20 ns resolution [80]. When one of three sub-arrays generate the Level-2 trigger, the time information is transmitted to SK tower to distribute other towers. Using the distributed trigger time information, other towers collect waveforms from SDs in the corresponding sub-array with the same time window if the tower does not have the Level-2 trigger at that time.

To collect air showers hit at boundary of sub-arrays, the level-1 trigger event lists from the SDs at the boundary of sub-arrays are sent to the SK tower. At the SK tower, the data acquisition PC run a trigger process which combines the Level-1 trigger information from SDs at the boundary. The trigger process apply the Level-2 trigger condition beyond the boundary. Also to deal with the event which two of the hit detectors are at the boundary but the other are not (possible in case pattern 1 or 6 of figure 2.7),

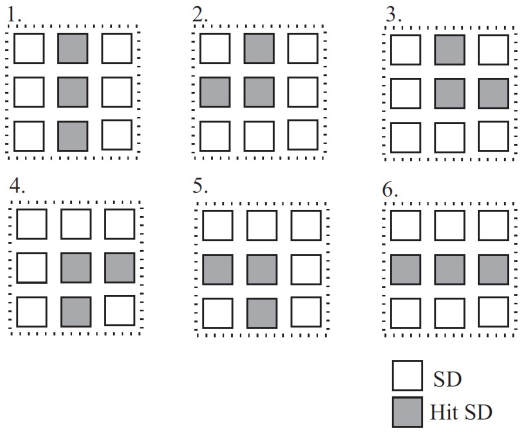

Figure 2.7: TA SD Level-2 trigger hit pattern [58]

central trigger process searches for the coincidence of two adjacent hits in the boundary detectors from Level-1 trigger lists. If such a coincidence exists, the central trigger process sends the trigger information to the other two towers, then each tower verifies the Level-2 trigger condition using the received information.

With the above trigger conditions, trigger efficiency is greater than 97% for a primary particle with energies above 10^{19} eV. Figure 2.8 shows the trigger efficiency in a sampled period as a function of energy of the primary particle obtained by CORSIKA air shower MC simulation [75] and GEANT4 detector MC simulation [76], which will be explained in detail in Chapter 3.

Low energy events ($< 10^{18.7}$ eV), which can be reconstructed by the FD but do not generate the Level-2 trigger patterns would be missed in the TA SD data. When the FD triggered the shower event, the SD data acquisition system at the nearest communication tower receives trigger from FD. The trigger is called "Hybrid Trigger". At a hybrid trigger, waveforms within 128 μs from the trigger timing are collected from each SD in the sub-array. The data acquisition scheme is the same as the Level-2 trigger with the longer time window. The longer time window is set because of the distance between the air shower and the FD telescopes. The efficiency of the waveform collection is greater than 97% for the primary particle with an energy of $10^{17.5}$ eV triggered by the FD [58].

Each FD telescope is instrumented with an imaging camera composed of 256 PMTs. The PMTs detect UV light from air showers. Two types of the FD trigger schemes are used, depending on the stations. For the BR and LR FD stations, there are three classes of triggers [63]. The signals from each PMT are sent to Signal Digitizer/Finder (SDF) modules [67]. One SDF module processes 16 input channels and 16 modules are installed for each camera (256 PMTs). The SDF has a 12-bit digitizer running at 40 MHz (25 ns/sample). If the digitized signal is greater than the pre-determined threshold, it sends an alert to the Track Finder (TF) module of the camera. This is called the "first level"

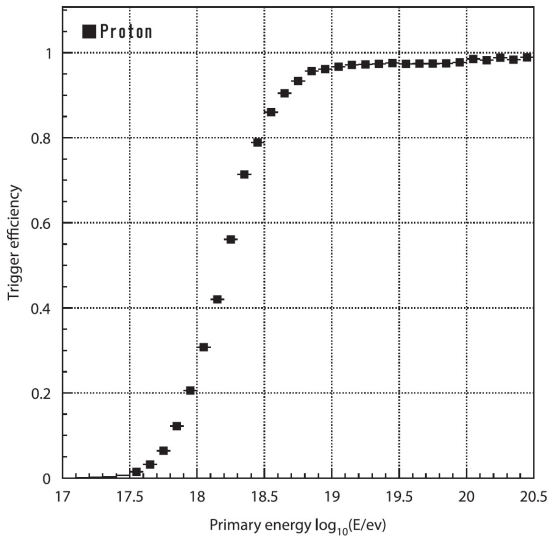

Figure 2.8: Energy dependence of TA SD Level-2 trigger efficiency in a sampled period [58].

trigger. The TF module is set in each FD telescope and collects the first level triggers from all 256 PMTs of the camera via the 16 SDFs. The hit pattern of the camera is compared with the trigger pattern table programmed in the RAMs in the TF module. If a match for a shower track is found, a "second level" trigger signal is sent to the Central Trigger Distributor (CTD) module, which deals with all the TFs of a FD station. When the CTD receives a second level trigger signal from one or more TFs, the module sends a "final" trigger signal to all of the cameras at the station to activate data recording processes for all signal channels. Then the waveforms of all the PMTs are recorded and the event time is calculated using the GPS time information in the CTD. The accuracy of absolute times is 20 ns [63].

The MD FD station has two trigger classes [64]. A "subcluster" (a 4×4 cluster of 16 PMTs within one camera) trigger occurs when three tubes trigger within a 25 μs time window, and two of them are adjacent. When two subclusters trigger within 25 μs window, a "telescope" level trigger occurs. Then the signals are converted digital signals through a 12-bit Analog to digital converter and recorded.

2.2.2 Monitoring data acquisition

To monitor the status of the detector and calibrate 1 MIP signal in the analysis after data acquisition, a monitoring process runs on each SD in a 10 min. cycle. The monitoring data are divided into 600 subsets and all the subsets are sent along with the Level-1 trigger tables every second. The acquisition and transfer of the monitoring data are synchronized by the GPS 1 second pulses (1-PPS). The monitoring data consist of the histograms and the status variables of every SD.

Figure 2.9 is an example of the time variations of the monitoring data. The most important information for the present work is the 1 MIP histograms. Muons at the minimum ionizing energy (around 300 MeV) are the most abundant atmospheric particles which penetrates the TA SD scintillator. So the Level-0 triggers are dominated by minimum ionizing particles. Histograms of the Level-0 signals (1 MIP) are used for determining the detector gain in FADC counts per MeV of energy deposition in each SD. The histogram is generated by integrating FADC counts of waveforms with the time window ranges between -4 bins from trigger timing and +8 bins after trigger timing. Here 1 bin corresponds to 20 ns. The pedestal histogram is also calculated to determine the base line of the FADC counts.

Figure 2.10 shows an example of 1 MIP histogram. The histogram shape consists of energy loss distribution and zenith angle distribution of atmospheric muons, the position dependence (non-uniformity) of the response of the SD, Poisson distribution of the number of photoelectrons generated at the surface of the PMT and so forth. The peak value of 1 MIP histogram calculated by the method explained in section 2.2.3 is monitored, as shown in the 6th panel of figure 2.9. The 1 MIP FADC value variation is caused mainly by the variation of outside temperature.

To understand the status of the GPS module, the visible number of satellites and conductivity of the antenna are read out in every 600s.

2.2.3 Detector calibration

The calibration is performed to determine the relation between the FADC values obtained at the SD and the energy deposition. It requires the simulated distribution of energy deposition by the atmospheric particles. The distribution are generated by the following procedure in a 10 min. cycle calibration [80, 61]:

1. Low energy cosmic rays with the power-law spectrum are simulated using CORSIKA air shower MC and the distribution of particles on the ground is generated. The cosmic rays in 3 GeV - 300 TeV energy range have major contribution.

2. An expected energy deposit distribution for atmospheric particles in the TA SD is calculated using Geant4 detector MC. Figure 2.11 shows an expected energy deposition distribution.

3. The expected energy deposition is smeared considering 7% Gaussian non-uniformity of the TA SD, the fluctuation of the number of photoelectrons following Poisson distribution and the pedestal fluctuation.

4. The 1 MIP histogram of the data is fitted with the simulated distribution calculated in the above procedure.

By the peak value of the fitting function, the conversion relation between FADC count and MeV units is obtained. In the analysis, the observed signal in the unit of FADC

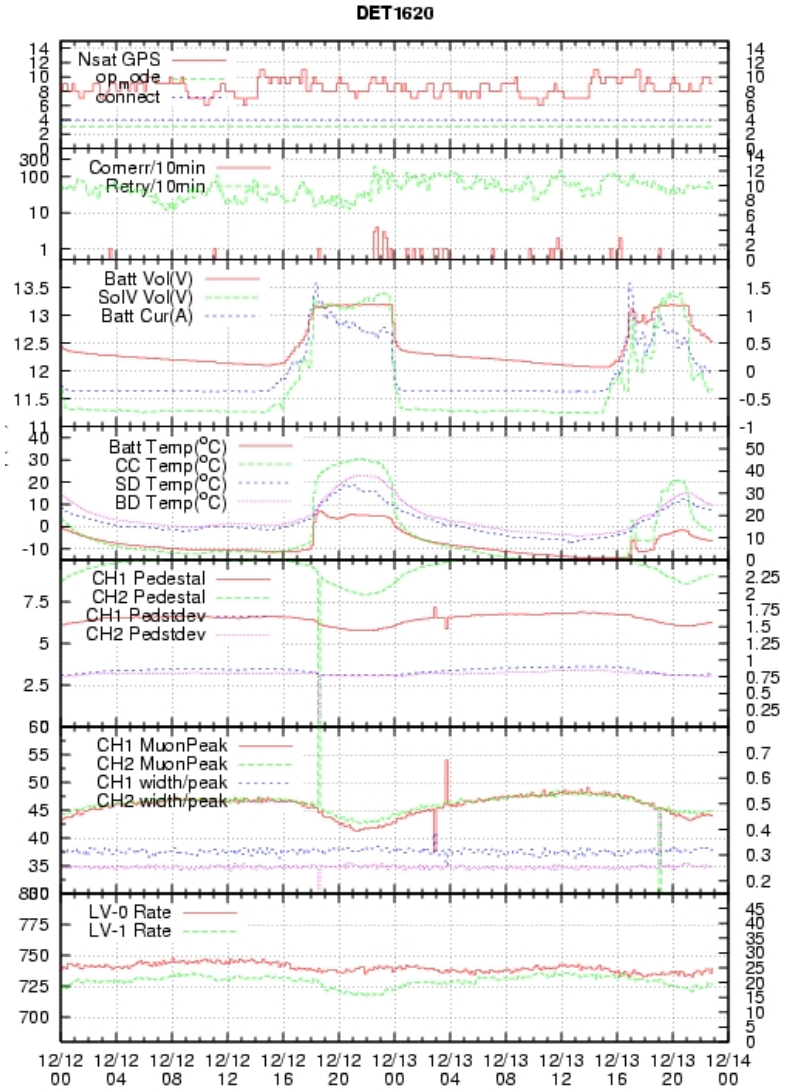

Figure 2.9: The sample monitor data in 12 Dec. 2016 - 14 Dec. 2016 UTC. The number of detected GPSs is shown in the 1st panel from the top. The 2nd panel shows communication status. In the 3rd panel, battery voltage, solar panel voltage and battery current are shown. The temperature measured at the various place in the SD is described in the 4th panel. The 5th and 6th panel shows the pedestal value and 1 MIP FADC value, respectively. The 7th panel describes the Level-0 and Level-1 trigger rate. There is a day-night variation in 1 MIP FADC value which has temperature dependence.

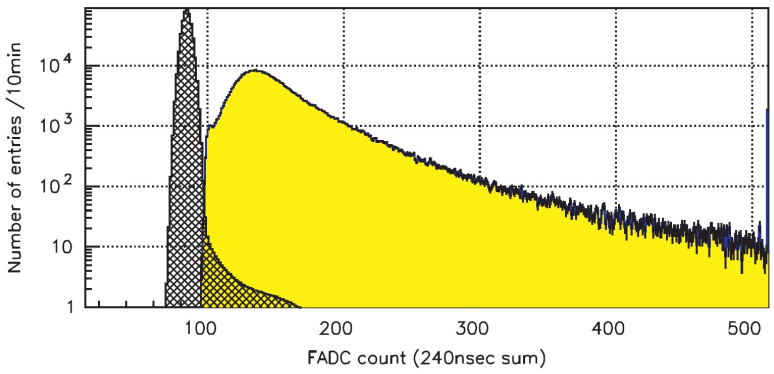

Figure 2.10: An example 1 MIP histogram, which is the histogram of the Level-0 trigger signals. The hatched histogram is a pedestal distribution. The pedestal distribution is scaled to have the same entry as the Level-0 trigger data.

count is converted to MeV units and the signal in MeV unit is converted to Vertical Equivalent Muon (VEM) units. The VEM unit is the most probable energy deposition of one vertical muon injection to the TA SD scintillator. The definition of VEM unit is 1 VEM $\equiv$ 2.05 MeV, that the relation is determined by the detector MC simulation described in section 3.2.

The linearity of the PMT output was checked by using two LEDs attached on the side of one scintillator inside the detector before SD deployment. When we describe the light amount of LED 1 and LED 2 as x_1 and x_2 and the peak of the pulse from a PMT in FADC count as $F(x_1)$ and $F(x_2)$, the linearity is measured by comparing $F(x_1 + x_2)$ with $F(x_1) + F(x_2)$ while changing x_1 and x_2. Figure 2.12 shows a typical example of measured relation between $F(x_1 + x_2)$ and $F(x_1) + F(x_2)$. The linearity variation in the operation after SD deployment is checked by monitoring the pulse-height histogram of FADC signal. The high voltage values of the PMTs of the detectors are adjusted so that the same 1 MIP FADC values are obtained for all detectors. Therefore if pulse-height histograms are different between detectors, it is due to linearity difference. The non-linearity is estimated by comparing the pulse height from each detector with that from detectors which have PMTs with good linearity.

The accuracy of determining 1 MIP FADC value is calculated by fitting the error of the 1 MIP histogram, which is 2% as described in section 4.3.2.

2.3 TA SD event reconstruction

The TA SD air shower events are reconstructed in four steps [80]. At first the SD signals that are related to air shower events are selected. Then the event geometry is determined by the arrival time distribution of air shower particles at the SDs. Following that, the lateral distribution of air shower particles is obtained in the signal size at each

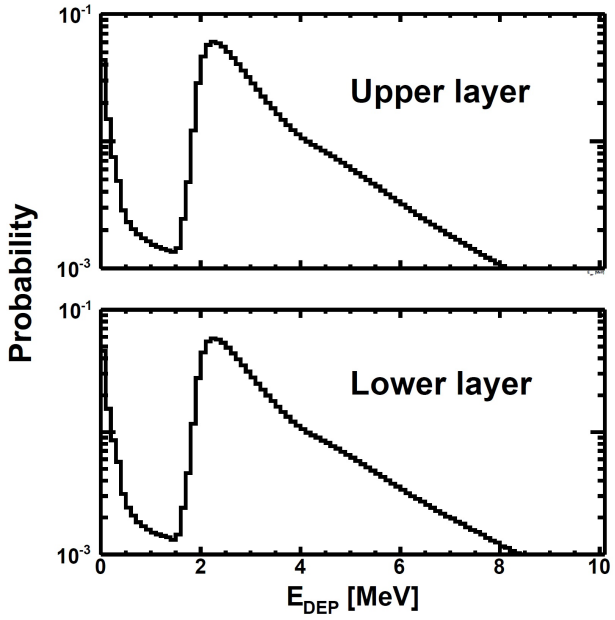

Figure 2.11: The expected energy deposition distribution by atmospheric particles calculated using CORSIKA air shower MC and Geant4 detector MC [80]. The upper and lower panels show the upper and lower scintillators, respectively.

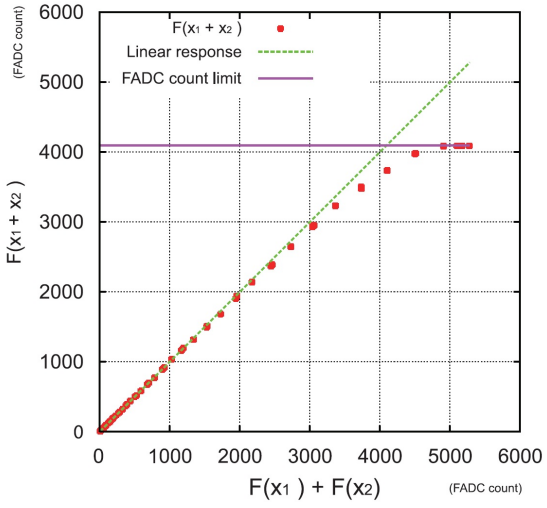

Figure 2.12: An example of measured relation between $F(x_1 + x_2)$ andt $F(x_1) + F(x_2)$ [58].

SD. Finally, The energy is determined by reconstructed parameters, using the energy scale obtained by the hybrid observation.

2.3.1 Signal selection

The first scheme of the event reconstruction is signal selection. For each event, all the detector waveforms are scanned by 80 ns (4 time bins) sliding window. If all 4 time bins of the sliding window exceed the pedestal by 5 σ in both upper and lower layers, the first time bin is regarded as the time of the signal. Here σ is the RMS of the pedestal per one time bin. Then if all 4 time bins of the sliding window are no longer larger than 5 σ, the time bin is considered as the signal end. This process separates the waveform into the multiple pulses in one waveform and reduce background signals from the random atmospheric muons, which occur at a rate of 700 Hz $\times$ 64 μs $\simeq$ 0.05 per counter within one event time period ($\pm$32 μs). After that, all pulses within 10 μs of the start time of the signal are summed and the integrated FADC values are obtained in each detector. Lastly, the average pedestal values are subtracted from the integrated FADC values, and they are converted to VEM units using calibration data.

Next, the SD which belongs to the air shower event is selected by determining a cluster which is contiguous in space and time. If the distance of the SDs are within $\sqrt{2}$ times of the detector separation unit (1200 m), the SDs are included in a cluster in space. Also if the time difference of the SDs are within their spatial separation divided by the speed of light, the SDs are included in a cluster in time. This procedure can exclude random atmospheric muons, which occurs uniformly in space and time. Figure 2.13 shows a display of sample clustered SDs decided by the above procedure.

2.3.2 TA SD geometry determination and energy estimation

The 5 parameters related to the air shower event geometry are decided by detector time distribution fitting; the time T_0 when the core of the shower hits the ground, the core position $\mathbf{R} = (R_{\rm x}, R_{\rm y})$, zenith angle θ and azimuth angle ϕ. Figure 2.14 shows the geometry of the parameters. The parameters are varied while minimizing the function:

$$\chi^2_{\rm G} = \sum_{i=0}^{N} \frac{(t_i - t_i^{\rm FIT})^2}{\sigma^2_{t_i}} + \frac{(\mathbf{R} - \mathbf{R}_{\rm COG})^2}{\sigma^2_{\mathbf{R}_{\rm COG}}} \quad , \tag{2.1}$$

where t_i is the i^{th} detector trigger time and $t_i^{\rm FIT}$ is the time of the i^{th} detector as predicted by the fit function. The form of $t_i^{\rm FIT}$ is

$$t_i^{\rm FIT} = T_0 + \frac{l}{c} + \tau \quad . \tag{2.2}$$

Here l is the distance between the detector and the shower plane at $T_0 = 0$,

$$l = (\mathbf{r} - \mathbf{R}) \cdot \hat{\mathbf{u}} \quad , \tag{2.3}$$

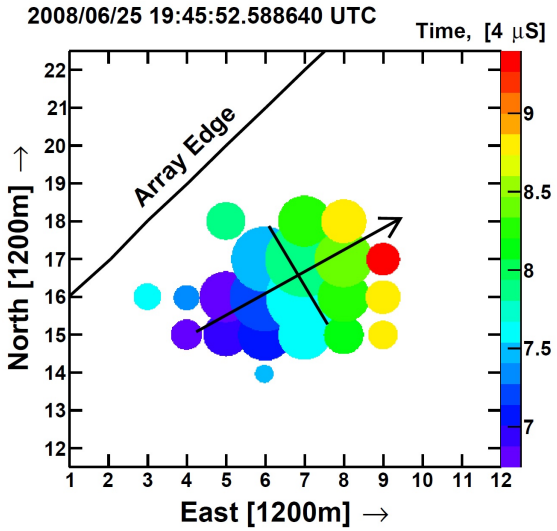

Figure 2.13: Sample event display of a typical TA SD event [86]. The circle centers correspond to the TA SD positions. The circle areas are proportional to the logarithm of the TA SD station pulse size. The circle colors represent the TA SD detection times relative to the detection time of the first triggered detector within the same ± 32 μs. The arrow shows the shower axis projected onto the ground and it is bisected by the perpendicular line at the location of the shower core.

where $\mathbf{r} = (x, y)$ is the detector position and $\hat{\mathbf{u}}$ is the unit vector of the shower axis projected onto the ground. τ is time delay due to shower front curvature effect and the function is tuned for TA SD data,

$$\tau = a \left(1.0 - \frac{l}{1.2 \times 10^3 \mathrm{m}}\right)^{1.05} \left(1.0 + \frac{s}{30\mathrm{m}}\right)^{1.35} \rho^{-0.5} \quad , \tag{2.4}$$

where a is a fit parameter, s is the distance between the detector and the shower axis. ρ is the integrated FADC values in VEM/m^2, that the FADC values obtained in the detector devided by the detector area (3 m^2). The uncertainty on the detector time σ_t consists of two components,

$$\sigma_t = \sqrt{\sigma_e^2 + \sigma_\tau^2} \quad , \tag{2.5}$$

where σ_e is the uncertainty due to the electronics, which is 20 ns [85]. σ_τ is the uncertainty on time delay,

$$\sigma_\tau = (1.56 \times 10^{-3}) \left(1.0 - \frac{l}{1.2 \times 10^3 \mathrm{m}}\right)^{1.05} \left(1.0 + \frac{s}{30\mathrm{m}}\right)^{1.5} \rho^{-0.3} \quad . \tag{2.6}$$

This function is also tuned from the TA SD data.

$\mathbf{R}_{\mathrm{COG}}$ is the center of gravity core position,

$$(R_{\mathrm{COG}})_{\mathrm{x}} = \frac{\sum_{i=1}^{N} \rho_i x_i}{\sum_{i=1}^{N} \rho_i} \quad , \tag{2.7}$$

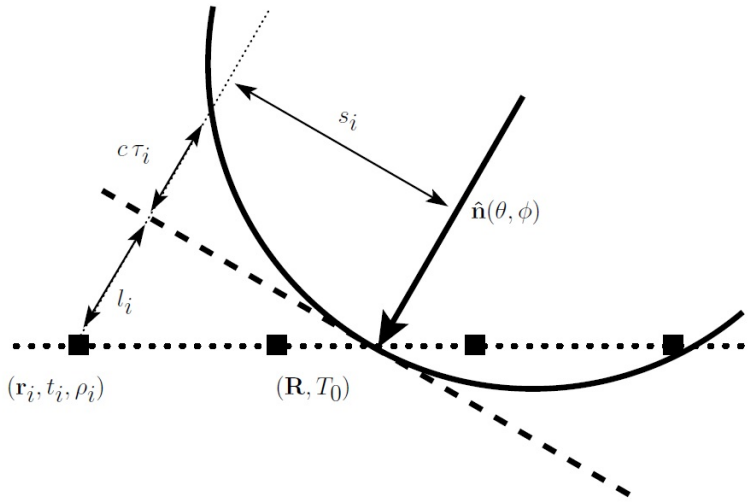

Figure 2.14: The schematics of the event geometry and the parameters at the time T_0 [80]. $\hat{\mathbf{n}}$ and s represents air shower axis vector and the distance from shower axis, respectively. Note that the distance from shower axis is denoted as R from chapter 4. In this section, $\mathbf{R}$ represents the core position of air showers on the ground.

$$(R_{\rm COG})_{\rm y} = \frac{\sum_{i=1}^{N} \rho_i y_i}{\sum_{i=1}^{N} \rho_i} \quad , \tag{2.8}$$

$\sigma_{\mathbf{R}_{\rm COG}} = 170$ m used for the analysis. The left panel of figure 2.15 shows the sample event time fit.

After the trigger time fit, the lateral distribution fit is performed by applying the following function to the integrated FADC values obtained in each event.

$$\rho^{\rm FIT} = A \left(\frac{s}{91.6{\rm m}}\right)^{-1.2} \left(1.0 + \frac{s}{91.6{\rm m}}\right)^{-(\eta(\theta)-1.2)} \left[1.0 + \left(\frac{s}{1000{\rm m}}\right)^2\right]^{-0.6} \quad , \tag{2.9}$$

$$\eta(\theta) = 3.97 - 1.79[\sec\theta - 1] \quad , \tag{2.10}$$

where A is the fitting parameter. This function is the same as the AGASA experiment described in chapter 1. The uncertainty σ_ρ is adjusted to fit the TA SD data:

$$\sigma_\rho = \sqrt{0.56\rho + 6.3 \times 10^{-3}\rho^2} \quad . \tag{2.11}$$

Then the scale A of the lateral distribution and the core position $\mathbf{R}$ are determined by minimizing the function,

$$\chi^2_{\rm LDF} = \sum_{i=0}^{N} \frac{(\rho_i - \rho_i^{\rm FIT})^2}{\sigma^2_{\rho_i}} + \frac{(\mathbf{R} - \mathbf{R}_{\rm COG})^2}{\sigma^2_{\mathbf{R}_{\rm COG}}} \quad . \tag{2.12}$$

The right panel of figure 2.15 shows a typical TA SD lateral distribution fit.

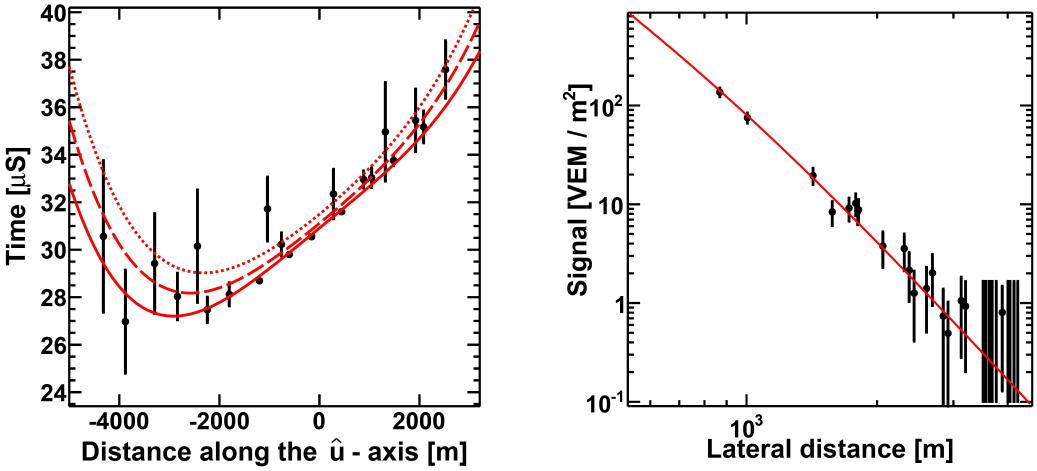

Figure 2.15: The TA SD geometry and lateral fit figures for the same event as figure 2.13 [86]. (left) The distribution of the SD trigger time versus the distance along $\hat{\mathbf{u}}$ axis, which is the shower axis projected onto the ground. Solid curve is the time expected by the fit for detectors lying on the $\hat{\mathbf{u}}$ axis. The dashed and dotted lines are the expected times by the fit for the detectors that are 1.5 and 2.0 km off the $\hat{\mathbf{u}}$ axis. (right) The lateral distribution fit. The horizontal and vertical axes represent the distance from shower axis and the integrated FADC values ρ in VEM/m^2 unit.

After the time and lateral distribution fit, the primary cosmic ray energy is calculated from the integrated FADC values at 800 m from shower axis, called $S800 \equiv \rho^{\mathrm{FIT}}(800$ m), and $\sec\theta$. The conversion relation from these two parameters to the energy E is studied by the MC described in the next chapter and recorded as a table, as shown in the left panel of figure 2.16. For each event, this conversion table is referred for the first estimation of the energy E.

2.3.3 Energy measurement for hybrid events

The reconstructed TA SD energy E'_{SD} (equals E described above) is determined using the MC, hence it has the large uncertainty from hadronic models in the air shower simulation. The TA FD energy E_{FD} is determined using calorimetric detection of air shower energy deposit in the atmosphere, hence it has less uncertainty than E'_{SD}. To obtain precise energy, it is necessary to correct the energy scale of E'_{SD} to match the TA FD using hybrid events. In this section we will introduce the reconstruction method of E_{FD}, referring that of BR and LR FD stations [66, 68].

Figure 2.17 shows the sample event display of a hybrid event. The key feature of the hybrid analysis is to use both the SD and FD timing information for the event reconstruction. By using the SD timing at which the shower plane crosses the ground as an anchor for the conventional FD timing fit, the accuracy of the shower geometry

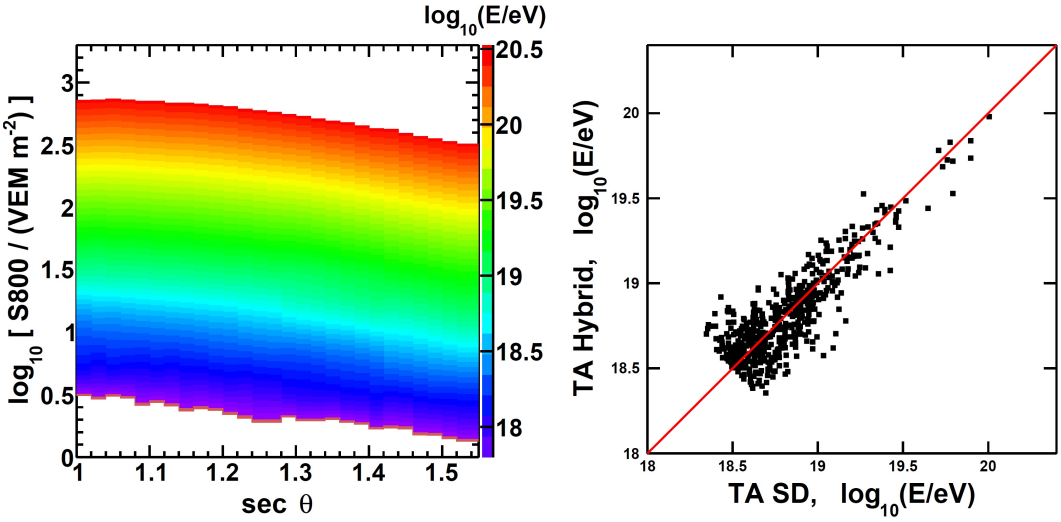

Figure 2.16: (left) The conversion table from $S800$ and $\sec\theta$ to the primary cosmic ray energy, which is made from the MC [86]. Colors represent the reconstructed energy $E'_{\rm SD}$. (right) The correlation between the SD energy normalized by 1/1.27 ($E_{\rm SD}$) and the FD energy ($E_{\rm FD}$) on the hybrid events [86]. The horizontal and vertical axes represent $E_{\rm SD}$ and $E_{\rm FD}$, respectively. The solid line represents $E_{\rm FD} = E'_{SD}$ relation.

determination is improved compared to the FD monocular analysis. At first, the Shower Detector Plane (SDP) is defined as the bundle of the pointing direction vectors of the triggered PMTs. Figure 2.18 shows the geometry definition on the SDP. Then the shower geometry (the direction and arrival position on the ground) is determined from the pointing directions and timings at the FD PMTs:

$$T_{{\rm exp},i} = T_{\rm core} + \frac{\sin\psi - \sin\alpha_i}{c\sin(\psi+\alpha_i)} R_{\rm core} \tag{2.13}$$

where $T_{{\rm exp},i}$ and α_i are the expected timing and elevation angle in the SDP for the i-th PMT, respectively. $T_{\rm core}$ is the time when the air shower reached the ground, $R_{\rm core}$ is the distance from the FD station to the core, and ψ is the elevation angle of the air shower in the SDP. For an event that has timing information of one SD near the core, $T_{\rm core}$ is expressed by:

$$T_{\rm core} = T'_{\rm SD} + \frac{1}{c}(R_{\rm core} - R_{\rm SD})\cos\psi \tag{2.14}$$

$$T'_{\rm SD} = T_{\rm SD} - \frac{1}{c}((\mathbf{P}'_{\rm SD} - \mathbf{P}_{\rm SD})\cdot\mathbf{P}) \tag{2.15}$$

where $\mathbf{P}_{\rm SD}$ is the position of the SD, $\mathbf{P}'_{\rm SD}$ is the projection of $\mathbf{P}_{\rm SD}$ onto the SDP, $\mathbf{P}$ is the direction of the shower axis, $T_{\rm SD}$ is the timing of the leading edge of the SD signal. To reconstruct the shower longitudinal profile, an "inverse MC method" in shower reconstruction is employed to find an MC shower which best reproduces the data considering

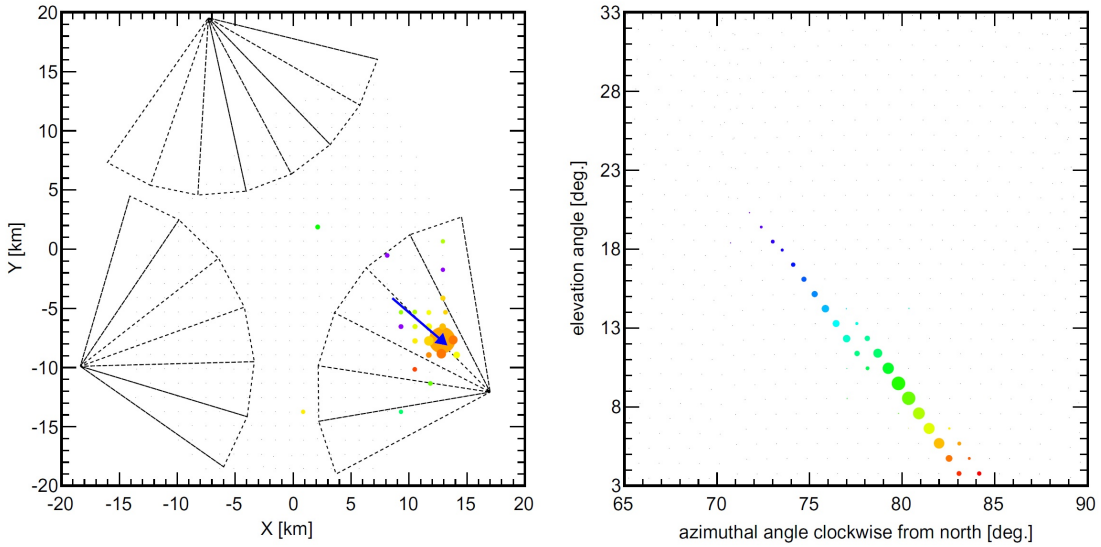

Figure 2.17: An example event display for a hybrid event [68]. (left) The map of SDs which were hit by the shower. The colors of the filled circles reflect the shower arrival time and the size of the circle is proportional to the number of photo-electrons recorded by the SD. The black dotted lines indicate the field of view for the telescopes at each FD. The horizontal and vertical axes indicate the locations of the TA detectors. The blue arrow represents the reconstructed shower axis. (right) The signals in the LR telescopes. The horizontal and vertical axes represent the pointing direction of each PMT. The filled circles are the selected PMTs. The color indicates timing and the size of the circle indicates the number of detected photo-electrons.

photons from air showers and detector response. The longitudinal development of air showers, which is the number of charged particles $N(X)$ at an atmospheric depth X, is described by the G-H function explained in section 1.3.4.

$$N(X) = N_{\max} \left(\frac{X - X_0}{X_{\max} - X_0} \right)^{\frac{X_{\max} - X_0}{\lambda}} \exp\left(\frac{X_{\max} - X}{\lambda} \right) \tag{2.16}$$

Here X_0 is fixed to 0 and λ is fixed to 70 g/cm^2. The $X_{\max}$ value is determined so that the sum of signals in each PMT of the MC reproduces that of the data. A calorimetric energy E_{FD} is calculated by integrating the obtained G-H function. In the calculation, a fluorescence yield model [69], which describes the number of photons emitted by air molecules per energy losses of air shower charged particles, with the the fluorescence photon spectrum measured by the FLASH experiment [70] is used. The systematic error of the energy determination is 21% [68], which is composed of uncertainties in the fluorescence yield (11%), atmospheric attenuation (11%) [71], the absolute detector calibration (10%) [72, 73, 74] and reconstruction (10%). The detail analysis procedure of BR FD and LR FD is described in [68] and that of MD FD is described in [64].

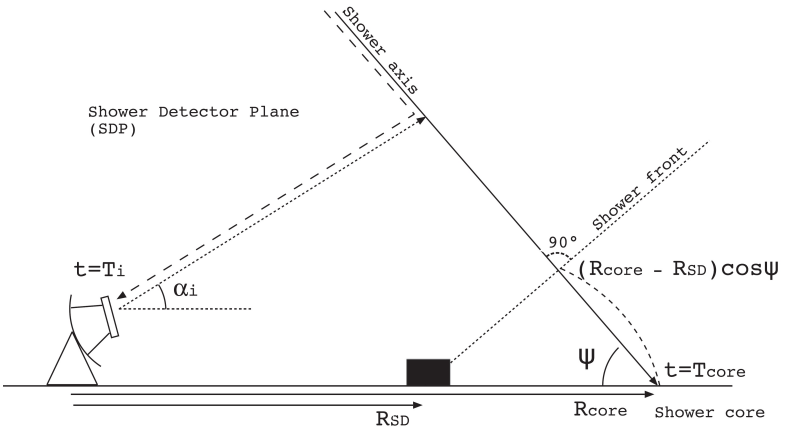

Figure 2.18: The diagram of the geometry used for the hybrid reconstruction [68].

2.3.4 TA SD energy determination and event selection

We compared the reconstructed energy $E'_{\rm SD}$ with $E_{\rm FD}$ and found good lineality relation between $E'_{\rm SD}$ and $E_{\rm FD}$, but $E'_{\rm SD}$ was larger than $E_{\rm FD}$ by 27%. To reduce the model dependence of the TA SD energy scale, the reconstructed SD energy $E'_{\rm SD}$ is normalized by 1/1.27, described as $E_{\rm SD} \equiv E'_{\rm SD}/1.27$, to match the TA FD energy for hybrid events. The right panel of figure 2.16 shows the correlation between $E_{\rm SD}$ and $E_{\rm FD}$ on the hybrid events.

After the energy is determined, the event selection process is conducted to reduce poorly-reconstructed events. The selection criteria are as follows [12]:

1. the number of SD in each event is larger than 5.
2. $\theta < 45^\circ$.
3. The distance of reconstructed event core from the edge of the array is larger than 1200 m.
4. $\chi^2_{\rm G}$/d.o.f. < 4, $\chi^2_{\rm LDF}$/d.o.f. < 4. Here d.o.f. means the number of degrees of freedom.
5. The angular uncertainty estimated by the timing fit is less than 5°.
6. The fractional uncertainty $\sigma_{\rm S800}/S(800)$ estimated by the lateral distribution fit is less than 25%.

The TA SD reconstruction resolution is determined by the MC simulation (described in chapter 3). The simulation uses the same reconstruction program and quality cut condition as the data. The energy resolution is 36% for $10^{18.0}{\rm eV} < E_{\rm in} < 10^{18.5}{\rm eV}$, 29% for $10^{18.5}{\rm eV} < E_{\rm in} < 10^{19.0}{\rm eV}$ and 19% for $E_{\rm in} > 10^{19.0}{\rm eV}$, respectively [80]. Here $E_{\rm in}$ is the input primary particle energy. The angular resolution is 2.4° for $10^{18.0}{\rm eV} < E_{\rm in} <$

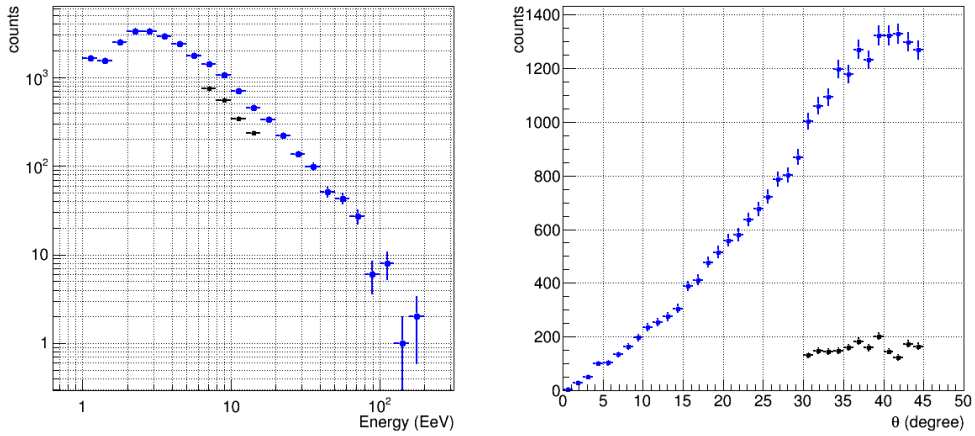

Figure 2.19: The distributions of reconstructed parameters. The blue and black show all the detected event condition ($E_{\rm rec} > 10^{18}$eV$, \theta < 45°$) and the the muon analysis condition ($10^{18.8}$eV $< E_{\rm rec} < 10^{19.2}eV, 30° < \theta < 45°$). (Left) Energy distribution. (Right) Zenith angle distribution.

$10^{18.5}$eV, 2.1° for $10^{18.5}$eV $< E_{\rm in} < 10^{19.0}$eV and 1.4° for $E_{\rm in} > 10^{19.0}$eV, respectively [80].

The above reconstruction procedure is applied to the TA SD 7 years' dataset from 11 May 2008 to 11 May 2015. Figures 2.19 - 2.21 show the typical reconstructed parameters of the data. All the detected event condition ($E_{\rm rec} > 10^{18}$eV$, \theta < 45°$) and the the muon analysis condition ($10^{18.8}$eV $< E_{\rm rec} < 10^{19.2}eV, 30° < \theta < 45°$) are described.

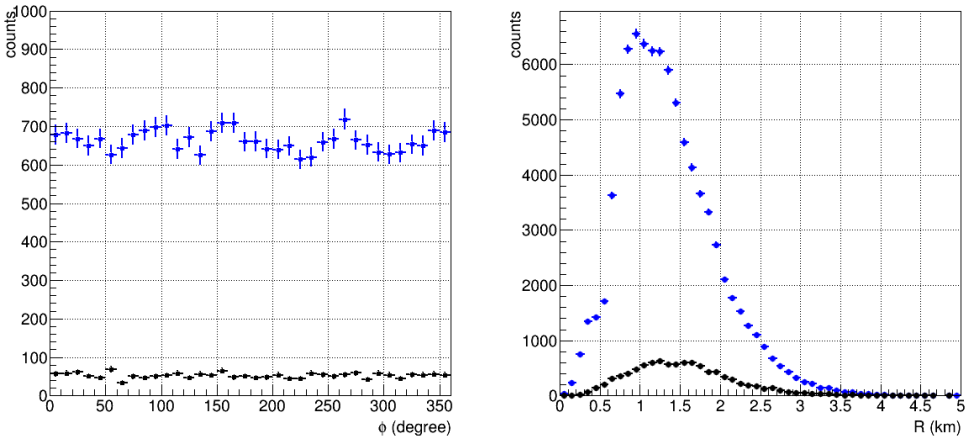

Figure 2.20: Same as figure 2.19, but for different parameters. (Left) Distribution of air shower azimuth angle. (Right) Distribution of distance from shower axis to the detectors which pass signal selection scheme explained in section 2.3.1.

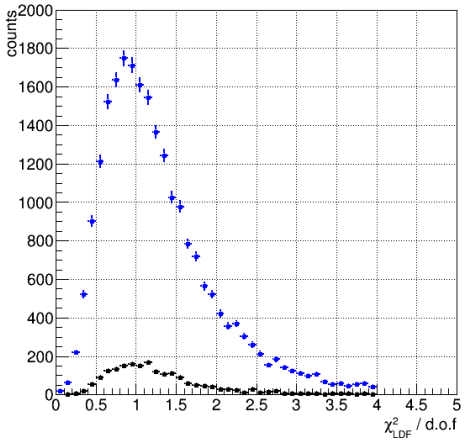

Figure 2.21: Same as figure 2.19, but for χ^2_{LDF}/d.o.f. value of lateral distribution fitting.

3 Monte Carlo Simulation

The TA SD Monte Carlo simulation is generated to reproduce the data by using CORSIKA [75] air shower simulation and Geant4 [76] detector simulation. The thinning method is used for air shower simulation to reduce the calculation time and the dethinning method is applied to thinned showers to obtain the information lost in thinning. In this chapter, the methods of TA SD air shower simulation and detector simulation are described.

3.1 Air shower simulation

The simulation of UHECR air shower is generated by CORSIKA v6.960 [75]. We use QGSJET II-03 [39] as a reference model for high energy hadronic interactions. There are other hadronic models often used in $E > 10^{18}$ eV such as Epos 1.99 [88] or Sibyll 2.1 [89], which have different interaction parameters (inelastic cross section, multiplicity and so forth). Also, there is QGSJET II-04 [40] model which is the updated version of QGSJET II-03 made using the results of the LHC experiment. The MC for these models are generated using the MC procedure established in QGSJET II-03 [39] model, which is described below. We also use FLUKA2008.3c [81, 82] to model low energy hadronic interactions and EGS4 [83] to model electromagnetic interactions.

The air shower MC with tracking all secondary particles, where 10^{11} particles are generated at shower maximum for a 10^{20} eV event, requires too large calculation time. For a single CPU core, one shower simulation for $E \sim 10^{20}$ eV takes part of a decade [79]. The approximation technique called thinning [77] is used, in which particles are removed from consideration in the shower generation and other particles in similar regions of phase space are given weights to account for the loss.

But the thinning method does not fully reproduce the TA SD signal. The TA SD measures the lateral distribution of air shower particles at the ground. The measured particles include those far from the shower axis ($\sim$km), where the average number of particles at a TA SD in a shower event is less than unity. The thinning approximation causes larger artificial fluctuation of the number of particles than non-thinned air showers [78].

Note that the thinning method is valid for the FD simulation because the longitudinal profile of the air shower measured by the FD is generated mainly in the shower core. The shower core is a dense and narrow region around the shower axis that contains most of secondary particles generated in air showers with small fluctuations in the numbers.

Hence the uncertainty due to the fluctuation of the number of particles in the FD energy determination is relatively small.

To make more accurate simulation of the TA SD, dethinning method is developed, where each group of thinned particles was regenerated from its weighted representative [78, 79]. The idea of replacing the information lost in thinning is to start with a thinned shower, maintain the average density of particles, and smooth the distribution to get the correct amount of fluctuations. A brief description of CORSIKA thinning and dethinning for TA SD MC is as follows [78, 80]. Let E_0 and ϵ denote the primary cosmic ray energy and thinning level parameter. The simulation is generated for a given ϵ value, which is 10^{-6} for TA SD MC. For each step of the interaction of each shower particle, two situations are possible; $\Sigma_j E_j < \epsilon E_0$ and $\Sigma_j E_j > \epsilon E_0$ where j describes the secondary particles generated in the interaction and E_j is the energy of each particle. If $\Sigma_j E_j < \epsilon E_0$, one secondary particle survives with probability $p_i = E_i/\Sigma_j E_j$. If $\Sigma_j E_j > \epsilon E_0$, one of the secondary particles of energies $E_i < \epsilon E_0$ survives in the secondary particles with probability $p_i = E_i/\epsilon E_0$ and all particles with $E_i > \epsilon E_0$ are kept. In both cases, surviving particles have the weight of $w_i = 1/p_i$. Thus the weight of a particle reaching the end of the simulation after passing through numbers of interaction steps is $w_{i,tot} = \Pi_k 1/p_k$ where k describes each step. This algorithm conserves the total energy; the weighted sum is equal to the energy of the primary particle that initiated the shower.

In the dethinning method, $w - 1$ particles are inserted to every ground particle of weight w generated by the simulation with thinning. When this is completed the weight of each particle is set to 1. To insert these particles we use the following procedure [78].

1. Choose an arbitrary vertex point on the trajectory of the weighted particle.

2. Choose a point in a cone centered on the particle's trajectory, weighted by a two-dimensional Gaussian distribution with a sigma of a few degrees. This will be the inserted particle's trajectory.

3. Project the inserted particle to ground level, assign it a time and energy, and add it to the particle list of the dethinned shower.

4. Perform steps 2 and 3 for $w - 1$ times.

Figure 3.1 shows the geometry used in the above procedure.

The distributions of the energy of particles, rise time and number of particles were compared between dethinned and non-thinned showers. The comparison was done for different conditions of cosmic ray energy E, zenith angle θ, azimuth angle Φ relative to the shower axis, distance R from the shower axis and secondary particle types. That shows the dethinned shower agrees well with the non-thinned shower. Figure 3.2 shows a comparison of the histograms of the number of muons among non-thinned, thinned and dethinned showers.

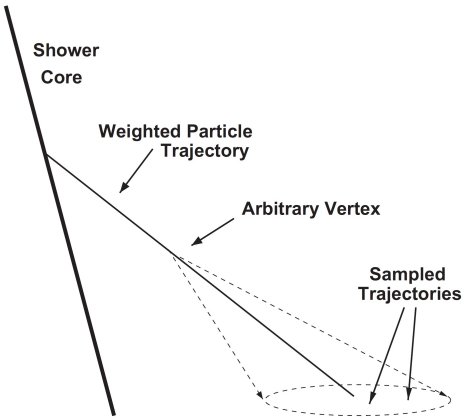

Figure 3.1: The geometry of the dethinning method [78]. The thick and thin solid lines show the primary and secondary particle tracks, respectively. The secondary particle has the weight of w. The dashed line represents a cone referred in the step 2 in the text.

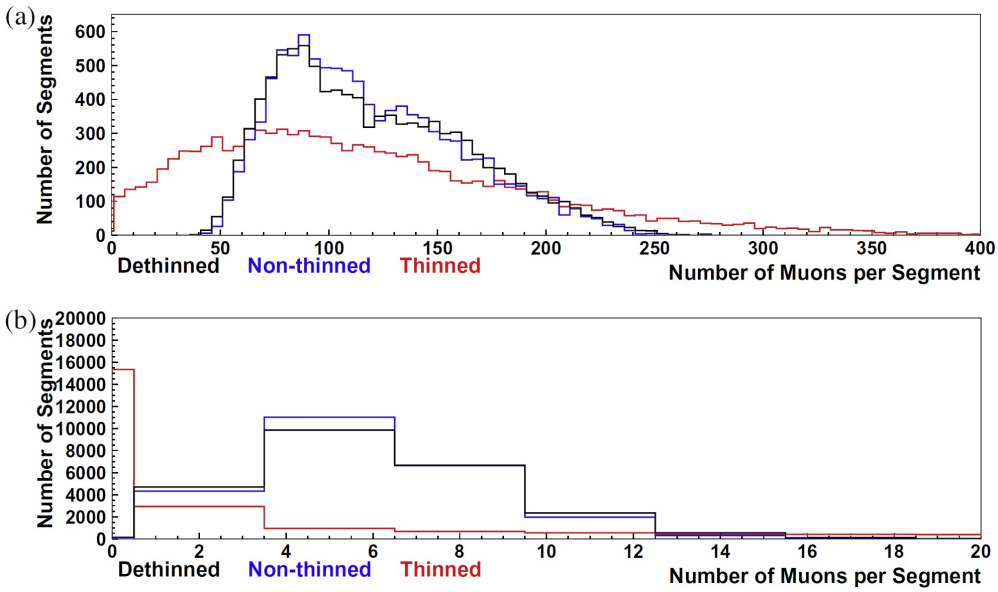

Figure 3.2: Histograms of the number of muons in 6 m $\times$ 6 m segments in plane normal to shower trajectory [78]. The primary energy, zenith angle and composition are $E = 10^{19}$ eV, $\theta = 45^\circ$ and proton, respectively. The black, red and blue are non-thinned, thinned and dethinned showers, respectively. (a) $\Phi = [-30^\circ, 30^\circ]$ and R =[500 m, 1000 m]. (b) $\Phi = [-150^\circ, 210^\circ]$ and R =[1500 m, 2000 m].

3.2 Detector simulation

The TA SD detector simulation using Geant4 includes a detailed modeling of the TA SD geometry and materials. The simulation provides energy deposit in scintillator layers for a given particle type, momentum and trajectory. In order to generate the accurate air shower and detector MC in a short time, we prepared the library of the SD response to suitably parameterized particle injection. Figure 3.3 shows the particle beam and detector arrangement to make the library. The simulation procedure is as follows. Firstly, a random point (X, Y) on the ground in 6 m $\times$ 6 m square and an injection azimuth angle ϕ are sampled. Secondly, a particle is generated in a given θ and sampled ϕ direction so that it directs to (X, Y) on the ground. Then repeat the above procedure for 1.2×10^6 times in each particle type ($\gamma, e^{\pm}, \mu^{\pm}, p, n, \pi^{\pm}$), energy ($\log_{10}(E/eV) = 4.7, 4.8, ..., 11.0$ for γ, $\log_{10}(E/eV) = 6.0, 6.1, ..., 10.9$ for $\pi^{\pm}$ and $\log_{10}(E/eV) = 6.0, 6.1, ..., 11.0$ for $e^{\pm}, \mu^{\pm}, p, n$) and zenith angle ($\sec\theta = 1.0, 1.5, 2.0, ..., 4.0$). For each condition, two dimensional histograms of energy deposition in upper and lower layers are generated, and recorded as the response library.

When air shower events are simulated by CORSIKA, the output file which consists of $(X, Y, Z, p_{\mathrm{x}}, p_{\mathrm{y}}, p_{\mathrm{z}}, t)$ of each particle on the ground is recorded. Here p_{n} means the momentum in the n direction and t means the time when reaching the ground. The momentum is converted to the energy deposition in a TA SD, using the closest value of the library table described above. Then the ground and the time is binned in 6m $\times$ 6m $\times$ 20ns. The time, position and energy deposition are recorded in each bin. Following that, the air shower event core position in the TA SD array configuration is randomly determined and the event time is randomly assigned from the observed event dataset. If the air shower particle position overlaps the SD position, the particle is counted as the detector signal. The background signals are also calculated by simulating atmospheric muons as primary particles. The signal is smeared following the measured electronics response shape and converted to FADC count using the detector calibration information in the event time. Finally, the detectors pass trigger process by the same method as the data.

3.3 Calculation condition and event reconstruction for MC

The proton composition showers with the primary energies between $10^{16.55}$ eV and $10^{20.55}$ eV are generated. The zenith angle is isotropically distributed in [0°, 60°]. The azimuth angle and core position are randomly distributed.

To reduce the calculation time, the oversampling of events is done. The original input energy of the MC event is set discretely ($10^{16.6}$ eV, $10^{16.7}$ eV, ..., $10^{20.5}$ eV), and the energy is randomly distributed artificially in each energy bin where the bin width is 0.1 in $\log E$. The zenith angle is smeared, setting the average value as the original value. Then one simulated shower event is sampled by more than tens of times, performing the above scheme each time.

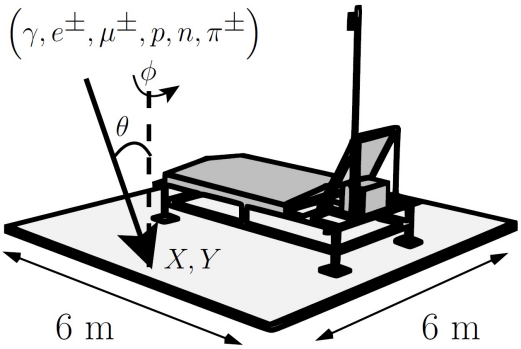

Figure 3.3: Arrangement of the detector simulation [80].

Table 3.1: Cosmic ray parameters generated in the TA SD MC.

Parameter	Method of sampling
Composition	Proton
Energy, E	Hires broken power law function [84] $E^{-3.25}$, $E < 10^{18.65}$ eV $E^{-2.81}$, $10^{18.65}$ eV $\leq E < 10^{19.75}$ eV $E^{-5.1}$, $E \geq 10^{19.75}$ eV
Zenith angle, θ	$\sin\theta\cos\theta$ distribution in $[0°, 60°]$
Azimuth angle, ϕ	Flat distribution in $[0°, 360°]$
Impact position	Randomly distributed inside a circle of 25 km radius centered at the TA CLF

The same reconstruction procedure is applied for the MC dataset. The oversampled events are sampled again so that the energy distribution follows the spectrum measured by the HiRes experiment [84]. The parameters of generated events of the TA SD MC are summarized in table 3.1.

Figures 3.4 - 3.8 show the comparison of typical reconstructed parameters of the data to that of the MC. These are in agreement between the data and the MC. Note that the above comparison is done in the same energy scale, in which the FD energy scale (corresponding to E_{SD}) is used. In the next chapter, the number of particles from air showers of the data is compared with that of the MC, using different energy scale. This condition will be explained in section 4.1.

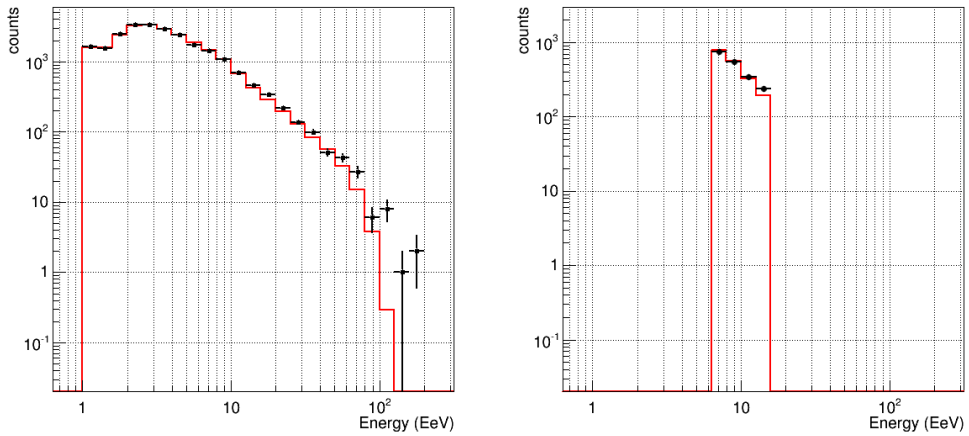

Figure 3.4: The comparison of reconstructed parameters of the SD data to that of the MC for energy distribution. The black and red represent data and MC, respectively. The data from 11 May 2008 to 11 May 2015 are used. The area of the histogram of MC is normalized to that of the data. (Left) All the detected event condition ($E_{\rm SD} > 10^{18}{\rm eV}, \theta < 45^{\circ}$). (Right) The muon analysis condition which will be presented in chapter 4 ($10^{18.8}{\rm eV} < E_{\rm SD} < 10^{19.2}{\rm eV}, 30^{\circ} < \theta < 45^{\circ}$).

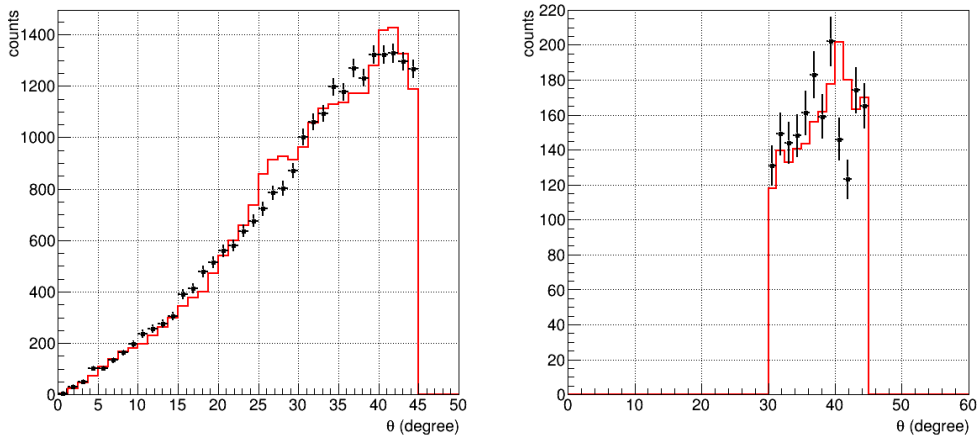

Figure 3.5: Same as figure 3.4, but for the zenith angle distribution.

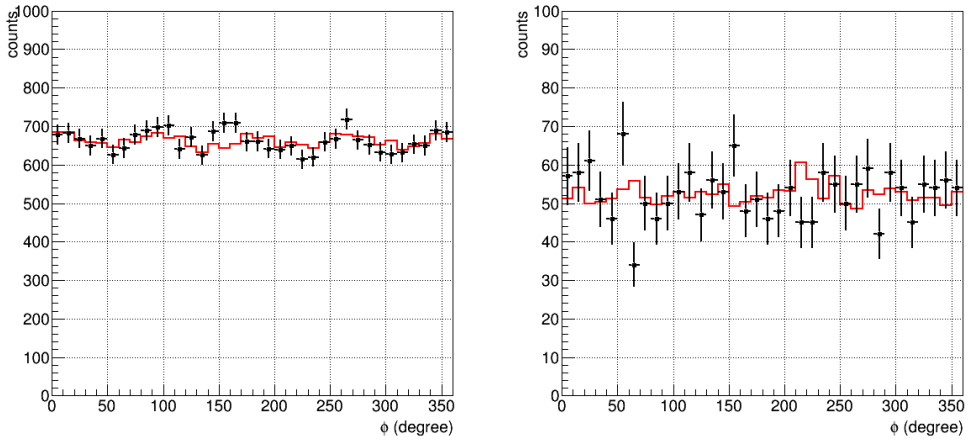

Figure 3.6: Same as figure 3.4, but for the air shower azimuth angle.

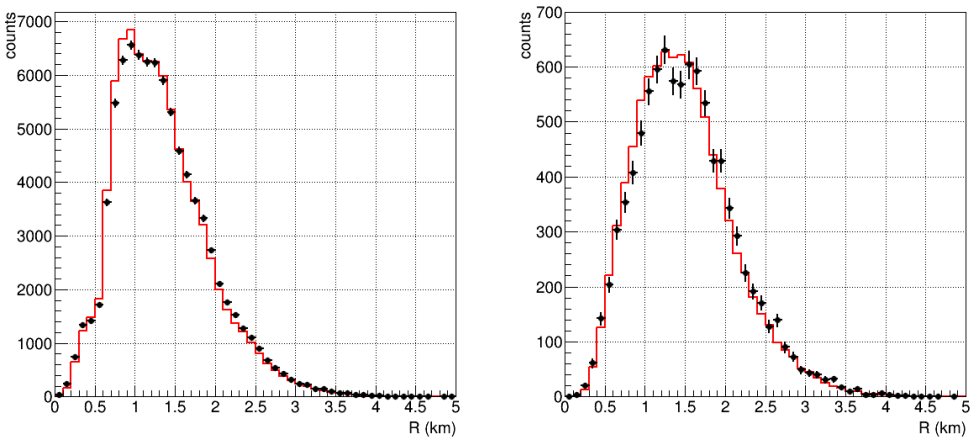

Figure 3.7: Same as figure 3.4, but for the distance from shower axis to the detectors which pass signal selection scheme explained in section 2.3.1.

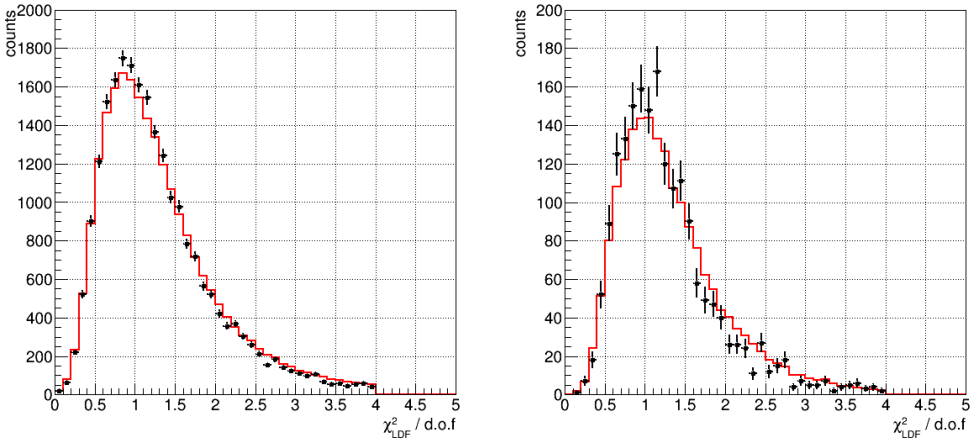

Figure 3.8: Same as figure 3.4, but for χ^2_{LDF}/d.o.f. value of lateral distribution fitting.

4 Muon analysis

4.1 Dataset

We use the TA SD 7 years' dataset recorded from 11 May 2008 to 11 May 2015. In this analysis, we use the reconstructed energy range $10^{18.8}$ eV $< E < 10^{19.2}$ eV and the dataset of events with quality cut used for the TA spectrum analysis [12]. This energy range is followed the analysis of the Auger experiment [87]. The composition of the primary cosmic ray estimated by the TA FD observation is consistent with proton [31, 32, 33]. We use the FD energy scale (the energy scale where the normalization by 27% ($E_{\rm SD} = E'_{\rm SD}/1.27$) is applied; $10^{18.8}$ eV $< E_{\rm SD} < 10^{19.2}$ eV) for the experimental data since the TA FD has done the calorimetric measurement of the shower particle energy deposition and its uncertainty of the absolute energy determination is less than the TA SD, as described in section 2.3. The number of air shower events is ~ 3600 in the dataset on condition $10^{18.8}$ eV $< E < 10^{19.2}$ eV and $\theta < 45^{\circ}$. Figure 4.1 shows waveforms of a typical event observed by the TA SD. The horizontal and vertical axes in this figure represent the time and the FADC value plus $1000\times\log_{10}(1 + R/\mathrm{km})$, respectively. The origin of the horizontal axis is the first trigger time of the Level-0 trigger detectors within ± 32 μsec from an event trigger time. The vertical offset of each waveform is proportional to $\log_{10}(1 + R/\mathrm{km})$, that the offset values are $\simeq 300$ at $R = 1000$ m and $\simeq 700$ at $R = 4000$ m, respectively. According to the air shower geometry, the FADC value is small at the earlier age of the air shower (on the upper left side of the figure), becomes large when the air shower core reaches the ground (in the lower middle of the figure) and again becomes small at the older age of the air shower (on the upper right side of the figure).

The detail of the MC dataset is described in chapter 3. The reconstructed energy range $10^{18.8}$ eV $< E < 10^{19.2}$ eV and the same quality cut condition as the data are used. We use original MC energy scale, where the normalization by 27% is not applied ($10^{18.8}$ eV $< E'_{\rm SD} < 10^{19.2}$ eV). Firstly, the experimental data is compared with the MC using the hadronic model QGSJET II-03 for proton. After that the other models and mass composition are tried; Epos 1.99 [88], Sibyll 2.1 [89] and QGSJET II-04 for proton, and QGSJET II-03 for iron. The generated number of events is ~ 60000 events on condition $10^{18.8}$ eV $< E < 10^{19.2}$ eV and $\theta < 45^{\circ}$.

The TA SD MC used for the spectrum and the arrival direction analyses does not record secondary particle type information for the outputs to reduce data sizes. To study muons in the air shower signals, I revised the MC codes to separate the outputs for six

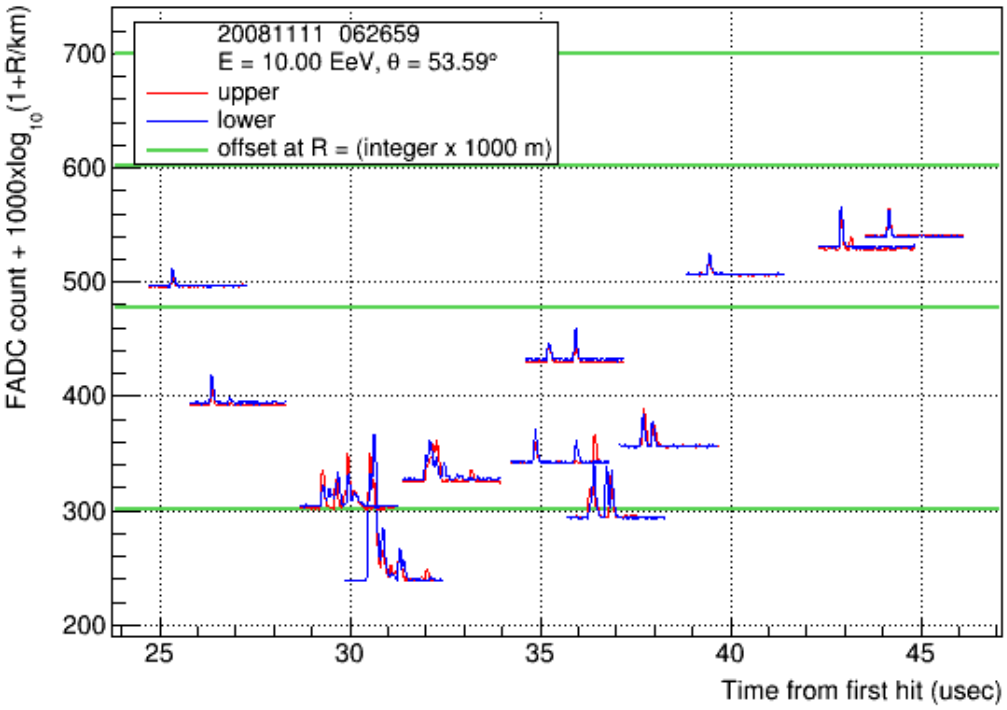

Figure 4.1: Observed signal waveforms in a typical air shower event in 11 Nov. 2008 6:26:59 UTC. The red and blue histograms represent waveforms of the upper and lower scintillators, respectively, in each SD. The green lines correspond to the values of the vertical offset $1000 \times \log_{10}(1 + R/\mathrm{km})$ at $R = 1000$ m, 2000 m, 3000 m and 4000 m from the bottom to top.

components corresponding to particle types; i) gamma, ii) electron/positron (hereafter, electron/positron is described as electron), iii) μ^-/μ^+ (hereafter, μ^-/μ^+ is described as muon), iv) other shower components (hadron such as pion or neutron), v) background (atmospheric muon and pedestal) and vi) the total of above components. For each component, TA SD waveforms relevant to air showers are recorded by using this revised MC. The air showers are reconstructed by applying the procedure explained in section 3 to the total signal, and the corresponding waveform of each component is picked up. Figure 4.2 shows the sample waveforms for all six types. Note that only the total component is obtained for the ordinary data taking condition.

The revised TA SD MC input and analysis conditions are shown in table 4.1. The selection criterion of the analysis energy range is explained in the next section. The energy resolutions of the TA SD are 29% for $10^{18.5}$ eV $< E < 10^{19.0}$ eV and 19% for $10^{19.0}$ eV $< E < 10^{19.5}$ eV [80]. Hence the input energy range is set to be wider $(1 - 0.29) \times 10^{18.8}$ eV $< E < (1 + 0.19) \times 10^{19.2}$ eV than that of the analysis energy range.

Table 4.1: The MC input and analysis conditions

	E (eV)	θ (°)	comment
input	$10^{18.55} - 10^{20.15}$	[0, 60]	
analysis	$10^{18.8} - 10^{19.2}$	[0, 45]	quality cut for spectrum

4.2 Analysis framework

The secondary particles generated in the atmosphere are attenuated by the interaction with atmospheric particles and the decay before they reach the ground. The electromagnetic (EM) components (electron and gamma) are more attenuated than muons compared in the same pass length, because the EM components largely lost their energy by the pair production and bremsstrahlung in the shower propagation but muons can penetrate the atmosphere down to the ground before they decay. Hence the ratio of the number of air shower muons detected by the SDs to the number of all charged particles detected by the same SDs (hereafter this ratio is described as the muon purity) is expected to be larger as the SDs are more distant from secondary particle generation points on the shower axis.

On the ordinary analysis condition, the TA SD signals are dominated by the EM components. To increase the muon purity in the signal, we divide the observed air shower events into two bins in zenith angle, [0°, 30°] and [30°, 45°]. The zenith angle distribution in the analysis energy range ($10^{18.8} - 10^{19.2}$ eV) is expected to follow $\mathrm{d}n/\mathrm{d}\theta = \sin\theta\cos\theta$. It is because the cosmic rays are expected to arrive at the Earth isotropically and solid angle in $\mathrm{d}\theta$ band is proportional to $\sin\theta$, while the detection area of the SD

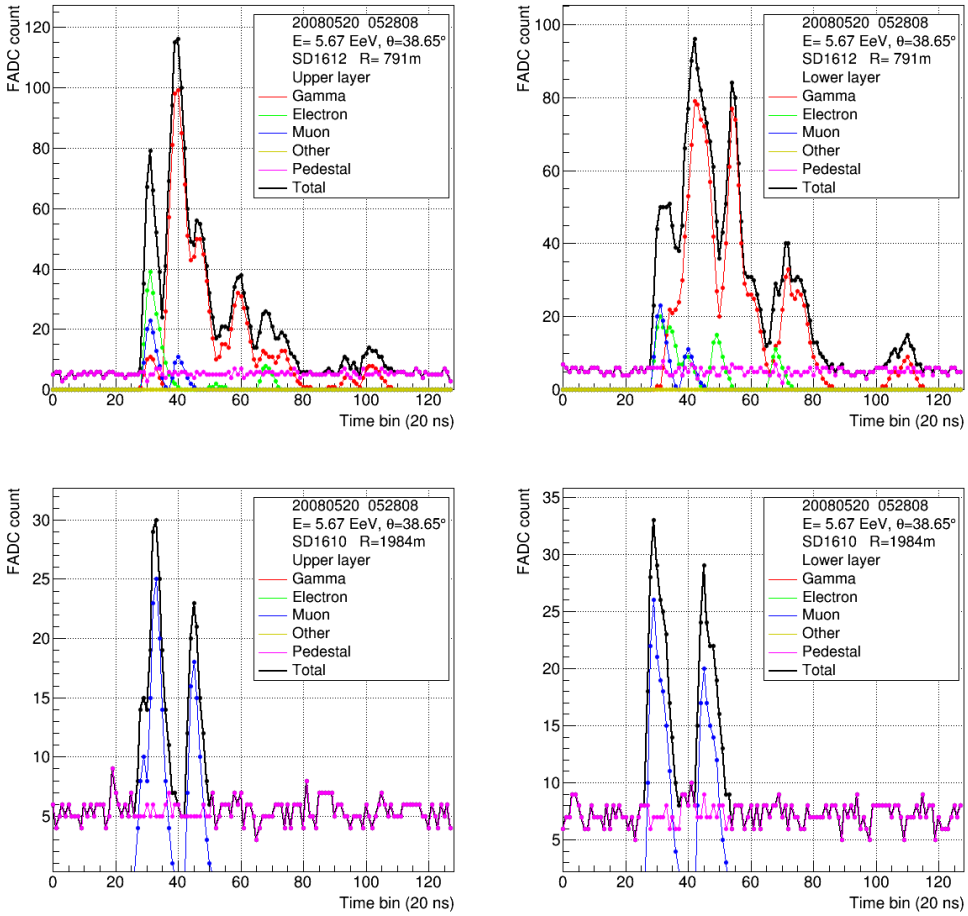

Figure 4.2: Sample event waveforms generated by the revised TA SD MC. The red, green, blue, yellow, magenta and black represent gamma, electron, muon, other shower components, background and total of them, respectively. (top left) The waveforms of the SD upper scintillator at $R \simeq 800$ m. Here R is the distance from shower axis. (top right) Same as top left, but for lower scintillator. (bottom left) The waveforms of the SD upper scintillator at $R \simeq 2000$ m. (bottom right) Same as bottom left, but for lower scintillator.

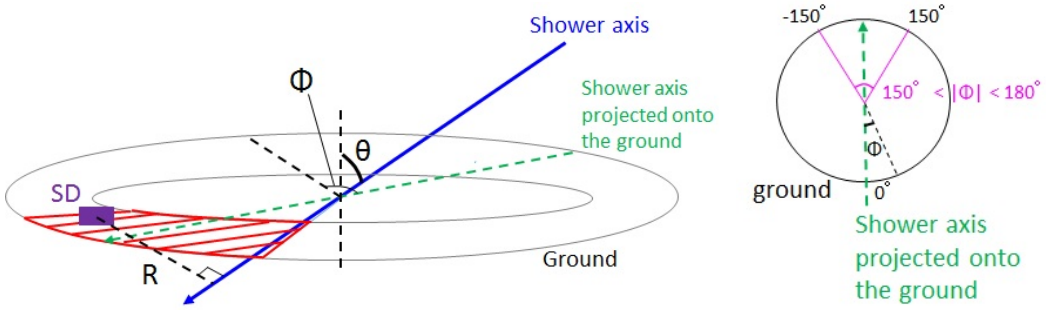

Figure 4.3: (left) Geometry definition of the muon analysis. The ground is separated by azimuth angle relative to the shower axis projected onto the ground, ϕ, and the distance from shower axis, R. The muon purity in the SD signal is calculated in each (ϕ, R) bin. The red region in the figure shows the largest distance bin from the particle generation points on the shower axis, which is expected to be the least EM background bin. (right) Top view for ϕ definition. There are six bins for the analysis and the geometry for $150° < |\phi| < 180°$ is shown by magenta lines.

is proportional to $\cos\theta$. Hence the two zenith angle conditions are expected to have the same number of events. We also divide the ground by ϕ, the azimuth angle relative to the shower arrival direction projected onto the ground, and R, the distance from shower axis. The geometry definition is described in the figure 4.3. Six bins are set for ϕ ($|\phi| < 30°, 30° < |\phi| < 60°, 60° < |\phi| < 90°, 90° < |\phi| < 120°, 120° < |\phi| < 150°$ and $150° < |\phi| < 180°$). The numbers of detectors which have air shower signals are nearly the same in each bin since it is proportional to the surface area for the data sampling. The distance from the shower axis is equally divided into 18 bins within 500 m $< R <$ 4500 m in logarithmic scale. The maximum R is limited by an air shower generation method (dethinning method) [78]. Note that any (ϕ, R) cuts were not adopted in the previous SD spectrum analysis [12].

If taking larger $\theta, |\phi|$, or R values, the atmospheric thickness between SDs and particle generation points on the shower axis increases, then the muon purity in the signal of SDs is expected to be relatively high. We compare the signal size, which is the energy deposit of air shower signals in the SD, between the experimental data and the MC in each $(\theta, |\phi|, R)$ condition. Also, muon-enriched condition is searched by comparing air shower components using the MC. To study muons from air showers, we take the following strategy to investigate the muon component in the air shower.

- On muon-enriched condition, the signal size of the data is compared with that of the MC for proton using QGSJET Ⅱ-03 model.
- The above comparison is studied with the different hadronic models and mass compositions.
- Confirm the correlation between the muon purity in the signal and the ratio of the

integrated FADC value between the data and the MC.

The signal size is calculated as follows. In each detector waveform, the bins which exceed the the pedestal by 5 σ are selected and summed [80]. The average pedestal is subtracted from the summed value. Then the value is converted from the unit of FADC count to that of MeV using the calibration information in each detector. Following that, the value in MeV unit is converted to VEM unit, which is defined in section 2.2.3. We call the value as the signal size and denote as S in the following figures. In other words, $S = f(C_{\rm FADC} - C_{\rm Ped})$, where f is conversion factor from FADC count to VEM unit, $C_{\rm FADC}$ is total FADC count, $C_{\rm Ped}$ is pedestal count.

The analysis procedure is as follows:

1. Air shower events which pass quality cut described in section 2.3 are selected.
2. For each air shower event, SDs which have air shower signals are picked up.
3. The signal size in a SD is calculated.
4. The procedures 2 - 3 are repeated for each event.
5. Finally, the histograms of the signal size (S) are made for each (θ, ϕ, R) condition using all the selected air showers. The histograms include the no hit detectors as $S = 0$.

Figures 4.4 and 4.5 show the histograms of the signal size measured by the TA SD, compared with the MC. The area of the MC histogram is normalized to that of the data. If a vertical muon injects into a SD, the signal size is 1 VEM, while a muon injected with zenith angle 60° produces the signal size 2 VEM. The unit of S is VEM / 3 m^2, where 3 m^2 is the size of the detector area. The average lateral distribution of the TA SD data is calculated by the same method described in section 4.2. Figure 4.6 and 4.7 show the average lateral distributions of the data and the MC for $\theta < 30°$ and $30° < \theta < 45°$, respectively. The average values of the signal size of the data are larger than those of the MC in all the figures. The ratios of the data to the MC are also shown. The difference of the average signal size between the data and the MC is larger as $\theta, |\phi|$ and R values increase. In these figures, the vertical error bar represents the standard deviation divided by the root of the entries.

The upper and lower errors of the integrated FADC value are expected to be asymmetry in small statistics or non-Gaussian distribution. The lower error cannot be calculated at the distance $R >$ ~1.5 km because of the following reason. The lower (upper) error is different between the standard deviation of simple average and ±34% from the median value of the distribution. That corresponds to taking 16% and 84% statistics of the histogram within the lower and upper errors. The histograms at larger R is non-Gaussian and small statistics dominated by $S = 0$. Then, the lower limit of error at 16% includes

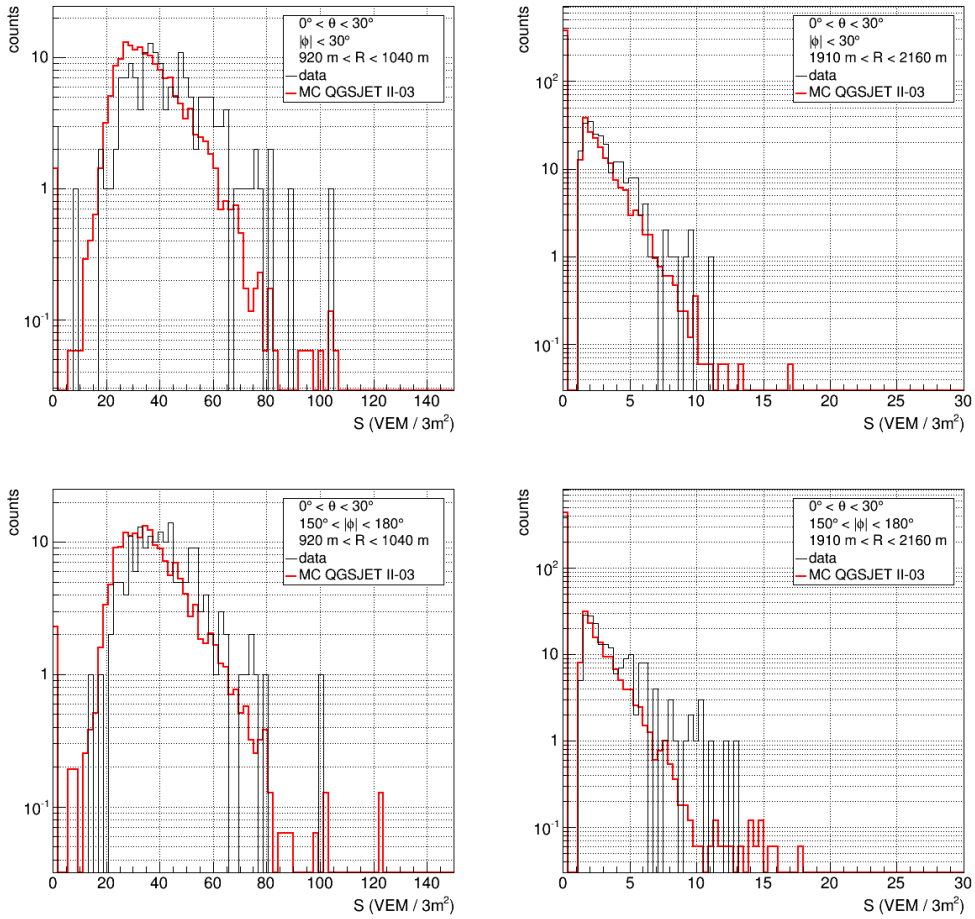

Figure 4.4: The histograms of the signal size for $\theta < 30°$. The black and red represent the data and the MC, respectively. (top left) $|\phi| < 30°$ and 920 m $< R <$ 1040 m. (top right) $|\phi| < 30°$ and 1910 m $< R <$ 2160 m. (bottom left) Same as the top left, but for $150° < |\phi| < 180°$. (bottom right) Same as the top right, but for $150° < |\phi| < 180°$. A bin at S=0 means the number of no hit detectors.

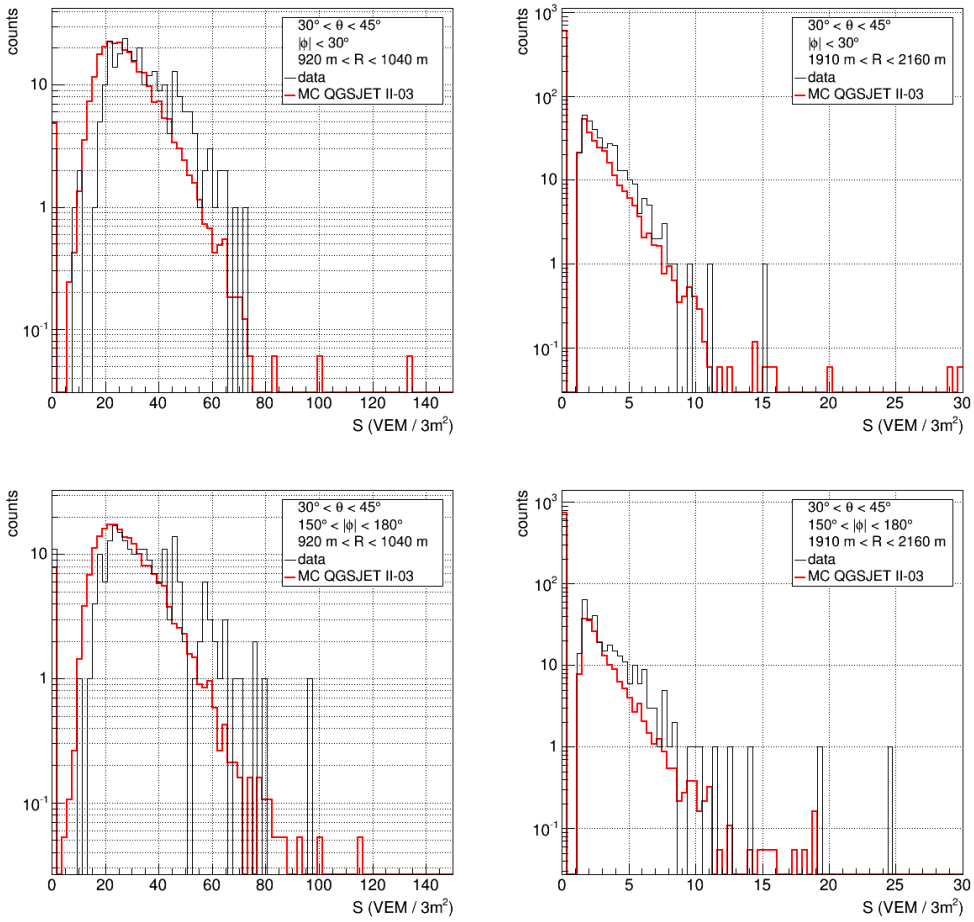

Figure 4.5: Same as figure 4.4, but for $30° < \theta < 45°$.

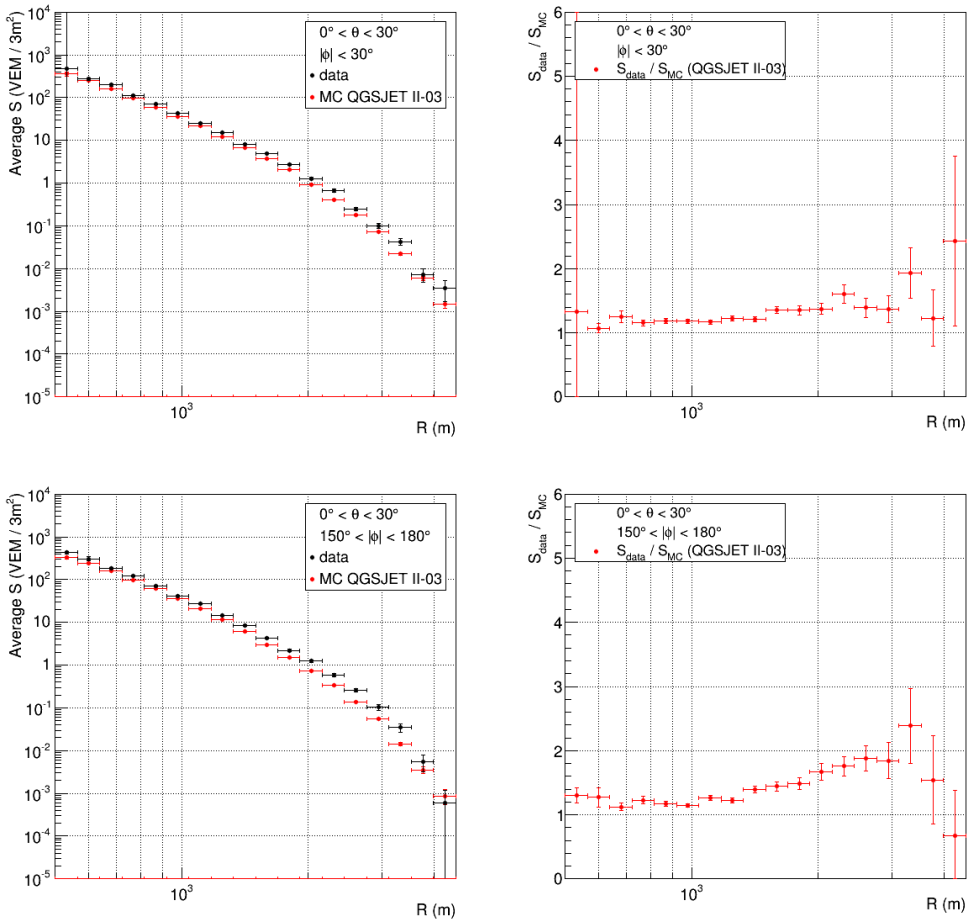

Figure 4.6: Lateral distributions of the average signal size and their ratios of the data to the MC for $\theta < 30°$. The vertical error bar shows the standard deviation divided by the root of the entries. (top left) The average lateral distributions for $|\phi| < 30°$. The black and red represent data and MC, respectively. (top right) The average ratio of the data to the MC for $|\phi| < 30°$. (bottom left) Same as the top left, but for $150° < |\phi| < 180°$. (bottom right) Same as the top right, but for $150° < |\phi| < 180°$.

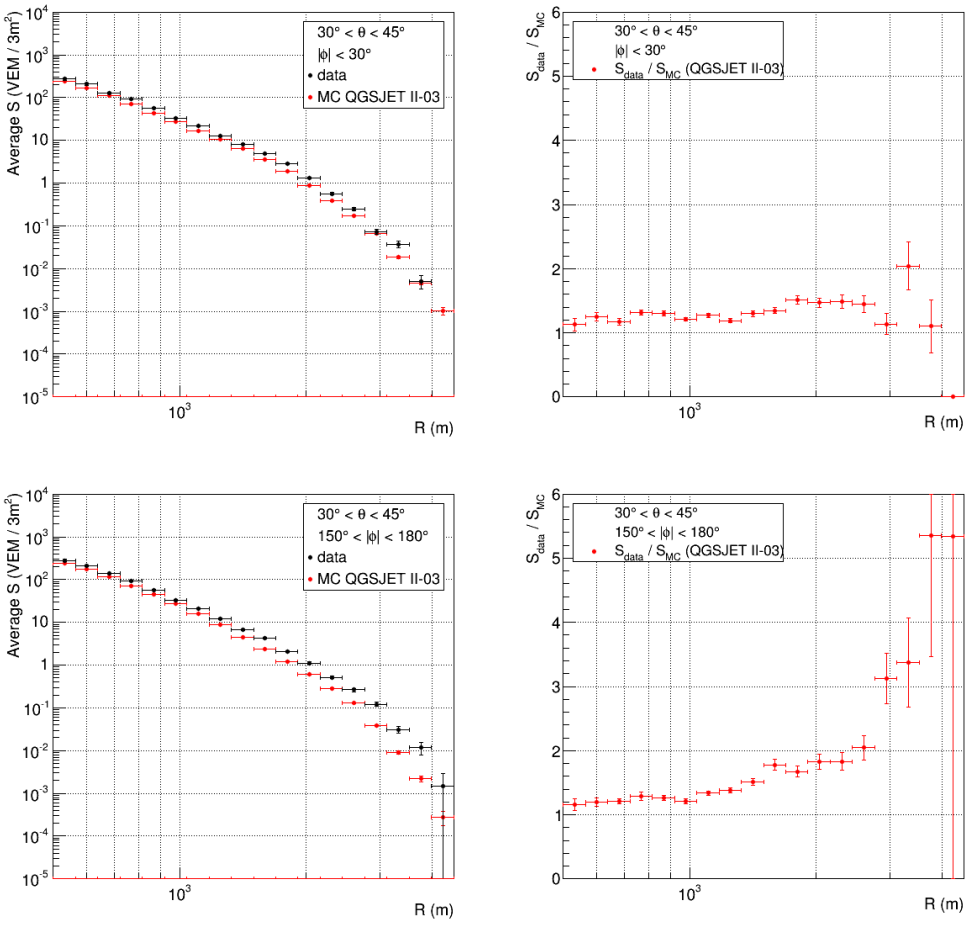

Figure 4.7: Same as figure 4.6, but for $30° < \theta < 45°$.

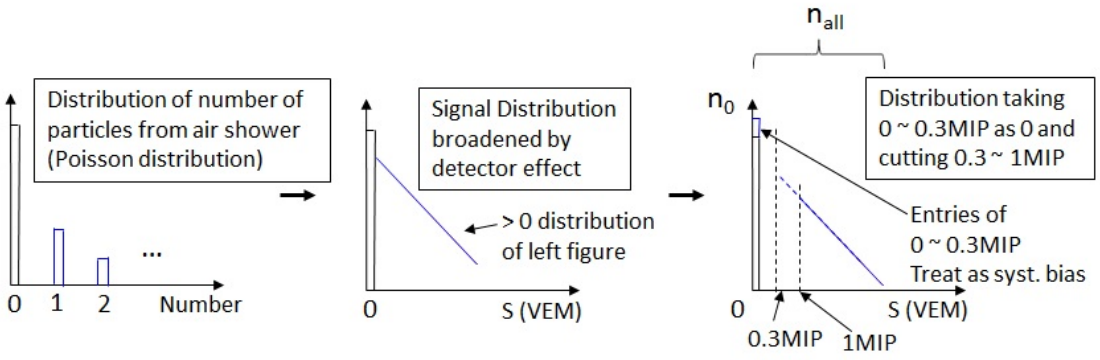

Figure 4.8: Schematics for the Poisson distribution assumption of the number of particles from in the air showers. The average value is assumed to be less than unity. A bin at 0 VEM means the number of no hit detectors.

0. Hence we used the different calculation method for the comparison of the data and the MC.

We denote the statistics of the $S = 0$ bin as n_0 and the all statistics of the histograms as $n_{\rm all}$. We calculate the average number of particles in each (θ, ϕ, R) condition by using n_0 and $n_{\rm all}$. This error calculation is based on the following idea.

- The number of particles from air showers which arrive on the SD in a (ϕ, R) bin is independent event by event and its distribution has an average value. Hence the number of particles is expected to follow the Poisson distribution, as described in figure 4.8 (left).
- The Poisson distribution is a discrete distribution of integer. Considering the detector resolution, the distribution of the number of particles becomes broadened without number 0 component when converting the distribution of the signal size. The schematic diagram is shown in figure 4.8 (center).
- The signal below about 0.3 MIPs is not recorded by a hardware threshold of the DAQ, namely the signal is counted as 0 VEM. The signal about 0.3 - 1 MIPs is cut by the software threshold to reduce background atmospheric muon contribution, and not included in the entries on the analysis. These effects occur the systematic bias of the difference from Poisson distribution. This will be treated as a source of the systematic uncertainty described in section 4.3. The schematic diagram is shown in figure 4.8 (right).

Poisson distribution is expressed as the following function.

$$f(x) = \frac{N^x e^{-N}}{x!} \tag{4.1}$$

Here N is the average value of the distribution and x is a variable. $f(x)$ is normalized to unity, hence the histogram mentioned above is expressed as $n_{\rm all} f(x)$. Therefore,

$$n_0/n_{\rm all} = f(0) = e^{-N} \tag{4.2}$$

The probability that zero values appear n_0 times in $n_{\rm all}$ sample follows the binomial distribution, so the standard deviation $\sigma_{\rm n0}$ of n_0 is

$$\sigma_{\rm n0} = \sqrt{n_{\rm all}\, p(1-p)} \tag{4.3}$$

where p is $n_0/n_{\rm all}$. From equations 4.2 and 4.3, N and its error are calculated. Note that the systematic error of the Poisson distribution assumption is large at $R < 1500$ m because n_0 decreases at a smaller R value, which will be described in section 4.3. This error calculation is adopted for only at $R > 1500$ m.

The muon purity in the signal is calculated by the revised MC. Figures 4.9 and 4.10 show the histograms of the signal size in each shower component obtained by the revised TA SD MC for $\theta < 30^\circ$ and $30^\circ < \theta < 45^\circ$, respectively. The software threshold of signal size of the total component (black histograms) is set to be about $S = 1.4$ VEM in the reconstruction procedure. The background component consists of pedestal fluctuation and atmospheric muons accidentally arriving in the air shower trigger time. For $\theta < 30^\circ, |\phi| < 30^\circ$ and $R \simeq 1000$ m (top left panel of figure 4.9), the EM components are dominant in the histogram. For $30^\circ < \theta < 45^\circ, 150^\circ < |\phi| < 180^\circ$ and $R \simeq 2000$ m (bottom right panel of figure 4.10), the muon component is dominant in the histogram. In the latter histogram, the peak value of the total component is about 1.8 VEM / 3 $\rm m^2$, which comes from the slant injection angle of the secondary particles.

Figures 4.11 and 4.12 are the lateral distributions and the muon purity in each R bin. The signal size of air shower particles decreases as R value increases. The lateral distribution of the muon component is flatter than that of EM components. That is because muons are less attenuated than EM particles in the air. We calculate the muon purity as the ratio of the average of signal size of the muons to that of the total component. In these figures, the muon purity calculated without the background component (atmospheric muons and pedestal fluctuation) is also shown by orange. The muon purity increases as the $\theta, |\phi|$ and R values increase, as expected from the above. The muon purity at around $R = 800$ m is 10 - 30%, where the signal size at the distance is used as the energy estimator in the TA spectrum analysis. For the condition ($30^\circ < \theta < 45^\circ, 150^\circ < |\phi| < 180^\circ$, 2000 m $< R <$ 4000 m), the muon purity increases to 60 - 70%, and we use this condition for the comparison of the signal size of air shower particles between the data and the MC.

The background signal size (Magenta plots in figures 4.11 and 4.12) decreases at $R > 1000$ m. This is due to the signal selection scheme in the event reconstruction. The background distribution originally should be the flat since the atmospheric muons comes on the ground randomly in space and time. If they come into the detector at

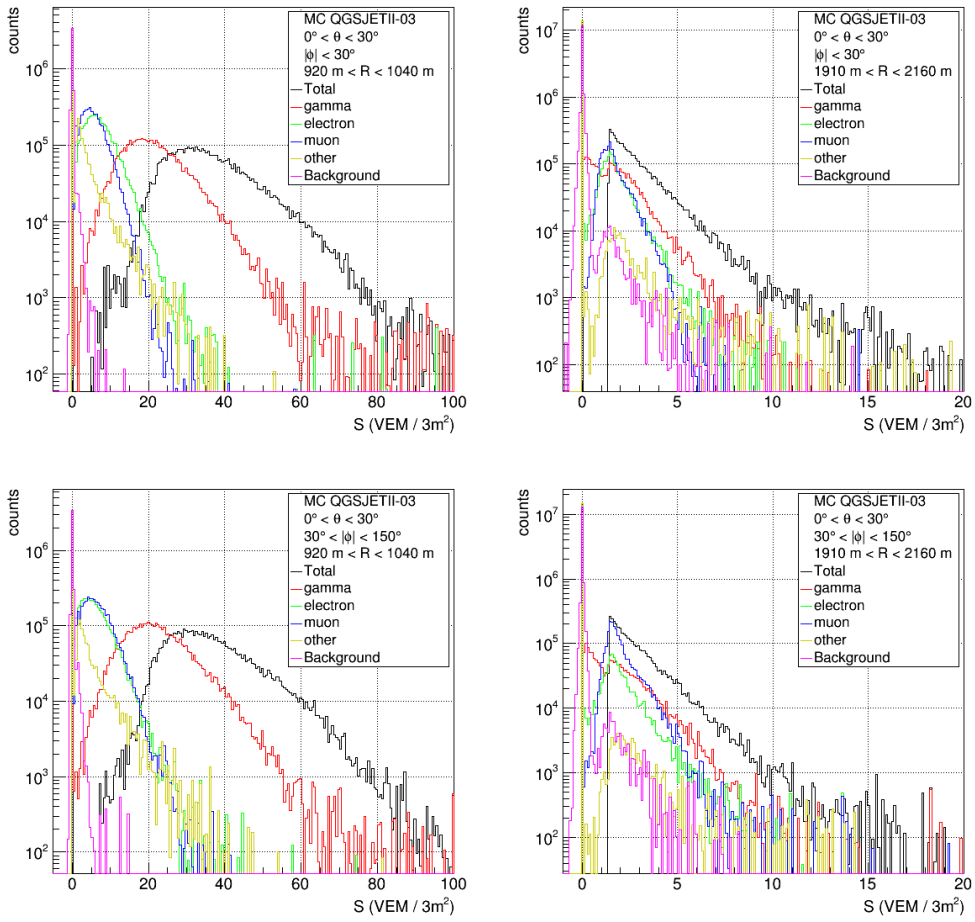

Figure 4.9: The histograms of the signal size for $\theta < 30°$. The red, green, blue, yellow, magenta and black represent gamma, electron, muon, other shower components, background and total of them, respectively. (top left) the histogram for $|\phi| < 30°$, 920 m $< R <$ 1040 m. (top right) the histogram for $|\phi| < 30°$, 1910 m $< R <$ 2160 m. (bottom left) Same as top left, but for $150° < |\phi| < 180°$. (bottom right) Same as top right, but for $150° < |\phi| < 180°$.

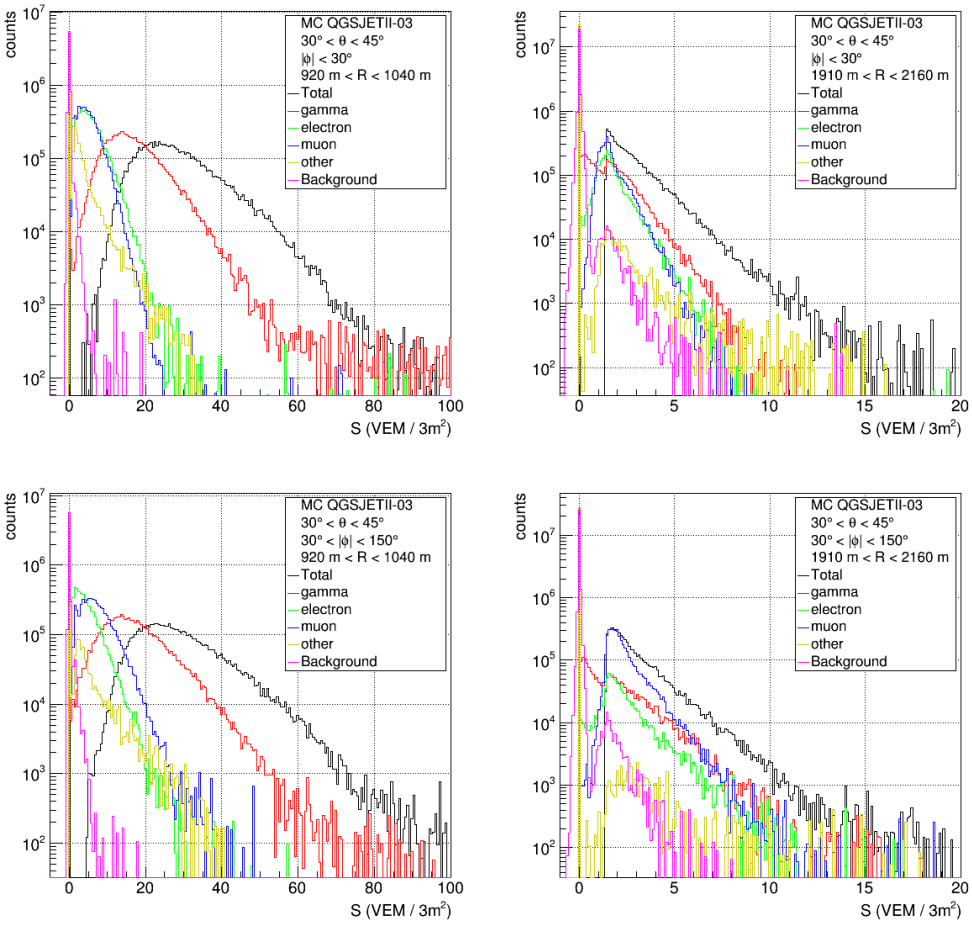

Figure 4.10: Same as figure 4.9, but for $30° < \theta < 45°$.

$R < \sim$1000 m in the shower event time width ($\pm 32\mu$s from the trigger time), they are possibly embedded in true air shower signals. But if they come at $R > \sim$1000 m, they often excluded by the space-time cluster cut, which is mentioned in section 2.3.1. This systematic effect to the comparison between the data and the MC will be evaluated in the next section.

4.3 Systematic errors

In the previous sections we calculated the signal size from air showers arriving at SDs on the muon-enriched condition. It is necessary to evaluate the systematic uncertainty of the signal size of the data. The possible sources of systematic uncertainty are the primary energy determination for events, the calibration of SDs, the background signal, Poisson distribution assumption for the signal size histogram, event reconstruction and detectors which are not working properly.

4.3.1 Energy determination uncertainty

In this analysis, the primary energy in the data obtained by the TA SD lateral distribution, reconstruction and response library from Geant4 MC is corrected by -27% to FD energy scale. This is caused by the discrepancy between the energy reconstructed by the SD and that by the FD in the hybrid events, and the FD energy is more reliable because it uses calorimetric EM signals from the longitudinal development of air showers. On the other hand, the primary energy in the MC is not corrected by -27% in this analysis. That enables to compare the data and the MC, including the energy scale discrepancy between the SD and the FD. More detailed explanation is described in section 5.3.

By changing the energy scale by -27% in an energy bin, the energy estimator $S800$ is shifted by $\sim$+27%. When the FD energy scale is used, it is necessary to consider the systematic uncertainty of FD energy measurement, which is 21% [68]. According to the generalized Heitler model of hadronic air showers [90], the number of particles of EM components $N_{\rm e}$ and muon component N_μ from the showers are predicted as

$$N_{\rm e} \propto E^{1.03} \tag{4.4}$$

$$N_\mu \propto E^{0.85} \tag{4.5}$$

where E is primary cosmic-ray energy. In the current analysis, the signal size corresponds to the number of particles and that on muon-enriched condition includes both EM and muon components, in which the muon purity is 60 - 70%. We conservatively assume $N \propto E$ in current analysis and add the systematic uncertainty by $\pm$21% to the signal size of the data.

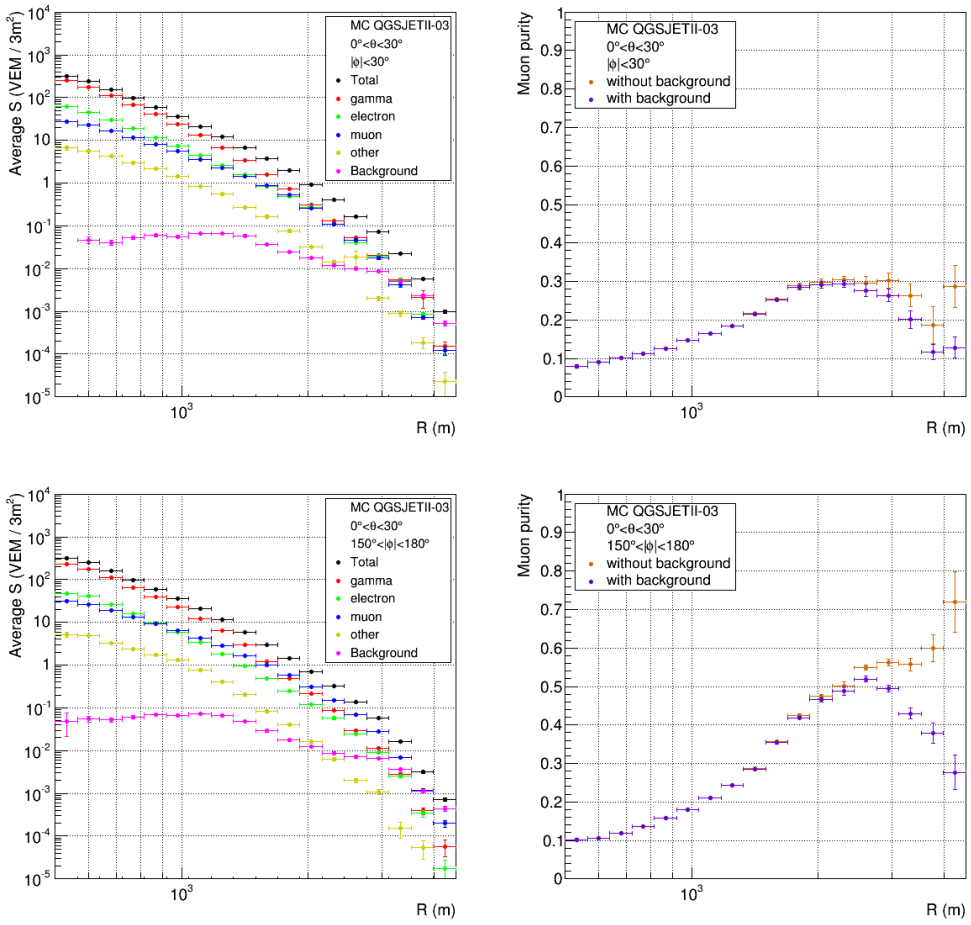

Figure 4.11: Lateral distributions of the average signal size and the muon purity for $\theta < 30°$. The vertical error bar shows the standard deviation divided by the root of the entries. (top left) The average lateral distributions for $|\phi| < 30°$. The red, green, blue, yellow, magenta and black points represent gamma, electron, muon, other shower components, background and the total of all components, respectively. (top right) The muon purity for $|\phi| < 30°$. The violet and orange points show the calculation with background and without background, respectively. (bottom left) Same as top left, but for $150° < |\phi| < 180°$. (bottom right) Same as top right, but for $150° < |\phi| < 180°$.

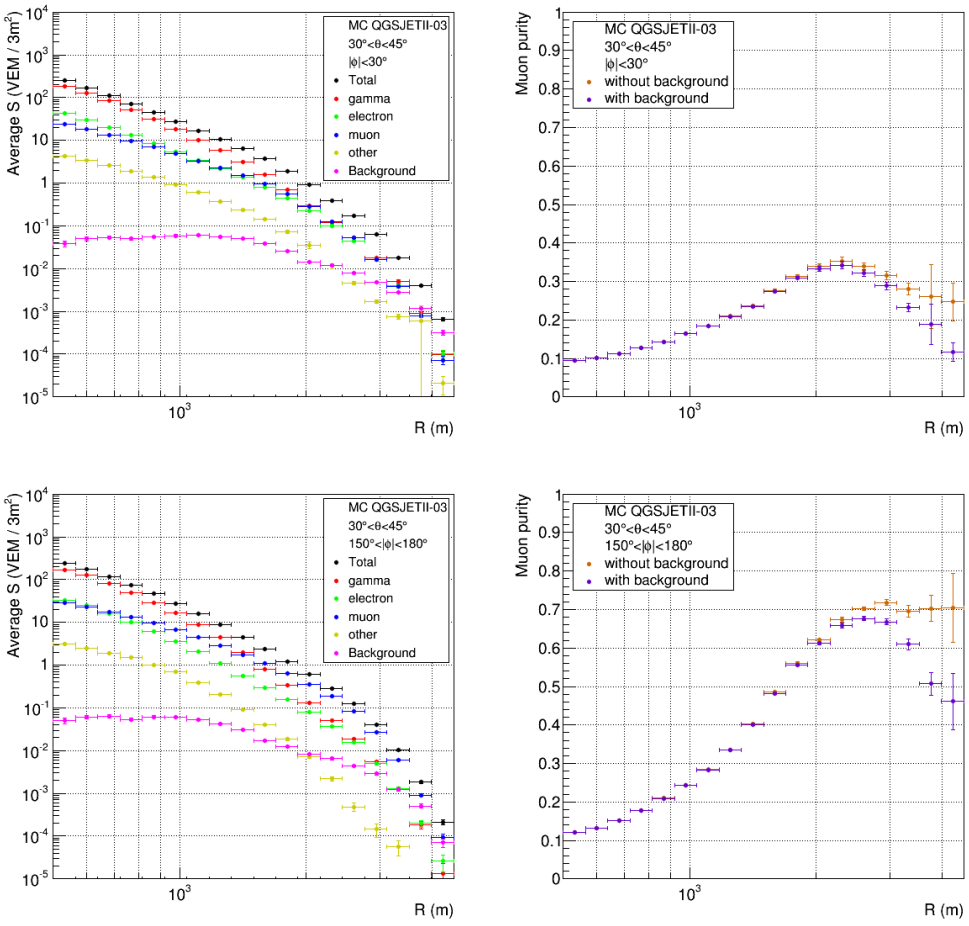

Figure 4.12: Same as figure 4.11, but for $30° < \theta < 45°$.

4.3.2 1 MIP calibration accuracy

The uncertainty of 1 MIP calibration contributes to the systematic error of the signal size. The signal size in VEM unit is calculated by fitting the histogram of the integrated FADC values of atmospheric muons and determining the peak value of the histogram. Here the integrated FADC values mean the sum of FADC signal bins of waveforms exceeding 5σ (the average pedestal subtracted). The histogram is created by the procedure described in section 2.2.3 in each SD every 10 min. to calibrate temperature dependence of 1 MIP value. The accuracy of the calibration method is $\epsilon_{\rm 1mip}/S_{\rm 1mip}$, where $S_{\rm 1mip}$ is the peak value of 1 MIP histogram (*cf.* section 2.2.2) determined by fitting and $\epsilon_{\rm 1mip}$ is the fitting error of $S_{\rm 1mip}$. The average value of the $\epsilon_{\rm 1mip}/S_{\rm 1mip}$ is calculated for all the detectors which have signals in all the air shower events. We take the systematic error as $\pm < \epsilon_{\rm 1mip}/S_{\rm 1mip} >= \pm 2\%$. The difference of the error in each (E, θ) condition is $\sim 0.01\%$.

The linearity of the PMTs does not affect to the systematic error because the average number of particles in each event is less than unity on the analysis condition of the present work.

4.3.3 Background muon contribution

Since TA SD muon analysis treats $R > \sim$2000 m where the average number of particles from air showers is less than unity, the background (atmospheric muon) contribution is important. The background signals decrease at $R > \sim$1000 m due to signal selection at the air shower reconstruction, as shown in figure 4.13. If the ratio of the background signal size to the total signal size ($S_{\rm B.G.}/S_{\rm total}$) is different between data and MC, that is the systematic error. $S_{\rm B.G.}/S_{\rm total}$ can be estimated by the MC. Since the ratio of the data is unknown, we conservatively set the systematic error as $S_{\rm B.G.}/S_{\rm total}$ of the MC, which is $\pm(S_{\rm B.G.}/S_{\rm total})/2 = \pm 0\%$ - 20%, depending on R.

4.3.4 Poisson distribution assumption

In this analysis, we calculated the average signal size from air showers in each (θ, ϕ, R) bin by assuming that the signal size distribution follows the Poisson distribution. This method provides the upper and lower statistical errors of the average signal size. Actually, the histograms of the signal size is somewhat different from the Poisson distribution due to two reasons. One is the air shower secondary particle reaction in the scintillator. A gamma ray is produces eectron and positron by the pair production reaction, so one particle generates two particle energy deposit. Also, low energy neutrons ($\sim$ 30 MeV - 50 MeV) produce recoil protons in the scintillator, which make large energy deposit, deserving 3 - 4 mip in the previous study [25]. They make tail components in the histograms of the integrated FADC values. The other reason is that the DAQ threshold enhances the signal size 0 component, as explained in figure 4.8. These effects make

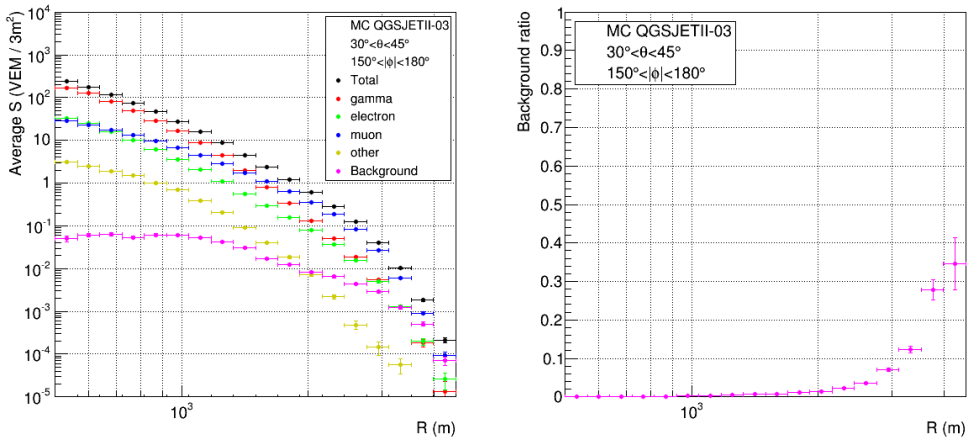

Figure 4.13: Lateral distributions of the average integrated FADC values and the background ratio for $30° < \theta < 45°, 150° < |\phi| < 180°$. The vertical error bar shows the standard deviation divided by the root of the entries. (Left) The lateral distributions of integrated FADC values, which is same as bottom left panel of figure 4.12. The red, green, blue, yellow, magenta and black points represent gamma, electron, muon, other shower components, background and the total of all components, respectively. (Right) The background ratio.

the bias to lower the average signal size calculated by assuming the Poisson distribution (denoted as N) than the simple average value of the histograms (denoted as S). It can be the systematic error if the bias of the Poisson distribution assumption is different between the data and the MC. Such situation may occur when muon fraction in the histogram is different between the data and the MC.

Figure 4.14 shows lateral distributions of $S_{\rm data}, S_{\rm MC}, N_{\rm data}, N_{\rm MC}$ and the bias between S and N. Here $S_{\rm data}, S_{\rm MC}$ are the signal size in the data and the MC, respectively and $N_{\rm data}, N_{\rm MC}$ are those assuming the Poisson distribution. The bias A is calculated as $A = (S - N)/N$. The systematic error is estimated to be $\pm| < A_{\rm data} > - < A_{\rm MC} > |/2$. Here the statistical error of A is neglected. The systematic error value is, for example, $\pm 8\%$ on condition $30° < \theta < 45°, 150° < |\phi| < 180°, R \sim 2000$ m.

4.3.5 Air shower reconstruction

Accuracy of core position determination is a possible source of systematic bias. The signal size of air showers is larger in the shower arrival direction than the shower forwarding direction, compared in the same R. In the TA SD reconstruction procedure, SDs used in lateral distribution fitting are not distinguished by azimuth angle, thus the reconstructed core position is biased on the side of the air shower arrival direction. Figure 4.15 shows the bias between reconstructed core position and input one with input

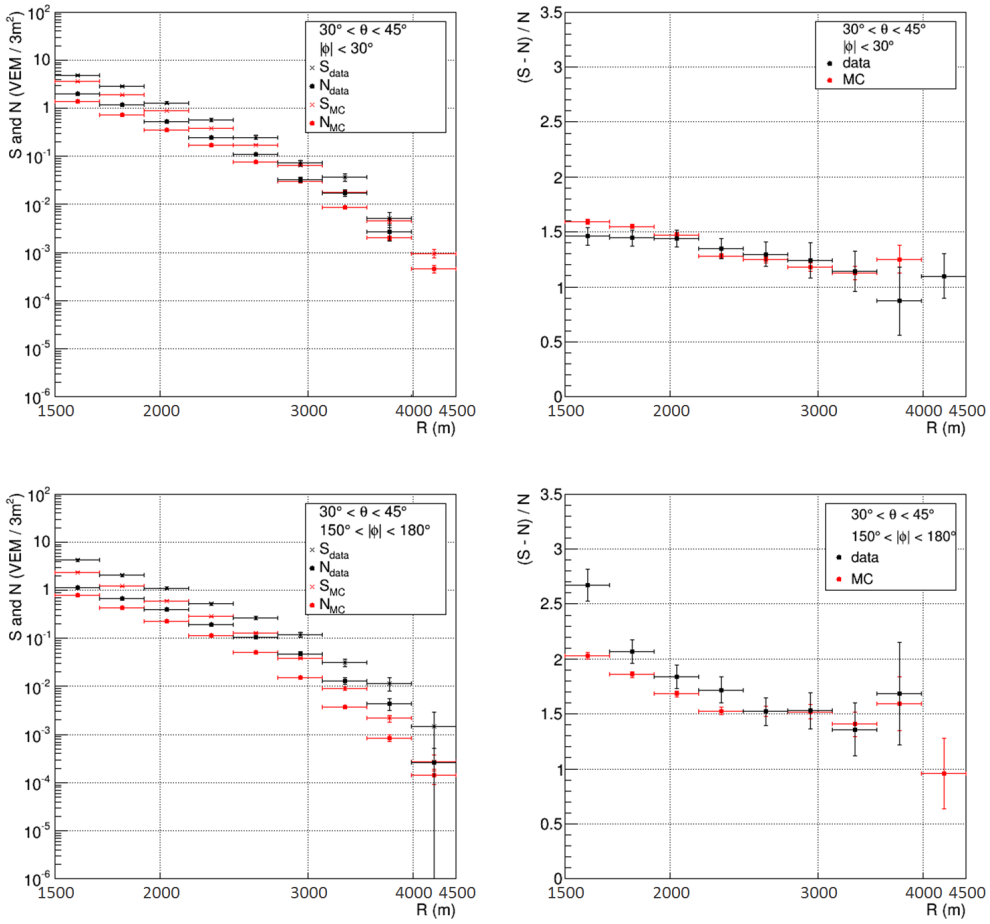

Figure 4.14: Lateral distributions of S (simple average) and N (Poisson assumption) for the data and the MC on condition $30° < \theta < 45°$ and 1500 m $< R <$ 4500 m. The black and red points represent data and MC, respectively. The cross and filled circle represent S and N, respectively. (top left) Lateral distributions of S and N for $|\phi| < 30°$. (top right) The bias $(S - N)/N$, which is denoted as A in the text, for $|\phi| < 30°$. The vertical error bars are calculated by the error of N. (bottom left) Same as the top left figure, but for $150° < |\phi| < 180°$. (bottom right) Same as the top right figure, but for $150° < |\phi| < 180°$.

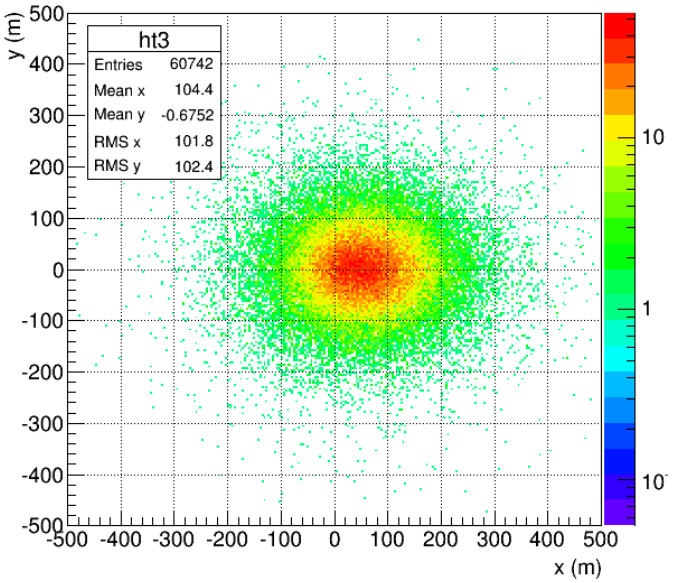

Figure 4.15: Bias between reconstructed core position and input one with input shower axis for $30^\circ < \theta < 45^\circ$ calculated by the MC using QGSJET II-03 for proton. The horizontal and longitudinal axes represent the coordinates x and y of the reconstructed core positions with respect to input ones, respectively. The positive direction of x axis corresponds to the input shower arrival direction projected onto the ground.

shower axis calculated by the MC. There is a systematic shift of the reconstructed core position by about 100 m to the shower arrival direction for $30^\circ < \theta < 45^\circ$. Such shift makes the bias to lateral distributions in each (θ, ϕ) condition.

The asymmetry of the number of air shower particles between air shower arrival direction and forwarding direction is caused by attenuation of the particles in the atmosphere. Comparing the number of particles between arrival and forwarding directions, the EM components are more attenuated than muons. Thus if the excess occurs in the data and the ratio of the signal size of muons to that of EM components is different between the data and the MC, the asymmetry is expected to be different. It may cause different core position bias between the data and the MC, which becomes systematic errors in comparison of them. The actual bias in the data cannot be known. Hence we conservatively take the systematic error from the bias of the MC.

Figure 4.16 shows average lateral distributions of the signal size of the MC with reconstructed event parameters (energy, zenith angle, azimuth angle and core position) $N_{\rm rec}$ and same with input ones $N_{\rm in}$, and the bias of them. Here $N_{\rm rec}$ corresponds to N described in other sections. The bias is $B = (N_{\rm in} - N_{\rm rec})/N_{\rm rec}$, and the systematic error is calculated by $\pm < B > /2$. Here the statistical error of B is neglected. The error value is, for example, $\pm 4\%$ on condition $30^\circ < \theta < 45^\circ, 150^\circ < |\phi| < 180^\circ, R \sim 2000$ m.

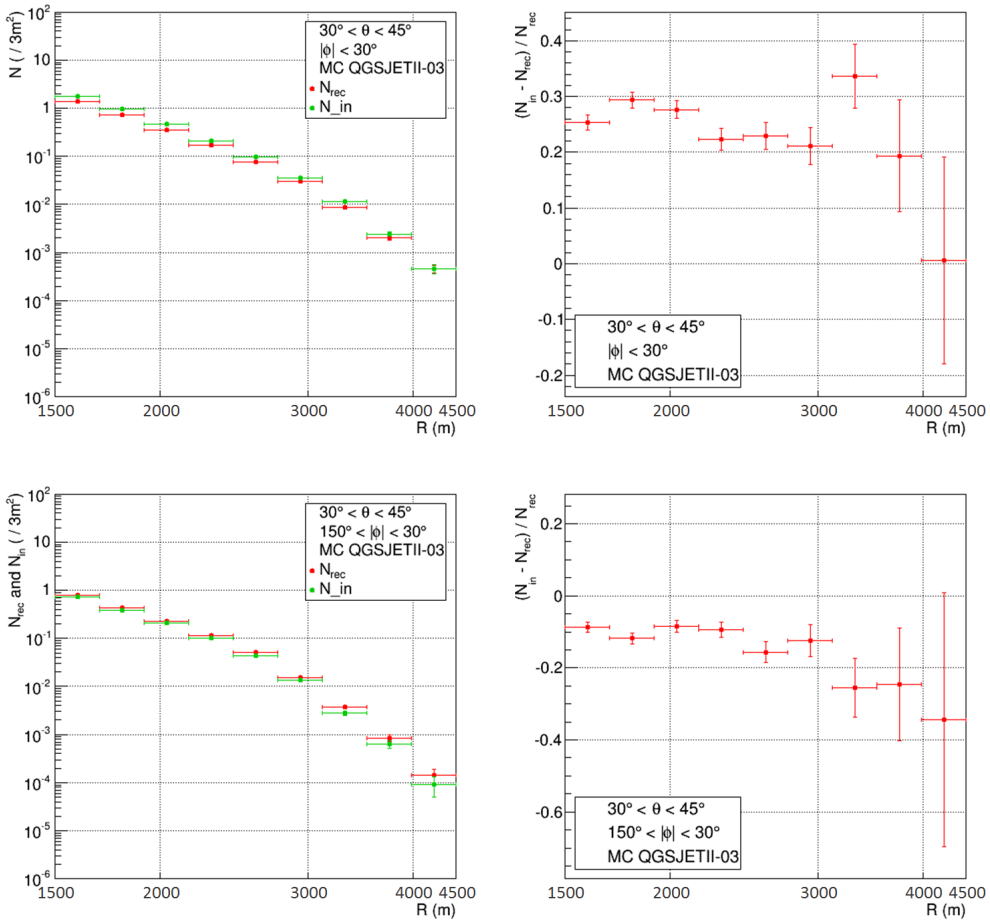

Figure 4.16: Lateral distributions of $N_{\rm rec}$, $N_{\rm in}$ and the bias between them of the MC for $30^\circ < \theta < 45^\circ$, 1500 m $< R <$ 4500 m. (top left) Lateral distributions for $|\phi| < 30^\circ$. The red and green points represent $N_{\rm rec}$ and $N_{\rm in}$, respectively. (top right) The bias $(N_{\rm in} - N_{\rm rec})/N_{\rm rec}$, which is denoted as B in the text, for $|\phi| < 30^\circ$. (bottom left) Same as top left, but for $150^\circ < |\phi| < 180^\circ$. (bottom right) Same as top right, but for $150^\circ < |\phi| < 180^\circ$.

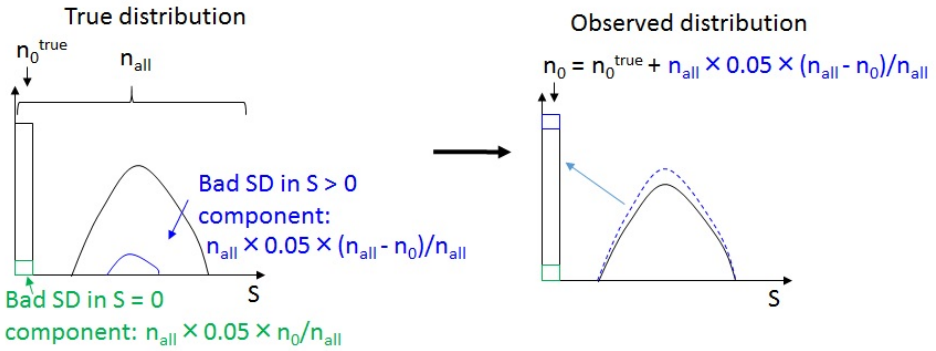

Figure 4.17: Bias of observed signal size distribution. (Left) True distribution. The blue represents the case where the shower particles penetrate detectors but the detectors are not working properly. The green represents the case where the shower particles do not penetrate detectors and the detectors are not working properly. The sum of the green and the blue is $n_{\rm all} \times 5\%$. (Right) Observed distribution. $n_0^{\rm true}$ can be calculated from $n_{\rm all}$ and n_0.

4.3.6 Bad detector

The averaged duty cycle of the SD array is approximately 95%, hence 5% of SDs in the event dataset is expected to be not working properly. Here we call the SD which is not working properly as the bad detector. Actually, the event trigger and reconstruction process can remove such bad detectors from the observed event dataset, but we conservatively treat them as 5% here. The bad detector should be excluded from the calculation of the average signal size, but it is counted as signal size $S = 0$ in the present work. The difference of that contribution between the data and the MC is not studied yet because it might be small systematics for the event reconstruction. In this work, the $S = 0$ component is important, hence the systematic error from this effect is estimated as follows.

In the calculation of the signal size N, we use the parameter n_0 and $n_{\rm all}$ as described in section 4.2. The measured n_0 is slightly overestimated by the bad detector. The relation between n_0 and $n_0^{\rm true}$ is described in figure 4.17. The bias to the value of N is calculated as

$$C = \frac{\ln(n_{\rm all}/n_0^{\rm true}) - \ln(n_{\rm all}/n_0)}{\ln(n_{\rm all}/n_0)} \tag{4.6}$$

The systematic error of N value is set to be $\pm|C_{\rm data} - C_{\rm MC}|/2$. It is $\sim 1\%$ in all (θ, ϕ) at 2000 m $< R <$ 4000 m. For example, on condition $30^\circ < \theta < 45^\circ, 150^\circ < |\phi| < 180^\circ, R \sim 2000$ m (corresponding to bottom right panel in figure 4.5), ($n_{\rm all}$, n_0) = (932, 631) for data and (17116, 13650) for MC, respectively. $n_0^{\rm true}$ can be calculated from $n_{\rm all}$ and n_0. Then $C_{\rm data} = 6.2\%$, $C_{\rm MC} = 5.6\%$ and the systematic error is estimated to be $\pm|C_{\rm data} - C_{\rm MC}|/2 = 0.3\%$.

Table 4.2: Systematic uncertainties of the signal size on the condition $30^\circ < \theta < 45^\circ$, $150^\circ < |\phi| < 180^\circ$ and 2000 m $< R <$ 4000 m.

Source	Systematic error	Remark
Energy determination	21%	
1 MIP calibration	2%	
Background muon	0% - 15%	R dependence
Poisson distribution assumption	5% - 10%	R dependence
Air shower reconstruction	5% - 10%	R dependence
Bad detector	$\sim$ 1%	R dependence
Total	22% - 29%	R dependence

4.3.7 Total systematic uncertainty

Table 4.2 summarizes all the systematic uncertainties of the signal size N of the data. The error values depend on (θ, ϕ, R) conditions, and we described the values on the muon-enriched condition ($30^\circ < \theta < 45^\circ$, $150^\circ < |\phi| < 180^\circ$ and 2000 m $< R <$ 4000 m). The energy determination uncertainty is dominant in this analysis.

4.4 Results

4.4.1 Results assuming proton using QGSJET II-03 model

Figures 4.18 and 4.19 show the lateral distributions of the signal size. The ratios of the signal size of the data to that of the MC are also shown. The average signal size decreases slower in the data than the MC when R is larger, namely larger difference of the number of particles at larger $|\phi|$ and R values. The error σ_{n0} also becomes larger at larger R value. The significance of the discrepancy between the data and the MC is calculated by

$$\frac{(N_{\mathrm{data}}/N_{\mathrm{MC}} - 1)}{\sigma_{\mathrm{ratio}}} \tag{4.7}$$

where σ_{ratio} is the lower error of $N_{\mathrm{data}}/N_{\mathrm{MC}}$. Table 4.3 shows the parameters of the results. The significance varies within 1.6 - 2.7σ at R = 2000 - 4000 m. The maximum significance appears around 3000 m since the average value of the ratio becomes larger, but the error also becomes larger at further lateral distance. The typical ratios of the signal size of the data to the MC for proton using QGSJET II-03 model are

$1.72 \pm 0.10(\mathrm{stat.}) \pm 0.40(\mathrm{syst.})$ (1910 m $< R <$ 2160 m)

$3.14 \pm 0.36(\mathrm{stat.}) \pm 0.72(\mathrm{syst.})$ (2760 m $< R <$ 3120 m)

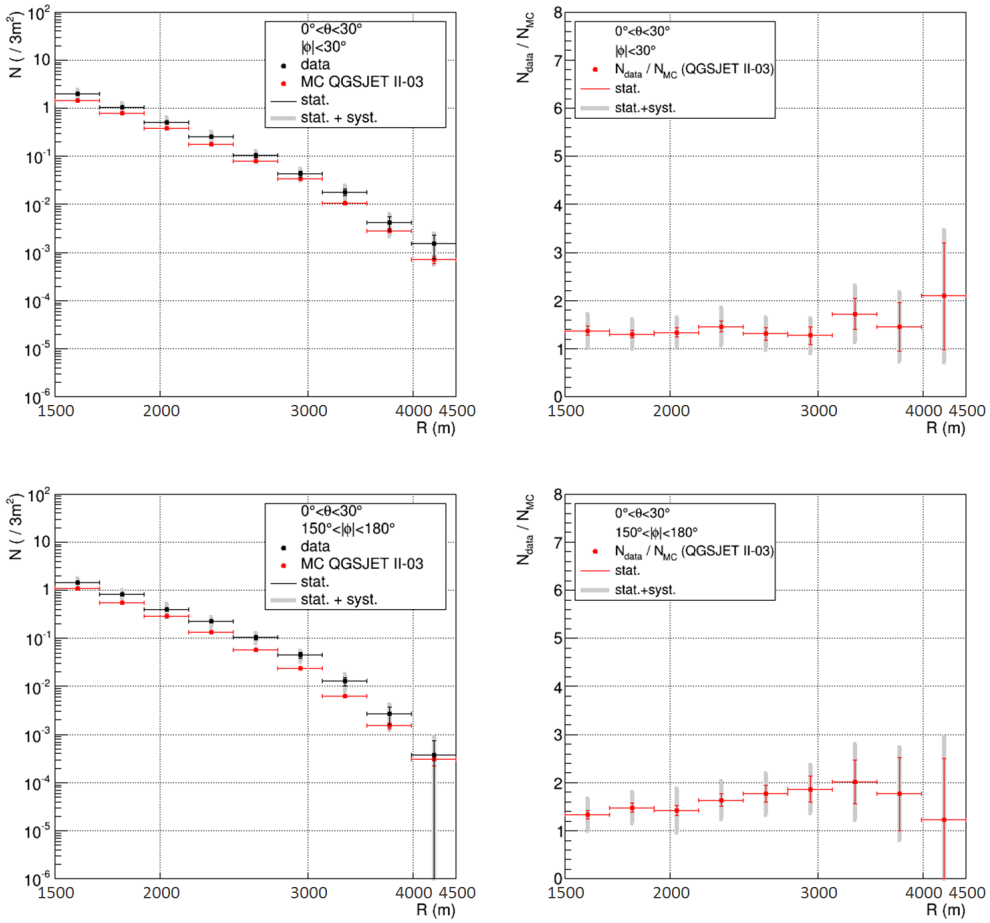

Figure 4.18: Lateral distribution of integrated FADC values assuming Poisson distribution and its ratio of the data to the MC for $\theta < 30°$, 1500 m $< R <$ 4500 m. The vertical thin error bars and shaded grey thick error bars represent statistical error and quadratic sum of statistical and systematic errors, respectively. (top left) The lateral distribution for $|\phi| < 30°$. The black and red points represent data and MC, respectively. (top right) The ratio of the data to the MC for $|\phi| < 30°$. (bottom left) Same as top left, but for $150° < |\phi| < 180°$. (bottom right) Same as top right, but for $150° < |\phi| < 180°$.

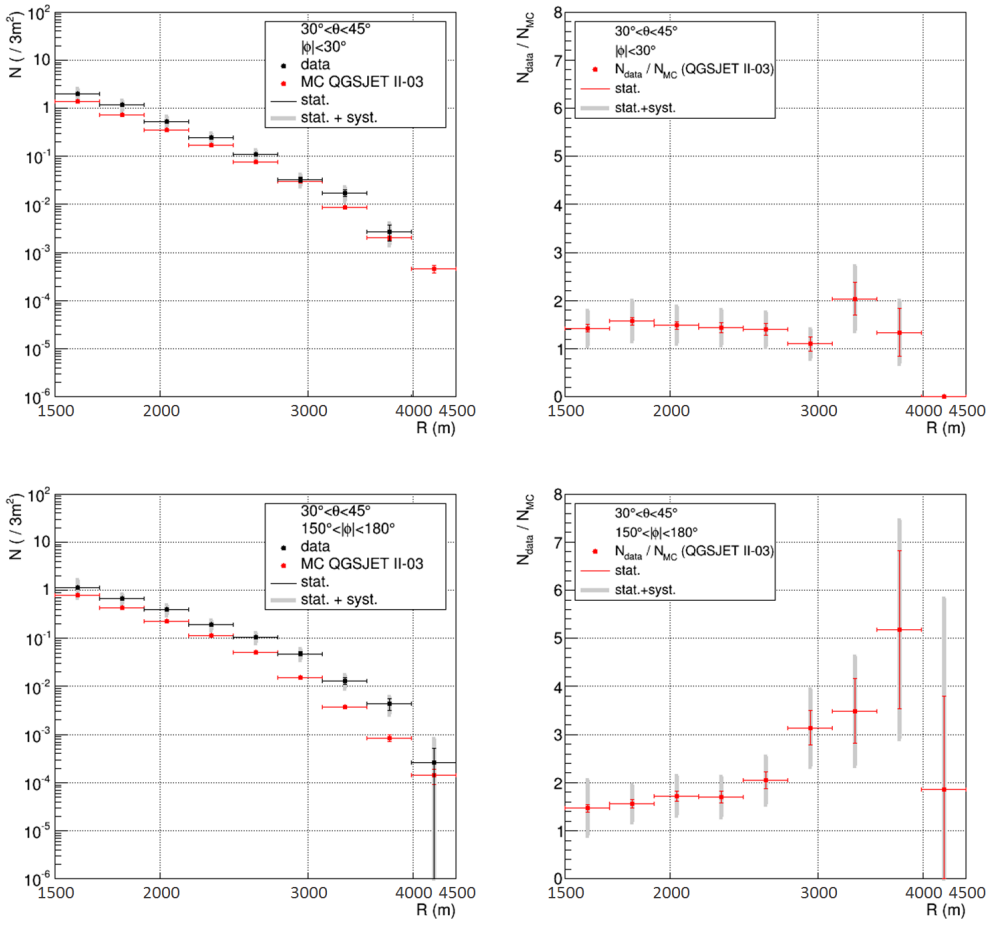

Figure 4.19: Same as figure 4.18, but for $30° < \theta < 45°$.

Table 4.3: The signal size in various R regions for $30^\circ < \theta < 45^\circ$ and $150^\circ < |\phi| < 180^\circ$. The errors include statistical and systematic errors.

R (m)	$N_{\rm data}$	$N_{\rm MC}$	$N_{\rm data}/N_{\rm MC}$	significance (σ)
[1500, 1695]	$1.147^{+0.451}_{-0.450}$	$0.782^{+0.011}_{-0.011}$	$1.47^{+0.58}_{-0.58}$	0.8
[1695, 1915]	$0.666^{+0.166}_{-0.166}$	$0.428^{+0.007}_{-0.007}$	$1.56^{+0.39}_{-0.39}$	1.4
[1915, 2160]	$0.390^{+0.092}_{-0.092}$	$0.226^{+0.004}_{-0.004}$	$1.72^{+0.41}_{-0.41}$	1.8
[2160, 2445]	$0.191^{+0.047}_{-0.047}$	$0.113^{+0.002}_{-0.002}$	$1.69^{+0.42}_{-0.42}$	1.6
[2445, 2760]	$0.105^{+0.003}_{-0.003}$	$0.0512^{+0.0014}_{-0.0014}$	$2.05^{+0.50}_{-0.50}$	2.1
[2760, 3120]	$0.0479^{+0.0121}_{-0.0121}$	$0.0153^{+0.0007}_{-0.0007}$	$3.14^{+0.80}_{-0.80}$	2.7
[3120, 3525]	$0.0132^{+0.0042}_{-0.0042}$	$0.00380^{+0.00030}_{-0.00030}$	$3.49^{+1.14}_{-1.14}$	2.2
[3525, 4180]	$0.00436^{+0.00179}_{-0.00179}$	$0.000842^{+0.00013}_{-0.00013}$	$5.18^{+2.27}_{-2.27}$	1.8
[4180, 4500]	$0.000260^{+0.000552}_{-0.000552}$	$0.000140^{+0.0000468}_{-0.0000467}$	$1.85^{+3.98}_{-3.98}$	0.2

4.4.2 Results assuming proton with different hadronic models

Figures 4.20 and 4.21 are the same figures as figures 4.18 and 4.19 but for various MC hadronic interaction models; QGSJET II-03, QGSJET II-04, Epos 1.99 [88], Sibyll 2.1 [89]. For all the models, the signal size of the data is larger than the MC in the similar level to QGSJET II-03 model. The difference between the data and the MC is larger at larger $\theta, |\phi|$ and R values. The difference among the models cannot be recognized beyond the statistical errors.

4.4.3 Results assuming iron with QGSJET II-03 model

Cosmic rays which are heavier than iron are unfavorable if the source is astrophysical objects. We generated the lateral distributions assuming iron with QGSJET II-03 model by the MC, and compared with that of the data. The MC input and analysis conditions are shown in table 4.4. Figure 4.22 shows the lateral distributions of average integrated FADC values in each particle type and the muon purity on muon-enriched condition. Figure 4.23 shows the lateral distributions of the muon purity assuming proton and iron by the MC. The muon purity for iron is larger by about 5% than proton.

Table 4.4: The input and analysis conditions of MC for iron

	E (eV)	θ ($^\circ$)	comment
input	$10^{18.55} - 10^{19.35}$	[0, 60]	
analysis	$10^{18.8} - 10^{19.2}$	[0, 45]	quality cut for spectrum

Figure 4.24 shows the lateral distributions of the signal size assuming the Poisson distribution. The average signal size in the MC for iron is smaller than the data at

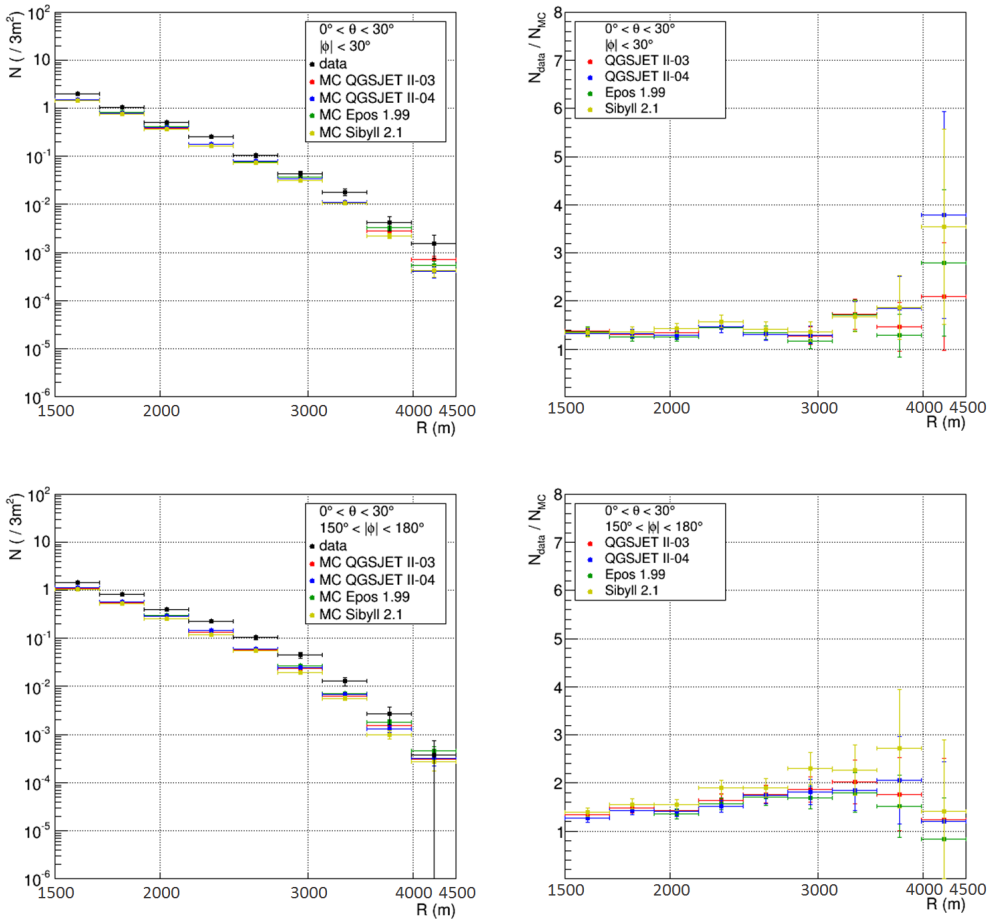

Figure 4.20: Lateral distributions of signal size assuming Poisson distribution and its ratio of the data to the MC for $\theta < 30°$, 1500 m $< R <$ 4500 m with various hadronic models. The proton primary composition is used. The vertical error bars represent statistical error. (top left) The average lateral distribution for $|\phi| < 30°$. The black, red, blue, green and yellow points represent data, MC QGSJET II-03, MC QGSJET II-04, MC Epos 1.99 and MC Sibyll 2.1, respectively. (top right) The ratio of the data to the MC for $|\phi| < 30°$. The color corresponds to MC hadronic models described in the top left figure. (bottom left) Same as top left, but for $150° < |\phi| < 180°$. (bottom right) Same as the top right, but for $150° < |\phi| < 180°$.

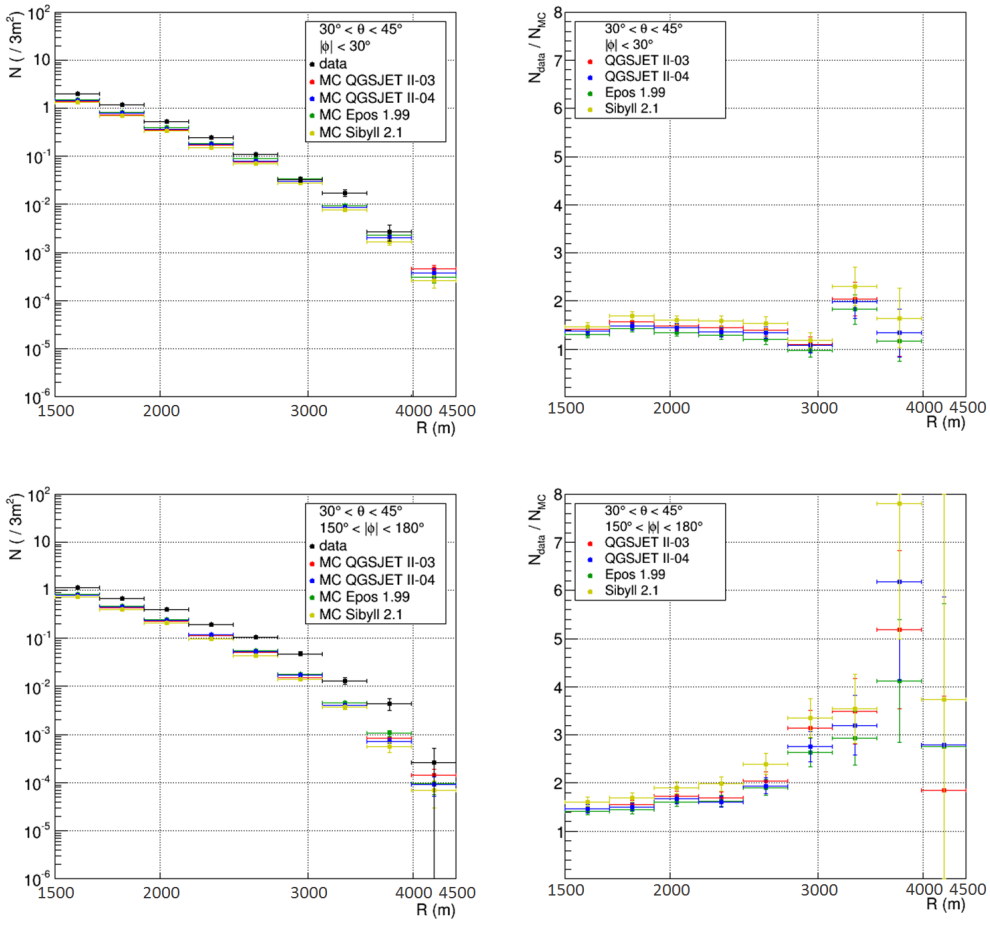

Figure 4.21: The same as figure 4.20, but for $30° < \theta < 45°$.

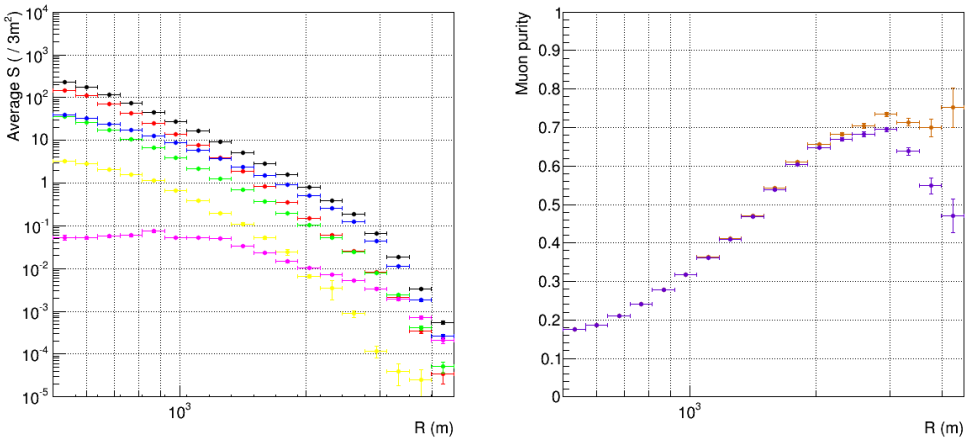

Figure 4.22: Lateral distributions of the average integrated FADC values and the muon purity for ($30° < \theta < 45°, 150° < |\phi| < 180°$, 500 m $< R <$ 4500 m) using the MC for iron. The vertical error bar shows the standard deviation of the average integrated FADC values. (left) The average lateral distributions. The red, green, blue, yellow, magenta and black points represent gamma, electron, muon, other shower components, background and the total of all components, respectively. (right) The muon purity. The violet and orange show the calculations with background and without background, respectively.

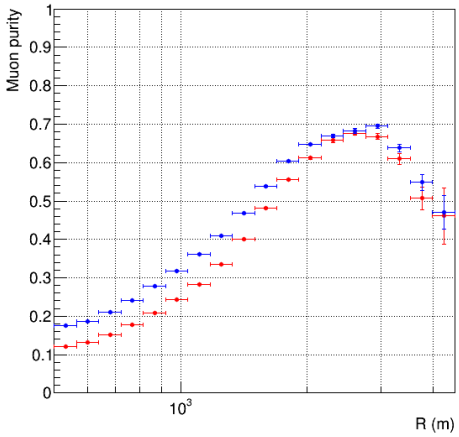

Figure 4.23: Lateral distributions of the muon purity for ($30° < \theta < 45°, 150° < |\phi| <$ 180°, 500 m $< R <$ 4500 m). The red and blue points represent MCs for proton and iron, respectively.

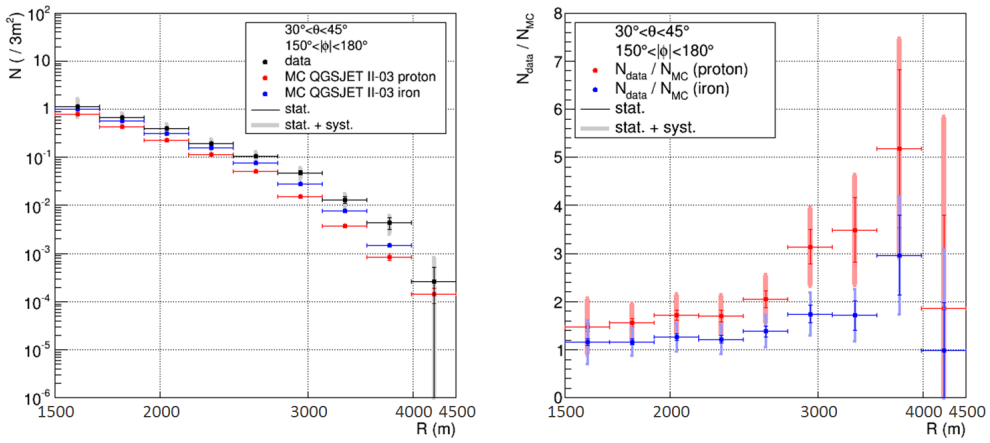

Figure 4.24: Lateral distributions of the signal size and the ratios of the data to the MC for ($30^\circ < \theta < 45^\circ, 150^\circ < |\phi| < 180^\circ$, 500 m $< R <$ 4500 m), using the MC for proton and iron. The vertical thin error bars and shaded thick error bars represent the statistical errors and the quadratic sum of statistical and systematic errors, respectively. (left) The average lateral distributions. The black, red and blue points represent experimental data, MC for proton and MC for iron, respectively. (right) The ratios of the data to the MC. The red and blue points represent the ratio of the data to the MC for proton and that for iron, respectively.

$R \sim 3000$ m. For other R conditions, they are within systematic errors. The average signal size for iron is larger than that for proton. The typical ratios of the number of particles of the data to the MC for iron are

$1.26 \pm 0.07(\text{stat.}) \pm 0.29(\text{syst.})$ (1910 m $< R <$ 2160 m)

$1.74 \pm 0.19(\text{stat.}) \pm 0.40(\text{syst.})$ (2760 m $< R <$ 3120 m)

The signal size of the data is larger than that of the MC for iron with $> 1\sigma$ significance in $R >$ 3000 m. The feature that the signal size of the MC for iron is closer to that of the data than the MC for proton and its average value is smaller than the data is similar to the muon excess reported by the Auger experiment [11].

4.4.4 Comparison among different muon purity conditions

In the above analysis, we studied the SD data within the muon-enriched (θ, ϕ) conditions. On the different (θ, ϕ) conditions, the geometry relation between the shower axis and the SD is different, hence the muon purity depends on (θ, ϕ) conditions in the analysis. To verify that the difference in the signal size between the data and the MC

on the analysis condition is caused by muons, we checked the correlation between the muon purity and the ratio of the data to the MC by changing (θ, ϕ) condition. Figure 4.25 is the correlation between the muon purity expected from the MC and the ratio of the signal size of the data to that of the MC. The colors show ϕ condition and the markers represent θ condition. The R condition is fixed from 2000 m to 4000 m. A data point corresponds to one (θ, ϕ) condition. The value for each point are summarized in table 4.5.

The muon purity and the ratio of the data to the MC at the muon-enriched condition is 65% and $1.88 \pm 0.08(\text{stat.}) \pm 0.43(\text{syst.})$ ($30^\circ < \theta < 45^\circ, 150^\circ < |\phi| < 180^\circ, 2000$ m $< R <$ 4000 m, magenta filled circle in figure 4.25), respectively. On the other hand, those values at the muon-less condition are 28% and $1.30 \pm 0.06(\text{stat.}) \pm 0.31(\text{syst.})$ ($\theta < 30^\circ, |\phi| < 30^\circ, 2000$ m $< R <$ 4000 m, black open circle in figure 4.25), respectively. The plots show larger difference of signal size between the data and the MC at the larger muon purity. This result indicates that part of the discrepancy between the data and the MC is caused by the muon excess in the data.

In addition, we checked the correlation between the muon purity and the ratio of signal size of the data to the MC for the air shower events with $45^\circ < \theta < 55^\circ$ (cross marks in the figure 4.25). On this condition, we adopted the same event quality cut for the SD spectrum analysis [12] except zenith angle condition. The correlation plots for $45^\circ < \theta < 55^\circ$ shows larger differences between the data and the MC, compared with that of $\theta < 45^\circ$. At the $|\phi| < 30^\circ$ and $30^\circ < |\phi| < 60^\circ$, $N_{\text{data}}/N_{\text{MC}}$ for $45^\circ < \theta < 55^\circ$ is smaller than that for $30^\circ < \theta < 45^\circ$, although it is within systematic error.

Table 4.5: The ratios and significance values for 2000 m $< R <$ 4000 m. The errors include statistical and systematic errors.

θ (°)	$\|\phi\|$ (°)	$N_{\text{data}}/N_{\text{MC}}$	significance (σ)
[0, 30]	[0, 30]	1.30 ± 0.31	1.0
[0, 30]	[30, 60]	1.36 ± 0.32	1.1
[0, 30]	[60, 90]	1.32 ± 0.30	1.1
[0, 30]	[90, 120]	1.41 ± 0.33	1.2
[0, 30]	[120, 150]	1.64 ± 0.36	1.8
[0, 30]	[150, 180]	1.59 ± 0.40	1.5
[30, 45]	[0, 30]	1.41 ± 0.35	1.2
[30, 45]	[30, 60]	1.53 ± 0.37	1.4
[30, 45]	[60, 90]	1.50 ± 0.33	1.5
[30, 45]	[90, 120]	1.63 ± 0.35	1.8
[30, 45]	[120, 150]	1.83 ± 0.40	2.1
[30, 45]	[150, 180]	1.88 ± 0.43	2.0

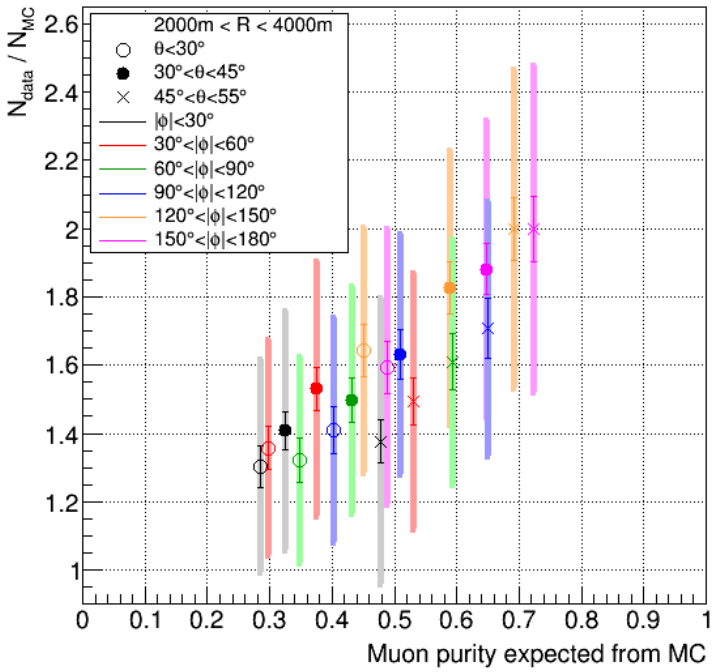

Figure 4.25: Correlation between the muon purity and the signal size ratio of the data to the MC for 2000 m $< R <$ 4000 m. The black, red, green, blue, yellow and magenta points represent $|\phi| < 30°$, $30° < |\phi| < 60°$, $60° < |\phi| < 90°$, $90° < |\phi| < 120°$, $120° < |\phi| < 150°$, $150° < |\phi| < 180°$, respectively. The open circle, filled circle and cross represent $\theta < 30°$, $30° < \theta < 45°$ and $45° < \theta < 55°$, respectively. The vertical thin error bars and shaded thick error bars represent the statistical errors and quadratic sum of statistical and systematic errors, respectively.

5 Discussion

5.1 Summary of the results

We compared the lateral distribution of the signal size obtained on muon-enriched condition ($30^\circ < \theta < 45^\circ$, $150^\circ < |\phi| < 180^\circ$, 2000 m $< R <$ 4000 m and muon purity $\simeq 60 - 70\%$) between the experimental data and the MC for proton with QGSJET II-03 model. The ratio of the signal size of the data to that of the MC is, typically, 1.72 ± 0.10(stat.)± 0.40(syst.) at 1910 m $< R <$ 2160 m and 3.14 ± 0.36(stat.)± 0.72(syst.) at 2760 m $< R <$ 3120 m. The average signal size is found to decrease slower in the data than in the MC when R is larger, namely larger discrepancy at larger R. The significance of the discrepancy varied within 1.6 - 2.7σ at 2000 m $< R <$ 4000 m including statistical and systematic errors, depending on R. The lateral distributions for different hadronic models (QGSJET II-04, Epos 1.99 and Sibyll 2.1) also show the discrepancy of the signal size and lateral distribution shape. The signal size of the MC for iron was closer to that of the data than the MC for proton, but the data is larger than the MC for iron with $> 1\sigma$ significance in $R >$ 3000 m. Comparison of the signal size between the data and the MC on different (θ, ϕ) conditions is performed, which means the comparison on different muon purity conditions. Larger discrepancy between the data and the MC is found at larger muon purity condition. This result indicates the discrepancy is partially due to muon excess in the data.

Let us comment on hadronic interaction of UHECR. The result shows the lateral distribution of the experimental data is broader than that of the MC. It is possible that the air showers develop faster in the data than the MC, which is caused by the larger hadron interaction cross-section, lower pion energy distribution at the generation or larger multiplicity in the data than the MC [91]. If the air shower develops faster, the lateral distribution on the ground becomes broader. It also causes larger attenuation of electromagnetic (EM) components in the air, resulting in larger ratio of muons to EM particles in number on the ground. $X^{\mu}_{\rm max}$ analysis reported by the Pierre Auger Observatory [42, 43] also suggests air showers develop faster in the data than the MC.

However, the above idea cannot explain all features of the results. Muons and EM components on the ground originate from $\pi^{\pm}$ and π^0 generated in the atmosphere, respectively. The pions are related to each other. If lateral distribution of muons of the data is broader than the MC, $\pi^{\pm}$ development is expected to be faster, and π^0 should has same feature as $\pi^{\pm}$. Thus lateral distribution of EM components of the data should be broader than MC. But the lateral distributions on muon-less (EM-enriched) (θ, ϕ)

condition match between the data and the MC, for example, on condition $\theta < 30°, |\phi| < 30°$ (muon purity: $\sim 30\%$) as shown in the top panels in figure 4.18.

5.2 Comparison with results of Auger experiment

Pierre Auger Observatory reported that the observed number of muons for 10^{19} eV primary cosmic rays was 30% - 80% higher than the MC prediction value assuming the primary composition inferred from $X_{\max}$ measurement [11]. In the analysis, hybrid events for $\theta > 60°$ are selected and the signal size is converted to the number of muons by using MC study [48]. Assuming the MC using QGSJET II-03 model for proton, the average ratio of observed number of muons to MC prediction value is $1.841 \pm 0.029(\text{stat.}) \pm 0.324(\text{syst.})$. This means the significance of the discrepancy is 2.6 σ, which is a similar level of results of this work.

The Auger experiment also reported the number of particles for $10^{18.8} - 10^{19.2}$ eV primaries shows the discrepancy between a measured and simulated signal size at $R = 1000$ m [87]. In the analysis, hybrid events for $\theta < 60°$ are selected and compared with simulated ones which have the similar longitudinal development. They analyzed muon and EM contributions to the signal and concluded that the ground signal from hadronic component of the shower, which consists of most of muons, was 1.33 ± 0.16 and 1.61 ± 0.21 times higher than the MC prediction using EPOS-LHC and QGSJET II-04 models, respectively, including statistical and systematic errors. They showed larger discrepancy between the data and the MC at larger θ, which corresponds to larger muon purity. This is the feature same as this work.

The quantitative comparison between the results of this work with Auger results is difficult because the data selection and the analysis condition is different. We separate SDs in ϕ and R, but Auger analysis uses all the signals in events. Also, the Auger analysis does not use 0 signal size detectors. In addition, the energy thresholds of the TA SD and the Auger SD are ~ 10 MeV and ~ 240 MeV, respectively. That suggests the air shower particles observed by the detector have different property between the two detectors.

To compare the results, further studies are necessary. The most simple method of the comparison is to make the analysis with the Auger data by the method of this work. The second method is to establish the dethinning method on $\theta > 60°$ condition and make the analysis with the TA SD on the condition. That requires tuning of the dethinning parameters for the TA SD and confirm its reliability. On $\theta > 60°$ condition, the TA SD signal is expected to be dominated by the muon component, in the same way as the Auger SD. The third method is to analyze the TA SD data with the Auger analysis method on $\theta < 60°$ condition. This method requires studying air shower MC to divide the air shower components more precisely, using the parent particle information of the particles on the ground [87, 52]. Also, in the method hybrid events are used, so it should be confirmed that the statistics of the TA hybrid events are enough for the analysis.

5.3 Suggestion for energy scale discrepancy between SD and FD

The difference of the energy scale between the TA SD and the TA FD is an unsolved issue in the UHECR observation. From the results of the present work, it is indicated that part of the difference is due to the muon excess. The detail is explained below.

In the SD spectrum analysis [12], the primary energy is determined by $S800$ and zenith angle using the conversion table made by TA SD MC. Here $S800$ is the signal size (units in VEM/m^2) at 800 m from the shower axis calculated by the lateral distribution fitting function. Then the energy is rescaled by -27% so that it becomes consistent with the energy measured by the FD. This means the energy scale discrepancy corresponds to $S800$ difference between the data and the MC. Figure 5.1 shows $S800$ distributions of data (FD scale), MC (MC scale) and MC (FD scale). In the figure, the area of the histograms of the MC are normalized to that of the data. Here the energy is calculated as described above in FD scale, and the rescaling by -27% lacks in MC scale. On the ordinary SD analysis condition ($E > 10^{18.0}$ eV, $\theta < 45^\circ$), the $S800$ distribution of the data well matches that of the MC (FD scale). On the muon analysis condition ($10^{18.8}$ eV $< E < 10^{19.2}$ eV, $30^\circ < \theta < 45^\circ$), the average $S800$ value of the data still matches that of the MC (FD scale) and is $1.252^{+0.009}_{-0.008}$ times larger than the MC (MC scale). Here the error is the statistical error. The average $S800$ value of the MC (FD scale) is $1.218^{+0.003}_{-0.003}$ times larger than that of the MC (MC scale). The comparison of data (FD scale) with MC (MC scale) corresponds to that of the number of particles between data and MC in a fixed energy. The difference between MC (MC scale) and MC (FD scale) corresponds to 27% energy scale difference.

In this study, the data is compared with the MC in each (θ, ϕ, R) condition. Figure 5.2 shows the lateral distributions of signal size of data (FD scale), MC (MC scale) and MC (FD scale) for $\theta < 45^\circ$ and their ratios. The data is $\sim 1.24 \pm 0.01$ times larger than MC (MC scale), which nearly corresponds to 27% energy scale difference. Figure 5.3 shows the same as figure 5.2 but for muon-enriched condition ($10^{18.8}$ eV $< E < 10^{19.2}$ eV, $30^\circ < \theta < 45^\circ$, $150^\circ < \phi < 180^\circ$). The data is ~ 1.83 times larger than MC (MC scale) at $R \simeq 2000$ m, and the ratio of them is larger at larger lateral distance, as shown in chapter 4. The ratio of MC (FD scale) to MC (MC scale) is ~ 1.26 at $R \simeq 2000$ m, which corresponds to 27% energy scale difference, and the ratio is smaller than the difference between data and MC (MC scale). The similar feature occurs at $R > 1000$ m.

Although the contribution of muons to the difference in the signal size at $R = 800$ m is unclear, $\sim 20\%$ of the SD signal at $R = 800$ m is expected to come from air shower muons. Hence it is indicated that the energy scale difference is partially due to muon excess.

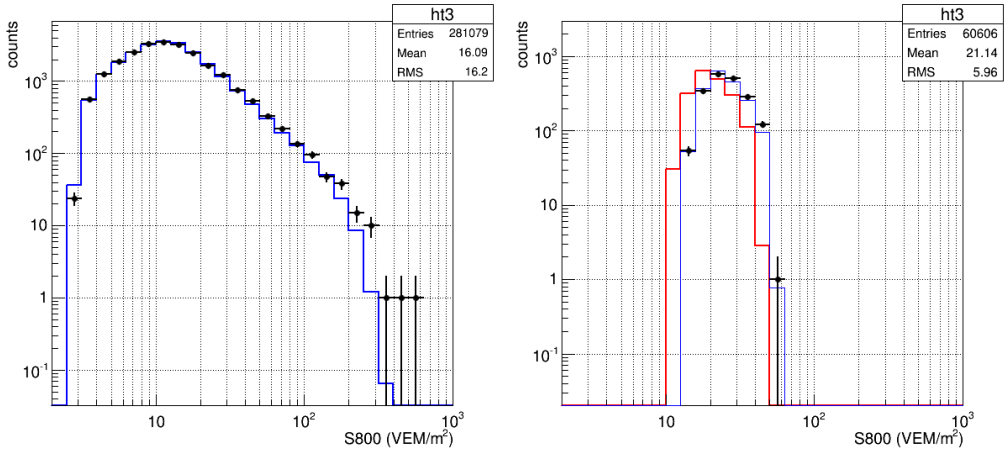

Figure 5.1: S800 distribution. The black, red and blue represent data, MC (MC scale) and MC (FD scale), respectively. (left) Distributions for all the events which passed quality cut ($E > 10^{18.0}$ eV, $\theta < 45°$). MC (MC scale) is not shown because the energy threshold of the cut is determined in FD energy scale. (right) Distributions for muon analysis condition ($10^{18.8}$ eV $< E < 10^{19.2}$ eV, $30° < \theta < 45°$).

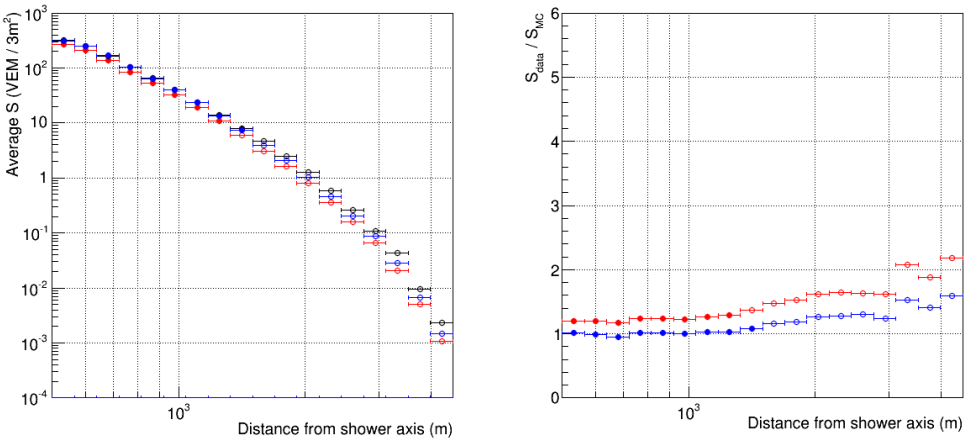

Figure 5.2: Lateral distributions of average integrated FADC values for all the events which passed quality cut ($E > 10^{18.0}$ eV, $\theta < 45°$). The color shows data (black), MC (MC scale) (red) and MC (FD scale) (blue). The filled circle is the plot with statistical error, while the open circle is the plot where the statistical error cannot be calculated, as explained in chapter 4.

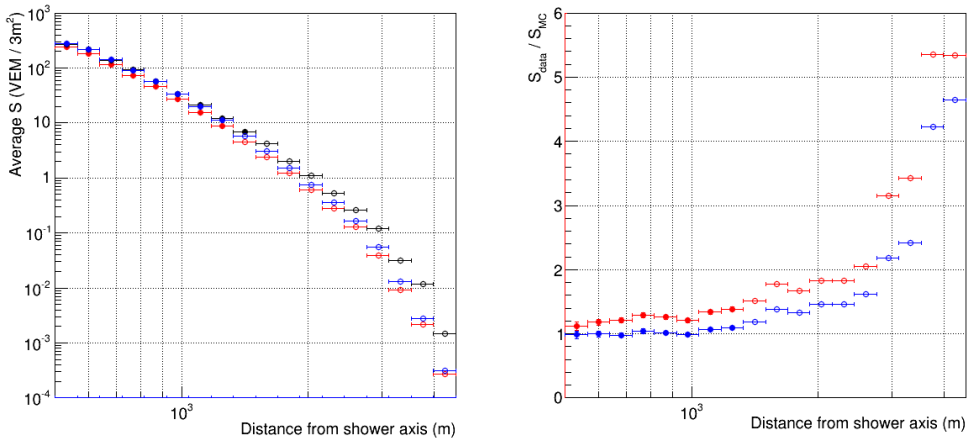

Figure 5.3: Same as figure 5.2, but for muon-enriched condition ($10^{18.8}$ eV $< E < 10^{19.2}$ eV, $30° < \theta < 45°$, $150° < \phi < 180°$).

5.4 Future prospects

The discrepancy between the data and the MC in muon counting can be further studied by compared with the Auger analyses, as described in section 5.2. The present analysis can be extended to higher energy range, $E > 10^{19.2}$ eV. That reveals the energy dependence of the discrepancy to high energy range. This analysis should be also extended to latest hadronic models, EPOS-LHC and Sibyll 2.3, to test the models.

The TA Low-energy Extention (TALE) experiment is ongoing [92]. It will measure cosmic ray spectrum and $X_{\rm max}$ around 10^{16} eV - 10^{17} eV and research the transition from galactic to extragalactic cosmic rays. The present analysis can be extended to the TALE experiment. That may reveal the starting value of the energy where the muon excess occurs. Since TALE will use TA type SD and FD to the north of the TA site, the systematic uncertainty between the TA and TALE experiments should be understood.

The TAx4 experiment aims the observation of the UHECR around 10^{20} eV. It will be performed by the extension of the TA type SD and FD around the current TA site. Therefore the present analysis can be extended to the experiment. Although the statistics is smaller than the current analysis due to the lower flux at around 10^{20} eV, it is challenging.

The TA muon detector project is proceeding at the TA CLF, located in the central position at the TA site [93, 94]. The purpose of the project is to measure air shower particles with different energy threshold detectors and obtain the information about the difference in the number of particles between the data and the MC in each threshold energy. That enables us to understand the hadron interaction of the UHECR and the energy scale discrepancy between TA SD and TA FD, which is described in section 5.3. This project will produce more detail information about the discrepancy of the number of particles of the data with that of the MC studied in the present work.

Figure 5.4: The detectors deployed at the TA CLF.

There are three types of detectors at the TA CLF; concrete shield detector, lead burger detector and Auger SD as shown in figure 5.4. Air showers are reconstructed by the surrounding TA SD array and the detectors in the CLF observe the number of muons in each shower separately. The concrete shield detector consists of eight TA SD scintillator boxes with a 1.2 m thickness concrete shield above the boxes. The detector has a surface area of 24 m^2 as a whole and its energy threshold is 600 MeV. The almost all of the number of air shower particles counted by the detector is that from muon component. The electronics are the same as TA SD, which has a 50 MHz sampling rate. Part of the segments (3 m^2) are continuing data acquisition from 2015.

The lead burger detector consists of the TA SD with a 25 mm lead plate between the upper and lower scintillator layers. Most of muons from air showers can penetrate all layers of the detector and record signals in the upper and lower layers, while most of electrons are absorbed in the lead plate. Gamma rays from air showers produce electrons by pair production in the lead plate, leaving signals in the lower layer. Thus the detector can separate air shower particle types. The detector 3 m^2 area is segmented into 0.75 m^2 each to increase muon counting accuracy. The estimated accuracy of counting the number of muons is about 20% at $R \geq 1200$ m [93]. The coincident air shower events with surrounding TA SD has been obtained by the observation with one segment operation.

The Auger SD is a water Cherenkov tank which is 1.5 m tall and has a footprint of 10 m^2. It is filled to a depth of about 1.2 m with about 10 MΩ-cm resistivity water. The Cherenkov light from air shower particles is diffusively reflected inside the water volume and viewed by the PMTs through optical windows. The thickness of the water works as an absorber and reduces the EM signals from air showers. The detector threshold is about 240 MeV. There are muon counting methods established by the Auger experiment [11], [87] and the method for the Auger SD at the TA CLF is under construction.

There is another purpose to set Auger SD at the TA CLF. There are differences between the results of the TA and that of the Auger, e.g. the energy at which the flux suppression occurs, the interpretation of that suppression and the composition of the UHECR primaries at the highest energies, as explained in section 1.4. The TA SD

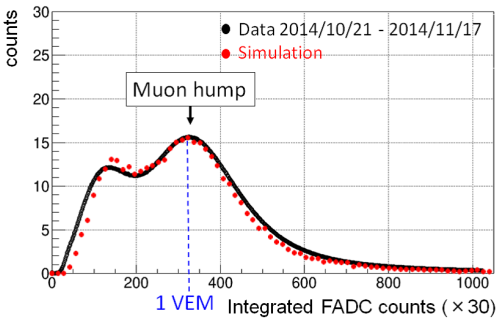

Figure 5.5: The 1 VEM histogram from the calibration data and the MC simulation [94]. The simulation is from a CORSIKA air shower simulation in which the QGSJET Ⅱ-04 hadronic interaction model and the Geant4 detector simulation are used. The peak position of the histogram for the simulation is adjusted to fit the experimental data.

detects mainly EM components that is the major part of air showers, while Auger SD detects EM and muon components as described above. Such detector difference may contribute to the results as systematic uncertainty. The systematic uncertainty can be understood by comparing the detector response to the same air showers between the Auger SD at the TA CLF and the surrounding TA SDs. We deployed one Auger SD in Oct. 2014 and it acquired the data by the local trigger. For the about 1.5 month observation, the histogram of integrated FADC values for 1 VEM calibration signal was obtained, and reproduced by the Geant4 detector simulation as shown in figure 5.5 [94]. The coincidence events between the Auger SD and the surrounding TA SDs were obtained, as shown in figure 5.6 [94]. The another Auger SD was deployed in June 2015 and the system that the two detectors receive the TA SD trigger information from the TA central trigger system was established in Aug. 2016. The current plan is to set several Auger SDs inside the TA site and have the Auger SD micro-array trigger independently to compare the trigger efficiency and energy estimators (S800 for the TA SD and S1000 for the Auger SD) with the TA SD array.

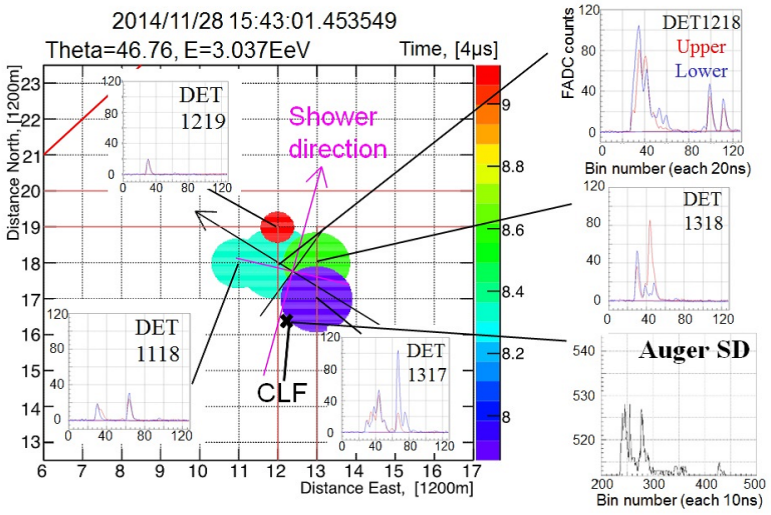

Figure 5.6: The event display of a sample coincident event [94]. The circle centers correspond to the TA SD positions. The circle areas are proportional to the logarithm of the TA SD station pulse heights. The circle colors represents the TA SD detection times from the detection time of the first triggered detector within the same $\pm$ 32 μs. The magenta arrow shows the shower axis projected onto the ground and the black x mark is the position of the Auger North SD at the CLF. The red line of the TA SD waveform is the upper layer signal, while the blue line shows the lower layer signal.

6 Conclusion

We studied muons from UHECR air showers with the TA SD to test hadronic interaction models of the air shower MC. The muon excess is reported from Pierre Auger Observatory with water Cherenkov detectors sensitive to muons [11, 87], and we did independent analysis from the report using the lateral distribution of air shower particles with plastic scintillation detectors on the ground. While almost the TA SD signals are composed of EM components, we established the method to study muons using (θ, ϕ, R) conditions, where θ is zenith angle of the shower event, ϕ is the SD azimuth angle relative to the shower axis projected onto the ground and R is the distance from shower axis to the SD.

The lateral distribution of the signal size, which is the energy deposit of air shower signals in the SD, was measured in the energy range $10^{18.8}$ eV $< E < 10^{19.2}$ eV. The air showers and the detector response were simulated in each air shower particle type, using CORSIKA air shower simulation with the dethinning method and Geant4 detector simulation. We divided the air shower events and the SDs using θ, ϕ and R conditions to search for muon-enriched analysis condition. If taking larger $\theta, |\phi|$, or R values, the atmospheric thickness between SDs and particle generation points on the shower axis increases, then the muon purity in the signal of SDs is expected to be relatively high. It was found that the muon purity was 60 - 70% on condition $30^\circ < \theta < 45^\circ, 150^\circ < |\phi| < 180^\circ$, 2000 m $< R <$ 4000 m using hadronic interaction model QGSJET II-03 for proton, although the purity was $\sim 20\%$ on the ordinary SD analysis condition.

The signal size observed on the above condition was compared with the MC prediction value for proton using QGSJET II-03 model. The typical ratio of the signal size of the experimental data to that of the MC was $1.72 \pm 0.10(\text{stat.}) \pm 0.40(\text{syst.})$ at 1910 m $< R <$ 2160 m and $3.14 \pm 0.36(\text{stat.}) \pm 0.72(\text{syst.})$ at 2760 m $< R <$ 3120 m. The average signal size is found to decrease slower in the data than in the MC when R is larger, namely larger discrepancy at larger R. The significance of the discrepancy varied within 1.6 - 2.7σ at 2000 m $< R <$ 4000 m including statistical and systematic errors, depending on R. The lateral distributions for different hadronic models (QGSJET II-04, Epos 1.99 and Sibyll 2.1) also showed the discrepancy in the signal size and the lateral distribution shape. The signal size of the MC for iron was closer to that of the data than the MC for proton, but the data is larger than the MC for iron with the significance greater than 1σ in $R >$ 3000 m. Comparison of the signal size between the data and the MC on different (θ, ϕ) conditions showed the property of larger discrepancy at larger muon purity condition. This result indicates that the MC does not reproduce the data on the

analysis (θ, ϕ, R) condition described above and the discrepancy is partially due to the muon excess in the data.

The feature that the signal size of the data is larger than that of the MC obtained in this work was qualitatively consistent with the muon excess detected in researches of Pierre Auger Observatory. In addition to the Auger analysis, where the R dependence of muons is not studied, we confirmed the lateral distribution of the MC does not reproduce the data on the analysis (θ, ϕ, R) condition with the significance described above. This result provides the information to improve reliability of the air shower MC and obtain a realistic air shower model.

Appendix I
The acceleration mechanism of high energy particle

In this section, the acceleration mechanism of high energy particles, called Fermi acceleration, and their maximum energy is explained [96].

The Fermi mechanism was first proposed in 1949 as an acceleration means by which particles colliding with clouds in the interstellar medium could be accelerated [10]. This theory naturally explains that the cosmic ray energy spectrum forms a power-law.

Let us assume charged particles are reflected from magnetic mirrors associated with irregularities in the galactic magnetic field. The mirrors move randomly with typical velocities V. Consider the collision between the particle and the mirror takes place such that the angle between the initial direction of the particle and the normal to the mirror surface is θ, as shown in figure 6.1. The mirror is taken to be infinitely massive so the velocity is unchanged in the collision. The energy of the particle in the cloud moving frame is

$$E' = \gamma_V(E + Vp\cos\theta), \quad \text{where} \quad \gamma_V = \left(1 - \frac{V^2}{c^2}\right)^{-1/2} \tag{6.1}$$

Here cloud moving frame is noted by $'$. E is the particle energy, p is the particle momentum and c is the speed of the light. The x component of the momentum is

$$p'_x = p'\cos\theta' = \gamma_V\left(p\cos\theta + \frac{VE}{c^2}\right) \tag{6.2}$$

In the collision, E' is conserved and the momentum in the x direction p'_x is reversed. Therefore, transforming back to the observer' s frame,

$$E'' = \gamma_V(E' + Vp'_{\mathrm{x}}) \tag{6.3}$$

Substituting (6.1) and (6.2) into (6.3) and using the relation $p_x/E = v\cos\theta/c^2$, where v is the speed of the particle, then

$$E'' = \gamma_V^2 E\left[1 + \frac{2Vv\cos\theta}{c^2} + \left(\frac{V^2}{c}\right)\right] \tag{6.4}$$

Expanding to second order in V/c, the change of the particle energy is

$$\Delta E \equiv E'' - E = E\left[\frac{2Vv\cos\theta}{c^2} + 2\left(\frac{V^2}{c}\right)\right] \tag{6.5}$$

Averaging over the random distribution angles θ, the rate of a head-on collision (left panel of figure 6.1) is larger than a following collision (right panel of figure 6.1), then

$$\left\langle\frac{\Delta E}{E}\right\rangle = \frac{8}{3}\left(\frac{V}{c}\right)^2 \tag{6.6}$$

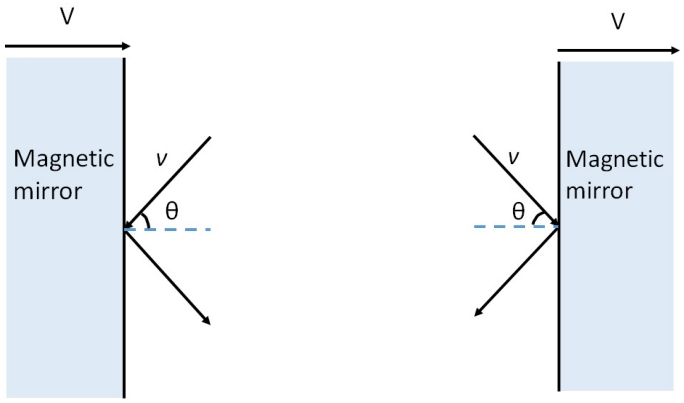

Figure 6.1: Schematics of charged particles reflecting from magnetic mirrors associated with irregularities in the galactic magnetic field. (left) Forward collision. (right) Backward collision.

This illustrates the same average fractional increase in the energy of the particle per collision. The average increase in energy is second-order in V/c, so this mechanism is called second-order Fermi acceleration.

If the mean free path between clouds is L, the time between collisions is $L/(c\cos\Phi)$ where Φ is the pitch angle of the particle with respect to the magnetic field direction. Averaging over Φ, the time between collisions becomes $2L/c$. Therefore the rate of energy increase is

$$\frac{\mathrm{d}E}{\mathrm{d}t} = \frac{4}{3}\left(\frac{V^2}{cL}\right)E = \alpha E \tag{6.7}$$

The spectrum is obtained from the diffusion-loss equation,

$$\frac{\mathrm{d}N}{\mathrm{d}t} = D\nabla^2 N + \frac{\partial}{\partial E}[b(E)N(E)] - \frac{N}{\tau_{\mathrm{esc}}} + Q(E) \tag{6.8}$$

Where D is diffusion coefficient, $b(E) = -\frac{\mathrm{d}E}{\mathrm{d}t}$ is the energy loss term, $Q(E)$ is the source term. If we assume steady state condition, $dN/dt = 0$. Also if we assume the absence of diffusion and there are no sources, $D = 0$ and $Q(E) = 0$. The energy loss term $b(E) \equiv -dE/dt = -\alpha E$. Therefore (6.8) becomes

$$-\frac{d}{dE}[\alpha E N(E)] - \frac{N}{\tau_{\mathrm{esc}}} = 0 \tag{6.9}$$

Rearranging the equation,

$$\frac{dN(E)}{dE} = -\left(1 + \frac{1}{\alpha\tau_{\mathrm{esc}}}\right)\frac{N(E)}{E} \tag{6.10}$$

and

$$N(E) = \text{constant} \times E^{-x} \tag{6.11}$$

Where $x = 1 + (\alpha\tau_{\mathrm{esc}})^{-1}$. This function forms power-law spectrum.

Second-order Fermi acceleration has a problem that the spectral index x cannot be determined. The acceleration mechanism is improved in 1970s , which is associated with particle acceleration in strong shock waves. It is often referred to as "diffusive shock acceleration". We will follow one of the approach [95].

The model involves a strong shock propagating through a diffuse medium, for example, the shock waves which propagate through the interstellar medium ahead of the supersonic shells of supernova remnants. High energy particles are assumed to be present both in front of and behind the shock front. A shock wave at a supersonic velocity $U \gg c_s$, where c_s is the sound speed in the ambient medium. Transforming into the frame of reference in which the shock front is at rest, the upstream gas flows into the shock front at velocity $v_1 = U$ and leaves the shock with a downstream velocity v_2. Here the notations 1 and 2 represent upstream and downstream. The mass is conserved through the shock front and so

$$\rho_1 v_1 = \rho_1 U = \rho_2 v_2 \tag{6.12}$$

In the case of a strong shock, $\rho_2/\rho_1 = (\gamma+1)/(\gamma-1)$ where γ is the ratio of specific heat capacity of the gas. Taking a monatomic or fully ionized gas, $\gamma = 5/3$ and $\rho_2/\rho_1 = 4$ then $v_2 = (1/4)v_1$. Let us consider high energy particles ahead of the shock. In the frame of reference in which the upstream gas is at rest, the particle distribution is isotropic by scattering in the upstream region, while the gas flows to the shock front at a velocity of $(3/4)U$ in the downstream region. When a particle in the upstream region crosses the shock front, it encounter head-on collision as described in second-order Fermi acceleration. Then the energy becomes

$$E' = \gamma_V (E + p_x V) \tag{6.13}$$

where $V = (3/4)U$. The shock is assumed to be non-relativistic, $V \ll c, \gamma = 1$. Then the particle obtain

$$\Delta E = pV \cos\theta \tag{6.14}$$

Averaging over injection angle,

$$\left\langle \frac{\Delta E}{E} \right\rangle = \frac{V}{c} \int_0^{\pi/2} 2\cos^2\theta \sin\theta \mathrm{d}\theta = \frac{2}{3}\frac{V}{c} \tag{6.15}$$

When the particle recross the shock front, the opposite same occurs. Considering the reference frame in which the downstream gas is at rest, the particle distribution is isotropic by scattering in the downstream region, while the gas flows to the shock front at a velocity of $(3/4)U$ in the upstream region. Then the particle obtains fractional increase in energy $(2/3)U$. Therefore, in making one round trip across the shock and back again, the average fractional energy increase is

$$\left\langle \frac{\Delta E}{E} \right\rangle = \frac{4}{3}\frac{V}{c} \tag{6.16}$$

Now we define the constants β and P; $\beta = E/E_0$ is the energy gain after one collision and P is the probability that the particle remains within the accelerating region after one collision. Here

$$\beta = \frac{E}{E_0} = 1 + \frac{4V}{3c} \tag{6.17}$$

in one round trip. Thus, $P = 1 - (U/c)$.

After k collisions, there are $N = n_0 P_k$ particles with energies $E = E_0 \beta_k$. Eliminating k between them,

$$\frac{\ln(N/N_0)}{\ln(E/E_0)} = \frac{\ln P}{\ln \beta} \tag{6.18}$$

Hence

$$\frac{N}{N_0} = \left(\frac{E}{E_0}\right)^{\ln P/\ln \beta} \tag{6.19}$$

This value of N is $N(\geq E)$ since this is the number which reachs energy E and some fraction of them continue to be accelerated to higher energies. Therefore

$$N(E)\mathrm{d}E = \text{constant} \times E^{-1+(\ln P/\ln \beta)}\mathrm{d}E \tag{6.20}$$

From above sentences,

$$\ln P = \ln\left(1 - \frac{U}{c}\right) = -\frac{U}{c} \tag{6.21}$$

$$\ln \beta = \ln\left(1 + \frac{4V}{3c}\right) = \frac{4V}{3c} = \frac{U}{c} \tag{6.22}$$

And

$$N(E)\mathrm{d}E \propto E^{-2}\mathrm{d}E \tag{6.23}$$

This mechanism can produce the spectrum index 2, so is widely used for the theory of particle acceleration at SNRs. In this theory, the fractional energy increase $\Delta E/E$ is proportional to first order of V/c, so the mechanism is referred to as "first-order Fermi acceleration".

On a particle acceleration in a magnetic field, The particle Larmor radius needs to be less than the size of the source to continue the acceleration. By magnetic field flux density B and the scale L of the acceleration region, the maximum acceleration energy $E_{\max}$ can be calculated. From Faraday' s law,

$$\nabla \times E = -\frac{\partial \mathbf{B}}{\partial t} \tag{6.24}$$

where E is the induced electric field in the region. This equation can be rewritten to order of magnitude as

$$\frac{E}{L} \sim \frac{B}{L/U}\,; \qquad E \sim BU \tag{6.25}$$

where U is the speed of the shock. Then the energy of a particle of charge ze accelerated by the electric field is

$$E_{\max} \int zeE\,\mathrm{d}x = zeBUL \tag{6.26}$$

Appendix II
Lateral distribution of muons from UHECR air showers

The AGASA group reported the lateral distribution of muons (LDM) in the energy range $10^{17.5}$ eV - $10^{19.5}$ eV observed with the 1 km^2, 20 km^2 and 100 km^2 muon detector array [97]. The absorber of the electromagnetic component is set over the detectors which is either concrete or the combination of iron and lead. The threshold muon energy of the detectors is about 0.5 GeV - 1 GeV. Figure 6.2 shows the lateral distributions of the average number density of muons by the AGASA group. The formula of LDM given by Greisen [23] is

$$\rho_\mu(R) = N_\mu(C_\mu/{R_0}^2)r^{-\alpha}(1+r)^{-\beta} \tag{6.27}$$

where N_μ is the total number of muons, $r = R/R_0$ and R_0 is a characteristic distance. C_μ is a normalization factor, given by $\Gamma(\beta)/(2\pi\Gamma(2-\alpha)\Gamma(\alpha+\beta-2))$ and $\alpha = 0.75$. The best fitted LDM from R = 800 m - 2000 m is obtained by modifying (6.27) and expressed as

$$\rho_\mu = N_\mu(C_\mu^{'}/R_0^2)r^{-0.75}(1+r)^{-\beta}[1+(R/800\,\mathrm{m})^3]^{-\delta} \tag{6.28}$$

where $\delta \sim 0.6$, $C_\mu^{'}$ is 0.325 and $\beta = 2.52$. R_0 is expressed by

$$\log(R_0) = (0.58 \pm 0.04)(\sec\theta - 1) + (2.39 \pm 0.05) \tag{6.29}$$

The LDM formula (6.28) obtained from AGASA muon detector data is different from that from AGASA scintillator data (1.15). Note that in TA SD analysis the AGASA formula for scintillator SD is used for lateral distribution fitting because both TA and AGASA SDs detect EM components mostly. Although there are detector differences, it is possible that the LDF shape becomes different depending on the muon purity in the signal.

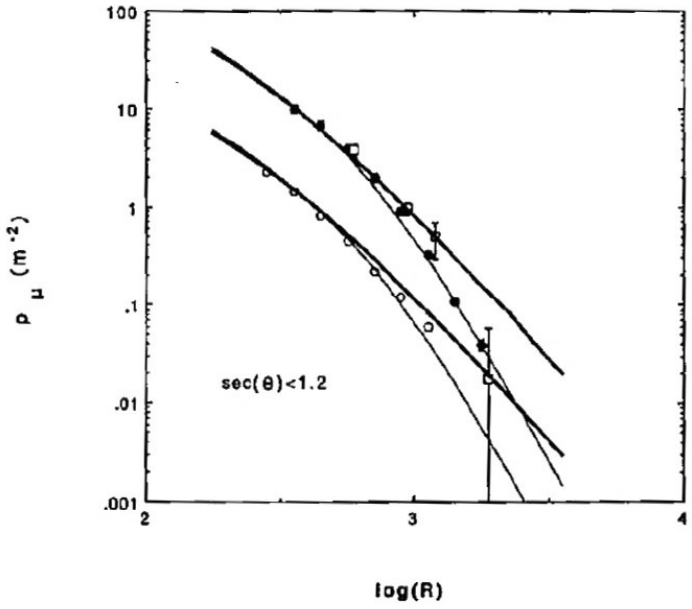

Figure 6.2: Lateral distributions of the average number density of muons above 1 GeV [97]. The open circles and full circles indicate the experimental data of air showers in $10^{17.5}$ eV $\leq E < 10^{18.0}$ eV normalized to the LDM at $10^{17.75}$ eV and in $10^{18.5}$ eV $\leq E < 10^{19.0}$ eV normalized to the LDM at $10^{18.75}$ eV, respectively obtained by AGASA 20 m^2 muon detector array. Open squares are the experimental data from 100 km^2 array, which is normalized to the LDM at $10^{18.5}$ eV $\leq E < 10^{19.0}$ eV. The thick and thin lines are fitting functions by eq.(6.27) and (6.28), respectively.

Bibliography

[1] V. F. Hess, *Über Beobachtungen der durchdringenden Strahlung bei sieben Freiballonfahrten*, *Physikalische Zeitschrift*, **13**, 1084 (1912).

[2] W. Hanlon, http://www.physics.utah.edu/ whanlon/spectrum.html, cited in 2016.

[3] Particle Data Group, *The Review of Particle Physics 29. Cosmic Rays*, http://www-pdg.lbl.gov/ (2016).

[4] P. Auger *et al.*, *Extensive Cosmic-Ray Showers*, *Rev. Mod. Phys.*, **11**, 288 (1939).

[5] K. Shinozaki and M. Teshima. *AGASA results. Nucl. Phys. Proc. Suppl.*, **136** 18-27, (2004).

[6] D. J. Bird *et al.*, *Evidence for correlated changes in the spectrum and composition of cosmic rays at extremely high-energies. Phys. Rev. Lett.*, **71**, 3401 (1993).

[7] T. Abu-Zayyad *et al.*, *First stereo results from the High Resolution Fly's Eye air fluorescence detector. Proc. 15th ICRC*, **5**, 369 (1999).

[8] J. H. Boyer *et al.*, *FADC-based DAQ for HiRes Fly's Eye*, *Nucl. Instrum. Methods. A*, **482**, 457 (2002).

[9] R. U. Abbasi *et al.*, *First Observation of the Greisen-Zatsepin-Kuzmin Suppression. Phys. Rev. Lett.*, **100**, 101101 (2008).

[10] E. Fermi, *On the origin of the cosmic radiation*, *Phys. Rev.*, **75**, 1169 (1949).

[11] A. Aab *et al.*, (The Pierre Auger Collaboration), *Muons in air showers at the Pierre Auger Observatory: Mean number in highly inclined events*, *Phys. Rev. D.*, **91**, 032003 (2015).

[12] T. Abu-Zayyad *et al.*, *The Cosmic Ray Energy Spectrum Observed with the Surface Detector of the Telescope Array Experiment*, *ApJ*, **768**, L1 (2013).

[13] T. C. Weekes *et al.*, *Observation of TeV gamma rays from the crab nebula using the atmospheric Cerenkov imaging technique*, *ApJ*, **342**, 379 (1989).

[14] A. Hillas, *The Origin of Ultra-High-Energy Cosmic Rays*, *ARA & A.*, **22**, 425H, (1984).

[15] K. Kotera and A. Olinto, *The astrophysics of ultrahigh energy cosmic rays*, arXiv:1101.4256 (2011)

[16] K. Murase *et al.*, *Blazars as ultra-high-energy cosmic-ray sources: implications for TeV gamma-ray observations*, *Astrophys.J.*, **749**, 63 (2012).

[17] E. Waxman, *Cosmological Gamma-Ray Bursts and the Highest Energy Cosmic Rays*, *Phys. Rev. Lett.*, **75**, 386 (1995).

[18] K. Greisen, *End of the cosmic-ray spectrum?*, *Phys. Rev. Lett.*, **16**, 748 (1966).

[19] G. T. Zatsepin and V. A. Kuzmin. *Upper limit of the spectrum of cosmic rays*, *JETP Lett.*, **4**, 78 (1966).

[20] P. G. Tinyakov and I. I. Tkachev, *Deflections of cosmic rays in a random component of the galactic magnetic field*, *Astroparticle Physics*, **24**, 32 (2005).

[21] T. Abu-Zayyad *et al.*, *Search for anisotropy of ultrahigh energy cosmic rays with the Telescope Array experiment*, *ApJ*, **757**, 26 (2012).

[22] Pierre Auger Observatory, https://www.auger.org/, cited in 2016.

[23] K. Greisen, *Cosmic ray air showers*, *Annu. Rev. Nucl. Sci.*, **10**, 63 (1960).

[24] J. Linsley *et al.*, *Energy Spectrum and Structure of Large Air Showers*, *J. Phys. Soc. Japan*, **17**, suppl A-Ⅲ, 91 (1962).

[25] M. Teshima *et al.*, *Properties of* $10^9 - 10^{10}$ *GeV extensive air showers at core distances between 100 and 3000 m*, **12**, 1097 (1986).

[26] *et al.*, *Lateral distribution of charged particles in giant air showers above 1 EeV observed by AGASA*, *J. Phys. G: Nucl. Part. Phys.*, **20**, 651 (1994).

[27] T. Gaisser, A. Hillas, *Reliability of the method of constant intensity cuts for reconstructing the average development of vertical showers*, *Proc. 15th ICRC*, 8, 353, (1977).

[28] Telescope Array, http://www.telescopearray.org/, cited in 2016.

[29] I. Valiño *et al.*, *The flux of ultra-high energy cosmic rays after ten years of operation of the Pierre Auger Observatory*, *Proc. 34th ICRC*, 271 (2015).

[30] M. Unger *et al.*, *Report of the working group on the composition of ultra-high energy cosmic rays*, *Proc. 34th ICRC*, 307 (2015).

[31] T. Stroman *et al.*, *Telescope Array measurement of UHECR composition from stereoscopic fluorescence detection*, *Proc. 34th ICRC*, 361 (2015).

[32] D. Ikeda *et al.*, *JPS meeting*, September (2016).

[33] J. P. Lundquist *et al.*, *Study of UHECR composition using telescope array's Middle Drum detector and surface array in hybrid mode*, *Proc. 34th ICRC*, 441 (2015).

[34] A. Aab *et al.*, *Depth of maximum of air-shower profiles at the Pierre Auger Observatory. I. Measurements at energies above* $10^{17.8}$ *eV*, *Phys. Rev. D.*, **90**, 122005 (2014).

[35] A. Yushkov *et al.*, *Composition at the "ankle" measured by the Pierre Auger Observatory: pure or mixed?*, *Proc. 34th ICRC*, 335 (2015).

[36] R.U. Abbasi *et al.*, *Indications of intermediate-scale anisotropy of cosmic rays with energy greater than 57 EeV in the northern sky measured with the surface detector of the Telescope Array experiment*, *ApJL*, **790**, L21 (2014).

[37] K. Kawata *et al.*, *Ultra-high-energy cosmic-ray hotspot observed with the Telescope array surface detectors*, *Proc. 34th ICRC*, 276 (2015).

[38] H. He *et al.*, *Monte Carlo Bayesian search for the plausible source of the Telescope Array hotspot*, *Phys. Rev. D.*, **93**, 043001 (2016).

[39] S. Ostapchenko, *QGSJET-II: results for extensive air showers*, *Nucl. Phys. B, Proc. Suppl.*, **151**, 147 (2006).

[40] S. Ostapchenko, *Monte Carlo treatment of hadronic interactions in enhanced Pomeron scheme: QGSJET-II model*, *Phys. Rev. D.* **83**, 014018 (2011).

[41] K. Werner, F. M. Liu, and T. Pierog, *Parton ladder splitting and the rapidity dependence of transverse momentum spectra in deuteron-gold collisions at the BNL Relativistic Heavy Ion Collider*, *Phys. Rev. C.*, **74**, 044902 (2006).

[42] A. Aab *et al.*, *Muons in air showers at the Pierre Auger Observatory: Measurement of atmospheric production depth*, *Phys. Rev. D.*, **90**, 012012 (2014)

[43] L. Collica for the Pierre Auger Collaboration, *Measurement of the muon content in air showers at the Pierre Auger Observatory*, *Proc. 34th ICRC*, 336 (2015).

[44] J. C. Arteaga-Velzquez *et al.*, *Testing hadronic interaction models with the attenuation length of muons in KASCADE-Grande*, *Proc. 34th ICRC*, 314 (2015).

[45] O. Adriani *et al.*, *Measurements of longitudinal and transverse momentum distributions for neutral pions in the forward-rapidity region with the LHCf detector*, *Phys. Rev. D*, **94**, 032007 (2016).

[46] O. Adriani *et al.*, *Measurement of very forward neutron energy spectra for 7 TeV protonproton collisions at the Large Hadron Collider*, *Phys. Lett. B*, **750**, 360 (2015).

[47] D. Veberic *et al.*, *What can we learn about hadronic interactions at the Pierre Auger Observatory?*, *UHECR2016 conference* (2016).

[48] A. Aab *et al.*, (The Pierre Auger Collaboration), *Reconstruction of inclined air showers detected with the Pierre Auger Observatory*, *JCAP*, **08**, 019 (2014).

[49] N. N. Kalmykov and S. S. Ostapchenko, *Yad. Fiz.*, **56N3**, 105 (1993) [*Phys. At. Nucl.*, **56**, 346 (1993)].

[50] P. Ghia *et al.*, *Testing the surface detector simulation for the Pierre Auger Observatory*, *Proc. 30th ICRC*, 300 (2007).

[51] V. Verzi *et al.*, *The Energy Scale of the Pierre Auger Observatory*, *Proc. 33rd ICRC*, 928 (2013).

[52] M.Ave *et al.*, *Extensive Air Shower Universality of Ground Particle Distributions*, *Proc. 32nd ICRC*, 178 (2011).

[53] A. Aab *et al.*, *Depth of maximum of air-shower profiles at the Pierre Auger Observatory. II. Composition implications*, *Phys. Rev. D.*, **90**, 122006 (2014).

[54] The Pierre Auger Collaboration, *Interpretation of the depths of maximum of extensive air showers measured by the Pierre Auger Observatory*, *JCAP*, **02**, 026 (2013).

[55] S. Andringa *et al.*, *The muonic longitudinal shower profiles at production*, *Astropart. Phys.*, **35**, 821 (2012).

[56] M. Fukushima *et al.*, *Telescope Array project for extremely high energy cosmic rays*, *Prog. Theor. Phys. Suppl.* **151**, 206 (2003).

[57] S. Udo *et al.*, *The Central Laser Facility at the Telescope Array*, *Proc. 30th ICRC*, **5**, 1021 (2007).

[58] T. Abu-zayyad *et al.*, *The surface detector array of the Telescope Array experiment*, *Nucl. Instrum. Methods. A*, **689**, 87 (2012).

[59] D. Ivanov *et al.*, *TA spectrum summary*, *UHECR2016 conference* (2016).

[60] S. Ozawa *et al.*, *Data acquisition system of surface detector array of the telescope array experiment*, *Proc. 30th ICRC*, 1109 (2007).

[61] A. Taketa *et al.*, *Measurement of the spectrum of ultra-high energy cosmic rays by the Telescope Array surface array*, *Proc. 31st ICRC*, 924 (2009).

[62] R. U. Abbasi *et al.*, *The energy spectrum of cosmic rays above* $10^{17.2}$ *eV measured by the fluorescence detectors of the Telescope Array experiment in seven years*, *Astroparticle Physics*, **80**, 131 (2016).

[63] Y. Tameda *et al.*, *Trigger electronics of the new fluorescence detectors of the telescope array experiment*, *Nucl. Instrum. Methods* **A609**, 227 (2009),

[64] R. U. Abbasi *et al.*, *The hybrid energy spectrum of Telescope Array' s Middle Drum Detector and surface array*, *Astroparticle Physics* **68**, 27 (2015).

[65] R.U. Abbasi *et al.*, *Study of Ultra-High Energy Cosmic Ray composition using Telescope Array's Middle Drum detector and surface array in hybrid mode* **64**, 49 (2015).

[66] D. Ikeda *et al.*, *Energy spectrum and mass composition of ultra-high energy cosmic rays measured by the hybrid technique in Telescope Array*, *Proc. 34th ICRC*, 362 (2015).

[67] A.Taketa *et al.*, *Data Digitization and Fluorescence Signal Recognition for Telescope Array Experiment*, *Proc. 29th ICRC*, **8**, 209 (2005).

[68] D. Ikeda *et al.*, *Energy spectrum of ultra-high energy cosmic rays observed with the Telescope Array using a hybrid technique* **61**, 93 (2015).

[69] F. Kakimoto *et al.*,*A measurement of the air fluorescence yield*, *Nucl. Instrum. Methods Phys. Res. A* **372**, 527 (1996).

[70] R.U. Abassi *et al.*, *Air fluorescence measurements in the spectral range 300420 nm using a 28.5 GeV electron beam*, *Astropart. Phys.*, **29**, 77 (2008).

[71] T. Tomida *et al.*, *The atmospheric transparency measured with a LIDAR system at the Telescope Array experiment*, *Nucl. Instrum. Methods Phys. Res. A*, **654**, 653 (2011).

[72] H. Tokuno *et al.*, *On site calibration for new fluorescence detectors of the telescope array experiment*, *Nucl. Instrum. Methods Phys. Res. A*, **601**, 364 (2009).

[73] D. Ikeda *et al.*, *Calibration of the Telescope Array experiment fluorescence detectors*, *Proc. 31st ICRC*, 858 (2009).

[74] S. Kawana *et al.*, *Calibration of photomultiplier tubes for the fluorescence detector of telescope array experiment using a Rayleigh scattered laser beam*, *Nucl. Instrum. Methods Phys. Res. A*, **681**, 68 (2012).

[75] D. Heck *et al.*, *CORSIKA: A Monte Carlo Code to Simulate Extensive Air Showers*, *Forschungszentrum Karlsruhe Report FZKA*, 6019 (1998).

[76] J. Allison *et al.*, *Geant4 developments and applications*, *IEEE Trans. Nucl. Sci.*, **53**, 270 (2006).

[77] M. Kobal *et al.*, *A thinning method using weight limitation for air-shower simulations*, *Astropart.Phys.*, **15**, 259 (2001).

[78] B. T. Stokes *et al.*, *Dethinning extensive air shower simulations*, **35**, 759 (2012).

[79] B. T. Stokes *et al.*, *A simple parallelization scheme for extensive air shower simulations*, arxiv:1103.4643 (2011).

[80] D. Ivanov, *Energy spectrum measured by the Telescope Array surface detector* (Ph. D. thesis), University of Utah (2012).

[81] A. Ferrari *et al.*, *FLUKA: a multi-particle transport code (Program version 2005)*, *Tech. Rep. 2005-010*, CERN (2005).

[82] G. Battistoni *et al.*, *The FLUKA code: description and benchmarking*, *AIP Conf. Proc.*, **896**, 31 (2007).

[83] W. R. Nerson *et al.*, *The EGS4 code system*, *Tech. Rep. 0265*, SLAC (1985)

[84] R. U. Abbasi *et al.*, *First observation of the greisen-zatsepin-kuzmin suppression*, *Phys. Rev. Lett.*, **100**, 101101 (2008)

[85] T. Nonaka *et al.*, *Performance of ta surface array*, *Proc. 31st ICRC*, 974 (2009).

[86] D. Ivanov *et al.*, *TA spectrum summary*, *Proc. 34th ICRC*, 349 (2015).

[87] A. Aab *et al.*, (The Pierre Auger Collaboration), *Testing Hadronic Interactions at Ultrahigh Energies with Air Showers Measured by the Pierre Auger Observatory*, *Phys. Rev. Lett.*, **117**, 192001 (2016).

[88] T. Pierog and K. Werner, *Muon Production in Extended Air Shower Simulations*, *Phys. Rev. Lett.*, **101**, 171101 (2008).

[89] E. J. Ahn *et al.*, *Cosmic ray interaction event generator SIBYLL 2.1*, *Phys. Rev. D*, **80**, 094003 (2009).

[90] J. Matthews, *A Heitler model of extensive air showers*, *Astropart. Phys.*, **22**, 387 (2005).

[91] S. Ostapchenko and M. Bleicher, *Constraining pion interactions at very high energies by cosmic ray data*, arXiv:1601.06567 (2016)

[92] G. B. Thomson *et al.*, *The Telescope Array Low Energy Extension (TALE)*, *Proc. 32nd ICRC*, 338 (2016).

[93] T. Nonaka *et al.*, *Performance and Observational Status of Muon Detectors in the Telescope Array Experiment*, *Proc. 34th ICRC*, 656 (2015).

[94] R. Takeishi *et al.*, *Initial results of a direct comparison between the Surface Detectors of the Pierre Auger Observatory and the Telescope Array*, *Proc. 34th ICRC*, 393 (2015).

[95] A. Bell, *The acceleration of cosmic rays in shock fronts — I*, *Mon. Not. R. astr. Soc.*, **182**, 147 (1978).

[96] M. Longair, *High Energy Astrophysics*, *Cambridge University Press* (2011).

[97] N. Hayashida *et al.*, *Muons ($\geq$ 1 GeV) in large extensive air showers of energies between $10^{16.5}$ eV and $10^{19.5}$ eV observed at Akeno*, *J. Phys. G: Nucl. Part. Phys.*, **21**, 1101 (1995).